

THE RED-SEQUENCE CLUSTER SURVEY. I. THE SURVEY AND CLUSTER CATALOGS FOR PATCHES RCS 0926+37 AND RCS 1327+29

MICHAEL D. GLADDERS¹

Carnegie Observatories, 813 Santa Barbara Street, Pasadena, CA 91101; and Department of Astronomy and Astrophysics,
 University of Toronto, 60 St. George Street, Toronto, ON, M5S 3H8, Canada

AND

H. K. C. YEE¹

Department of Astronomy and Astrophysics, University of Toronto, 60 St. George Street, Toronto, ON, M5S 3H8, Canada

Received 2004 February 26; accepted 2004 October 24

ABSTRACT

The Red-Sequence Cluster Survey (RCS) is a $\sim 100 \text{ deg}^2$, two-filter imaging survey in the R_C and z' filters, designed primarily to locate and characterize galaxy clusters to redshifts as high as $z = 1.4$. This paper provides a detailed description of the survey strategy and execution, including a thorough discussion of the photometric and astrometric calibration of the survey data. The data are shown to be calibrated to a typical photometric uncertainty of $0.03\text{--}0.05 \text{ mag}$, with total astrometric uncertainties less than $0''.25$ for most objects. We also provide a detailed discussion of the adaptation of a previously described cluster search algorithm (the cluster red-sequence method) to the vagaries of real survey data, with particular attention to techniques for accounting for subtle variations in survey depths caused by changes in seeing and sky brightness and transparency. A first catalog of RCS clusters is also presented, for the survey patches RCS 0926+37 and RCS 1327+29. These catalogs, representing about 10% of the total survey and comprising a total of 429 candidate clusters and groups, contain a total of 67 cluster candidates at a photometric redshift of $0.9 < z < 1.4$, down to the chosen significance threshold of 3.29σ .

Subject headings: galaxies: clusters: general — methods: statistical — surveys

Online material: extended figures, machine-readable tables

1. INTRODUCTION

The detection and characterization of galaxy clusters has long been a goal of observational cosmology. A large number of surveys over a broad range of wavelengths have been completed in the past 50 years (see Bahcall 1977 for a detailed description of earlier surveys), and similar searches continue to be done (e.g., Gunn et al. 1986; Gioia et al. 1990; Dalton et al. 1992; Lumsden et al. 1992; Scharf et al. 1997; Ebeling et al. 1998; Rosati et al. 1998; Vikhlinin et al. 1998; Böhringer et al. 2000; Bramel et al. 2000; Gal et al. 2000; Romer et al. 2000; Ebeling et al. 2001; Bahcall et al. 2003a; Gilbank et al. 2003; Mullis et al. 2003; Valtchanov & Pierre 2003). The goals of modern surveys for galaxy clusters are better defined than their predecessors, having moved on from the typically cartographic pursuits of the early days. To be useful in a modern context, a cluster survey must be well-defined and must present a homogeneous and well-understood catalog. These basic requirements come about because the scientific questions that will be addressed with such catalogs often require a statistical analysis of large samples (e.g., Margoniner et al. 2001; Bahcall et al. 2002a). A further criterion for modern cluster surveys is that they probe a large and distant volume, again motivated by the type of studies, such as the determination of cosmological parameters (e.g., Oukbir & Blanchard 1992; Levine et al. 2002), envisioned with these cluster catalogs.

It is these joint requirements of a clean, well-characterized sample and large volumes that led to X-rays being the preferred cluster search method in the past decade. Because the intensity

of bremsstrahlung emission is proportional to the square of the electron density, X-rays offer the advantage of selecting only the densest hot gas found in the deepest potential wells. Hence, X-ray samples of clusters tend to be relatively unaffected by projection effects (since a projection of mass along a line of sight does not emit significantly at X-ray wavelengths compared to the same mass gathered into a cluster) and so tend to produce a clean sample. Moreover, it is possible to survey large areas of sky shallowly with X-ray telescopes (e.g., the *ROSAT* all-sky survey, Voges et al. 1999) and thus X-ray samples have tended to probe larger areas (e.g., Gioia et al. 1990) than surveys at other wavelengths. However, though such surveys have produced extremely useful cluster samples, their mass sensitivity is ultimately limited by precisely the physical effect that makes them attractive. It is likely that X-ray surveys will always produce the largest samples of the most massive clusters (Ebeling et al. 2001), but unlikely that X-rays will be the most effective approach in probing extremely deeply into the cluster mass function at redshift one or higher, or in probing extremely large volumes (i.e., a good fraction of the observable universe) to high redshifts, where clusters are generally expected to be less massive, quite apart from cosmological dimming effects.

As has been suggested by numerous authors (e.g., Postman et al. 1996; Olsen et al. 1999), an alternative approach for finding distant clusters is to use deep optical imaging data. One strategy for this is demonstrated in Gladders & Yee (2000). Gladders & Yee showed that two filter imaging is sufficient to perform a clean cluster search using the cluster red sequence of early-type galaxies, even when probing deeply into the mass function. Other techniques exploiting similar optical data have also been suggested, including the matched-filter algorithm (Postman et al. 1996) and its variants (Kepner et al. 1999; Lobo et al. 2000; Kim

¹ Visiting Astronomer, Canada-France-Hawaii Telescope, which is operated by the National Research Council of Canada, le Centre Nationale de la Recherche Scientifique, and the University of Hawaii.

et al. 2002), methods relying primarily on searches for the early-type galaxy population (Ostrander et al. 1998; Goto et al. 2002), and the search for the unresolved background light of the cluster (Dalcanton 1996). Recent application of some of these methods to even the shallow imaging data of the Sloan Digital Sky Survey (SDSS) illustrates the potential power and efficiency of optical cluster surveys (Bahcall et al. 2003a, 2003b). A complementary development in the late 1990s has been the advent of panoramic mosaic cameras for 4 m class telescopes; these cameras make it feasible to image the sky area required to probe a large volume to redshifts much higher than the SDSS. These two developments, large cameras and efficient search algorithms, were the impetus for the Red-Sequence Cluster Survey (RCS).

In this paper we lay out the motivation, design, and execution of the RCS in detail. We pay particular attention to both the photometric and astrometric calibration of the RCS images and measure the uncertainties in these calibrations both by internal consistency checks and by comparison to other data. We provide a detailed discussion of the adaptation of the cluster-finding algorithm of Gladders & Yee (2000) to the complexities of RCS data, with a description of techniques for accounting for subtle variations in survey depths caused by changes in seeing and sky brightness and transparency. The paper concludes by applying this modified algorithm to the calibrated data from the first two completed RCS patches, RCS 0926+37 and RCS 1327+29, which comprise about 10% of the complete survey. The resulting cluster catalog is given in its entirety over most of the RCS redshift range ($0.2 < z < 1.4$) down to a modest significance cut and includes richness estimates for each cluster using the B_{gc} statistic (e.g., Yee & López-Cruz 1999). Catalogs of clusters for other patches will be presented in future papers, as will further catalogs for the patches presented here (less robust catalogs to smaller significance cuts and refined lower redshift catalogs using upcoming bluer imaging data).

This paper is arranged as follows. In § 2 we describe the basic goals of the RCS, and how the survey was designed to meet these goals. Section 3 lays out the RCS observational strategy. In § 4 we provide a detailed description of the data reduction pipeline. We demonstrate the final data products for two of the survey patches in § 5. In § 6 we summarize the basis of the RCS cluster-finding algorithm (Gladders & Yee 2000) and discuss a number of modifications and enhancements pertaining to the application of this algorithm to real RCS data. The cluster catalogs for two survey patches are given in § 7. We use a $\Omega_M = 0.3$, $\Omega_\Lambda = 0.7$, and $h = H_0/100 \text{ km s}^{-1} \text{ Mpc}^{-1}$ cosmology, unless otherwise noted.

2. SURVEY DESIGN

2.1. Basic Goals

Five basic goals (finding clusters in a large volume, at high redshift, and to low masses, with excellent catalog uniformity and utility) drive much of the survey design for the RCS. The need for a large volume mandates a survey area of at least tens of square degrees, and preferably larger. There are similar sized recent surveys: a notable comparison, given that it also targets clusters at $z \sim 1$, is the 48 deg² *ROSAT* Distant Cluster Survey (Rosati et al. 1998). The local abundance of rich clusters (defined here as systems corresponding to Abell Richness Class 1 or greater, or equivalently those systems with a one-dimensional velocity dispersion in excess of 750 km s⁻¹) is on order of one every $10^5\text{--}10^6 h^{-3} \text{ Mpc}^3$ (e.g., Bramel et al. 2000). Over the interval $0.5 < z < 1.0$, the total comoving volume per square degree is about $(0.5\text{--}1.0) \times 10^6 h^{-3} \text{ Mpc}^3$, depending on cosmology, and

so one expects on order of one such cluster per square degree in this redshift interval, and likely less since the cluster mass function is expected to be reduced at higher redshift. Given these issues, and considerations of feasibility given limited telescope and researcher resources, we initially chose the RCS size as 50 deg², all to be imaged using the Canada-France-Hawai'i Telescope (CFHT). With the addition of several new collaborators, we added another 50 deg² to be imaged at the Cerro-Tololo Inter-American Observatory (CTIO) 4 m telescope, bringing the total planned survey area to 100 deg².

When the RCS was initially designed, there were very few clusters known at $z > 0.7$. Most examples at that time, apart from a few very massive clusters from the EMSS (Gioia & Luppino 1994), came from the survey of Gunn et al. (1986). Hence, from the perspective of survey design, it was clearly important to attempt to find a significant cluster sample at $z > 0.7$. Moreover, the samples at $z > 1$ were extremely small—only a handful of clusters—making this redshift regime particularly significant. Most importantly, the highest redshift clusters have the most significance for determining cosmological parameters (e.g., Levine et al. 2002) and offer the best constraints for studies of the evolution of cluster galaxies. We chose redshift one as a fiducial target redshift for these reasons.

The bulk of the signal for cluster finding comes from cluster galaxies within a couple of magnitudes of M^* (Gladders & Yee 2000); at redshift one this depth can be reached efficiently using 4 m class telescopes. This depth is also needed to be sensitive to lower mass clusters at more moderate redshifts (Gladders & Yee 2000).

The high-redshift goal of the RCS also mandates using very red filters (recall that the cluster-finding algorithm of Gladders & Yee 2000 is optimal when the filters span the 4000 Å break) and we hence chose to use the R_C (centered at ~ 6500 Å) and z' (centered at ~ 9100 Å) filters. The color magnitude diagrams in Figure 1 show why this choice is important. Plotted are fiducial red sequences in AB magnitudes for clusters from $0.5 < z < 1.4$ using the V and I filter pair often utilized in optical cluster surveys (e.g., Postman et al. 1996) and using the R_C and z' filter pair adopted for the RCS. All filter curves used are for the CFH12K camera (Cuillandre et al. 2000), with normal rather than red-sensitive CCDs (see § 2.2 below). The model used is a GISSEL Bruzual & Charlot (1993) model parameterized as a 0.1 Gyr burst ending at $z = 2.5$ with a $\tau = 0.1$ Gyr exponential decline thereafter, in an $h = 0.7$ universe. The R_C and z' filter pair clearly provides much better color discrimination at high redshift, as the colors are nondegenerate all the way to $z = 1.4$, and more widely separated at $0.5 < z < 1.0$. Moreover, the z' and R_C filters suffer less drastic K -correction dimming until redshifts well above one, with typical early-type galaxies at $z = 1.4$ being 0.9 and 1.2 AB magnitudes brighter than I and V_i respectively. Even the fact that the z' filter is generally less efficient than I (owing to falling CCD response in the red and a brighter sky) is also of no import, since the limiting filter at $z > 1$ for either filter set is the bluer one.

The basic outline of the RCS is thus a 100 deg² survey in R_C and z' to a depth ~ 2 mag past M^* at redshift one. This design provides a cluster sample over a large volume, to high redshifts, and low masses. By completing the survey on only two telescopes, using a single imaging instrument at each, we also hoped to ensure uniformity in the data products. Finally, to enhance the utility of the survey, we divided the survey area into a number of individual patches, which are placed to allow maximum flexibility in observing and follow-up. In practice, we chose 10 patches for the CFHT component of the survey, and 12 patches for the CTIO component. The rest of this paper

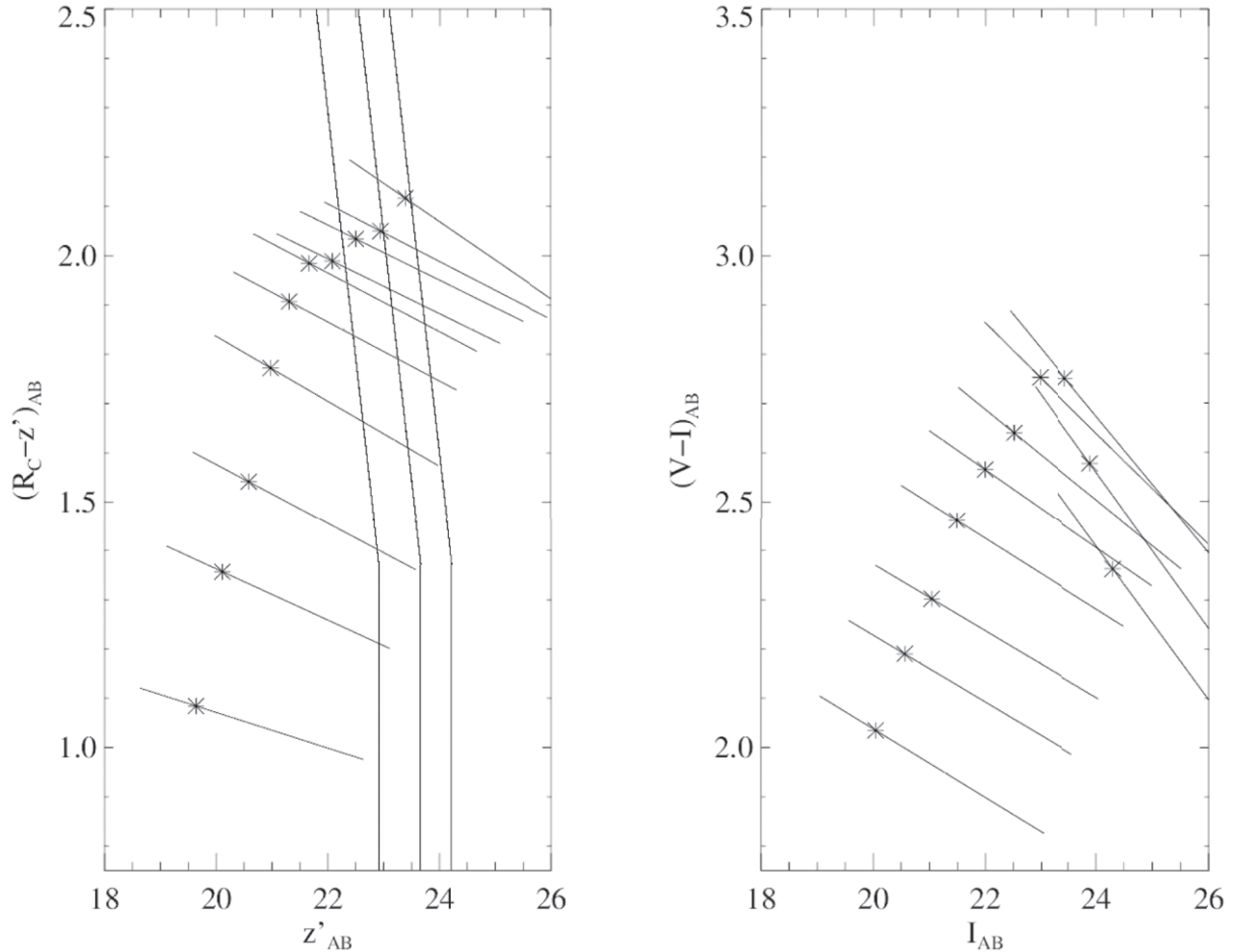


FIG. 1.—Selecting the RCS filters. Fiducial red sequences for cluster early-type galaxies at $0.5 < z < 1.4$, in steps of 0.1 in redshift, using the RCS R_C and z' filter pair (left) and the V and I filter pair often used in previous optical cluster surveys. The asterisks indicate the location of M^* at each redshift. Near vertical lines indicate the typical 10, 5, and 3 σ point-source limits for RCS data from standard chips. The 10 σ limit is conservatively the 100% completeness limit for all galaxies (regardless of profile) and the 100% completeness limit for the most relevant galaxies for cluster finding (distant early types, which are compact and nearly pointlike in typical ground-based seeing) is fainter than this.

focuses primarily on a subset of the CFHT observations—namely, the first two completed patches. The remainder of the CFHT data and the CTIO data are discussed further elsewhere (e.g., L. F. Barrientos et al. 2005, in preparation).

2.2. Patch Layout

The instrument used for the CFHT observations is the CFH12K (Cuillandre et al. 2000). This camera is a mosaic of 12 $2k \times 4k$ CCDs arranged in a 6×2 grid, with typical interchip gaps of $7''$. The camera has a plate scale of $0''.206$ per pixel, corresponding to a $42' \times 28'$ image² for the full mosaic. All chips in the CFH12K are from the MIT/Lincoln Labs CCD project. The CCDs come in two varieties: “standard” chips, and “red-sensitive” chips, which are thick, high-resistivity devices with enhanced response at wavelengths redward of ~ 7000 Å.

The patch size for the CFHT observations was chosen to provide 10 equal patches, with each consisting of 15 CFH12K pointings arranged in a slightly overlapping grid of 3×5 pointings. With a $30''$ overlap this corresponds to a patch of size $125' \times 138'$. These patches were placed according to a number of

considerations. The first was that we wished to overlap some of the patches with regions covered by other galaxy/galaxy cluster surveys. This provides added value either through comparison to cluster search results via other methods, or via complementary data. Second, we wished to avoid regions of significant interstellar dust, as the resulting extinction degrades both the depth and uniformity of the survey. We also wished to avoid bright stars, as these result in lost area, and make the data processing more difficult. These two considerations set a general constraint that all the patches be located at Galactic latitudes greater than 40° . Finally, we also avoided too high a Galactic latitude to ensure that there are enough reference stars for star-galaxy separation, astrometric corrections, and detailed point-spread function corrections for lensing analyses (e.g., Hoekstra et al. 2002).

The precise location of each patch was chosen by a careful comparison to the integrated H I map of Hartmann & Burton (1997) and the star counts from the Tycho catalog (Hoeg et al. 1997). The H I column densities were converted to an extinction estimate using the conversion from Burstein & Heiles (1978). To place a patch, three maps spanning the relevant portion of the sky were produced with a 0.1° grid spacing. The first map is an average of the estimated $E(B - V)$, convolved with a kernel the same size as a fiducial patch. The second map similarly records the integrated flux of all stars down to $R_C = 9$. The R_C magnitudes were

² Throughout this paper, when sizes of fields are described, the size in R.A. is given first, followed by the size in decl.

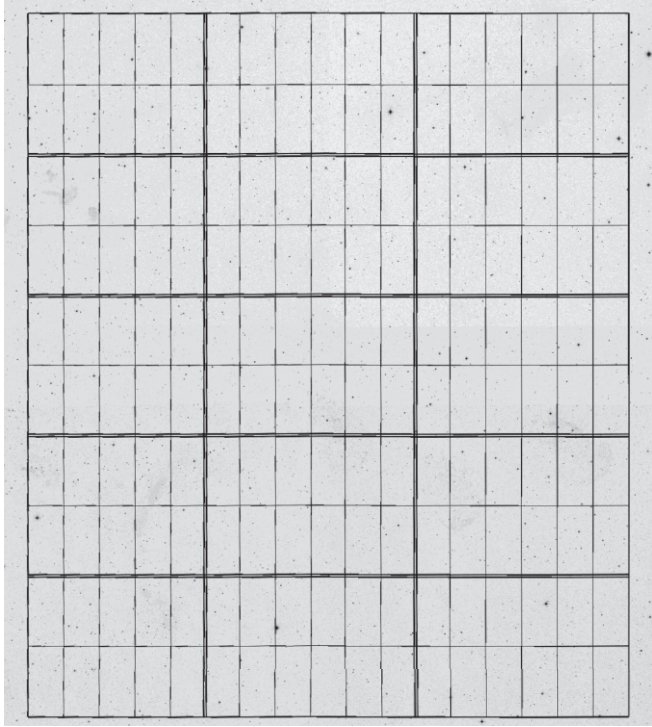


FIG. 2.—Patch RCS 1327+29. The nominal pointing placements for an example RCS patch. The background image is the digitized first-generation Palomar Optical Sky Survey, in rectangular projection with east to the right and north toward the top. The desired locations for the fifteen pointings are shown as overplotted lines. As described in the text, columns are labeled A to C, running east to west, and rows are labeled 1 to 5, running from north to south. Note that the left-hand column of pointings (C1–C5) were done in the first run and hence are 10 chips rather than 12.

estimated from the B and V magnitudes reported in the Tycho catalog. The limit of $R_C = 9$ is set both by the completeness depth of the Tycho catalog, and by the fact that the density of stars at $R_C = 9$ is high enough that the total light from fainter objects is a smooth function of Galactic latitude for the regions considered when smoothed on the patch scale. The third map simply records the brightest star in the patch area in the R_C band. Using these maps, we then searched for locations that had low average $E(B - V)$, preferably less than 0.05, no star brighter than $R_C = 6$ and with the brightest star as faint as possible, and low total light from bright stars. Typically, there were a number of candidate placements for each patch; as a final step each was examined

visually for bright galaxies (which were avoided) and then the placement that best matched the criteria outlined above was selected. For patches that were to be placed overlapping areas from preexisting surveys, we constructed similar maps over the much smaller allowed area with a finer grid and fine-tuned the patch placement to maximize the overlap while minimizing the extinction and avoiding bright stars.

Figure 2 shows an example of the patch placement, for the patch RCS 1327+29. The background image is the digitized Palomar Sky Survey image for the region, and the overplotted lines show the placement of the 15 CFHT pointings. The pointings within each patch are designated by a row and column code; the columns run from A to C, with A to the east, and the rows run from 1 to 5, with 1 to the north. This convention holds for the entire survey, with modifications in cases for extra or missing data. Note also that the 1327+29 patch was chosen to overlap a much smaller patch from the Palomar Distant Cluster Survey (Postman et al. 1996) and a patch from the older GHO survey (Gunn et al. 1986). In all cases such as this in which we overlapped areas with known surveys, we ensured that the original patch definition in the older surveys was random with respect to clusters, and we did not use the location of known clusters in the area to guide the patch placement. This ensures that the resulting patch is unbiased with respect to galaxy clusters.

The central coordinates for all 10 CFHT patches are listed in Table 1. In each case we tabulate the $100\ \mu\text{m}$ brightness estimated from *IRAS* maps, and the estimated average extinction from Schlegel et al. (1998).

Several of the observed patches deviate from the nominal plan of 15 full pointings of the CFH12K camera. Patches 0926+37, 1327+29, 1415+53, 1615+30, and 2151–06 all were observed in the first run, during which the CFH12K camera was missing two chips. Hence, these patches are missing some area. Because of scheduling requirements, we were also unable to complete two pointings in patch 1447+09 and three in 2151–06, though we did acquire three extra pointings in patch 0920+37. As a result, the entire CFHT component of the survey covers $\sim 46\ \text{deg}^2$. For each patch, the area in square degrees is indicated in Table 1.

3. OBSERVATIONAL STRATEGY

The RCS observational strategy is notably different from most ongoing surveys using mosaic cameras and hence worth describing. The most obvious difference is that the observations are not dithered: for the data from CFHT a single 15 minute R_C integration was taken at each position, as well as two 10 minute

TABLE 1
BASIC DATA FOR THE RCS CFHT PATCHES

| Patch | R.A. (J2000) | Decl. (J2000) | $100\ \mu\text{m}$ | $E(B - V)$ | Area (deg^2) | Notes |
|---------------|--------------|---------------|--------------------|------------|----------------------------|-------------|
| 0226+00 | 02 26 07.0 | +00 40 35 | 2.73 | 0.036 | 4.81 | CNOC2 Patch |
| 0351–09 | 03 51 20.7 | –09 57 41 | 2.57 | 0.043 | 4.79 | |
| 0926+37 | 09 26 09.6 | +37 10 12 | 0.39 | 0.012 | 5.59 | CNOC2 Patch |
| 1122+25 | 11 22 22.5 | +25 05 55 | N/A | 0.018 | 4.78 | |
| 1327+29 | 13 27 41.9 | +29 43 55 | –0.02 | 0.012 | 4.54 | PDCS Patch |
| 1416+53 | 14 16 35.0 | +53 02 26 | –0.20 | 0.010 | 4.53 | Groth Strip |
| 1449+09 | 14 49 26.7 | +09 00 27 | 0.89 | 0.029 | 4.17 | CNOC2 Patch |
| 1616+30 | 16 16 35.5 | +30 21 02 | 1.03 | 0.038 | 4.26 | |
| 2153–05 | 21 53 10.8 | –05 41 11 | 3.04 | 0.035 | 3.43 | CNOC2 Patch |
| 2318–00 | 23 18 10.7 | –00 04 55 | 2.96 | 0.057 | 4.84 | |

NOTE.—Units of right ascension are hours, minutes, and seconds, and units of declination are degrees, arcminutes, and arcseconds.

TABLE 2
BASIC DATA FOR THE RCS CFHT RUNS

| Run | Dates | General Comments |
|---------------|----------------|--|
| Run 1-a | 1999 May 5–6 | Photometric, excellent seeing |
| Run 1-b | 1999 Jul 7–9 | Shared, 1 night of 3, photometric |
| Run 2 | 2000 Jan 7–14 | Shared, 4 nights of 8, mostly photometric |
| Run 3 | 2000 Jul 23–26 | 1 night lost to weather, partially photometric |
| Run 4 | 2001 Jan 27–28 | Mostly photometric |

z' exposures without shifts. The 20 minutes of z' integration was split solely to keep sky levels at a reasonable value. This minimalist approach, which does not allow for the rejection of cosmetic defects or cosmic rays in the images, is driven by the need for observing efficiency and simplicity in the data processing. This latter point is of particular note and is explored further in § 4. The presence of cosmic rays and defects in the images results in a minimal loss of area, a loss that is more than compensated by the high efficiency allowed by this observing mode. Cosmic rays in particular can also affect the photometry of a small number of objects. However, the cluster-finding algorithm used on these data is insensitive to these effects.

Typically, each pointing was observed all at once, with the three integrations taken sequentially. The only exception to this is pointings imaged near twilight. Experience from the first CFHT run in 1999 May showed that z' images taken near twilight do not defringe as well as those taken in the middle of the night. Hence, on all subsequent runs, we typically observed two pointings in R_C sequentially at the beginning and the end of the night, with the corresponding z' data acquired more toward midnight. In most cases, pointing was done blindly, since slewing to a target directly and integrating without checking the pointing is the most time efficient. For pointings with split R_C and z' data we ensured that the data were taken at the same position by returning to the same telescope coordinates and guider position. This ensured a good position match in all but a few cases.

Apart from these two changes, the observing runs proceeded in a fairly standard manner. Photometric standard fields from

Landolt (1992) were observed during twilight at the beginning and end of each photometric night, and the central region of M67 was observed once per run for astrometric calibration. In cases where data were deemed nonphotometric we acquired short integrations of the same field during a photometric night to ensure a proper calibration. The basic data for each run are summarized in Table 2. The RCS runs were mostly photometric, typically with subarcsecond seeing. One complete night was lost during Run 3, and the equivalent of approximately one more night was lost during the remaining runs because of telescope problems and minor weather losses. In total, the entire imaging program required 11 clear nights.

The data discussed in the rest of this paper are from Run 1-a, on 1999 May 5–6, Run 2, on 2000 January 7–14, and Run 4, on 2001 January 27–28. A total of 33 pointings comprising two patches are considered, and the relevant data for each, including estimates of the seeing for each pointing, are given in Tables 3 and 4.

4. DATA REDUCTION

The data reduction for mosaic images is typically quite complex and fraught with a number of subtleties that can hinder those used to working on single-chip CCD data. The design of the RCS observations allows us to circumvent many of these issues, since each camera chip may be treated independently. Hence, standard single CCD methods (and programs) may be used for much of the data reduction. Note that it is never our goal to construct large scale homogeneous images from the RCS survey data, and hence photometric and astrometric calibration can be performed after the data have been extracted to catalog form. This avoids many of the complications typical of mosaic data, which often relate to how to photometrically and

TABLE 3
OBSERVATIONAL DATA FOR THE PATCH RCS 0926+37

| Pointing | Run | Seeing R_C/z' (arcsec) | Int. Time R_C/z' (s) |
|-------------|-----|-----------------------------|---------------------------|
| 0926A0..... | 4 | 1.03/1.05 | 900/1200 |
| 0926A1..... | 2 | 0.87/0.74 | 840/1200 |
| 0926A2..... | 2 | 0.81/0.99 | 900/1800 |
| 0926A3..... | 2 | 1.00/1.02 | 840/1140 |
| 0926A4..... | 2 | 0.97/1.16 | 840/1140 |
| 0926A5..... | 2 | 1.11/0.99 | 840/1140 |
| 0926B0..... | 4 | 1.09/1.05 | 900/1200 |
| 0926B1..... | 2 | 0.76/0.68 | 900/1200 |
| 0926B2..... | 2 | 0.77/0.73 | 900/1200 |
| 0926B3..... | 2 | 0.82/0.68 | 900/1200 |
| 0926B4..... | 2 | 0.65/0.66 | 900/1140 |
| 0926B5..... | 2 | 0.89/0.80 | 900/1200 |
| 0926C0..... | 4 | 1.02/0.85 | 840/1100 |
| 0926C1..... | 2 | 0.94/0.86 | 840/1200 |
| 0926C2..... | 1-a | 0.61/0.57 | 900/1200 |
| 0926C3..... | 1-a | 0.71/0.63 | 900/1200 |
| 0926C4..... | 1-a | 0.73/0.69 | 900/1200 |
| 0926C5..... | 2 | 0.97/0.89 | 840/1200 |

TABLE 4
OBSERVATIONAL DATA FOR THE PATCH RCS 1327+29

| Pointing | Run | Seeing R_C/z' (arcsec) | Int. Time R_C/z' (s) |
|-------------|-----|-----------------------------|---------------------------|
| 1327A1..... | 2 | 0.91/1.04 | 500/1400 |
| 1327A2..... | 2 | 0.72/0.88 | 900/1200 |
| 1327A3..... | 2 | 0.77/0.66 | 840/1140 |
| 1327A4..... | 2 | 0.75/0.70 | 840/1080 |
| 1327A5..... | 2 | 0.79/0.87 | 900/1200 |
| 1327B1..... | 2 | 0.78/0.69 | 900/1200 |
| 1327B2..... | 2 | 0.76/0.67 | 900/1200 |
| 1327B3..... | 2 | 0.87/0.68 | 840/1200 |
| 1327B4..... | 2 | 0.91/0.78 | 840/1140 |
| 1327B5..... | 2 | 1.18/1.10 | 500/1100 |
| 1327C1..... | 1-a | 0.62/0.55 | 840/1200 |
| 1327C2..... | 1-a | 0.57/0.59 | 900/1200 |
| 1327C3..... | 1-a | 0.61/0.54 | 900/1200 |
| 1327C4..... | 1-a | 0.69/0.60 | 900/1200 |
| 1327C5..... | 1-a | 0.65/0.59 | 840/1200 |

astrometrically map different portions of the images into a standard frame in order to stitch together dithered observations.

The transformation of the RCS survey data from raw images to final photometrically and astrometrically calibrated catalogs consists of three major steps. The first is preprocessing, in which typical procedures such as debiasing and flat-fielding are performed. The second major step is object-finding and photometry. The final step, performed using the individual chip-by-chip catalogs output from step two, is to stitch the individual catalogs into a master catalog for each patch using a full photometric and astrometric calibration. Each step consists of a large pipeline, written specifically for these data.

4.1. Pipeline I: Preprocessing

The preprocessing of the RCS survey data was done, for the most part, in the standard manner, using a pipeline implemented within IRAF.³ Each night, or at least during each run, we acquired sets of bias, dark, and twilight flat-field images. Both the bias and dark frames contain very little signal, and so we examined several possibilities in removing their effects. After some experimentation it was found that removal of the dark frame did nothing to improve the uniformity of the images. Moreover, some of the chips contain some columns with significant structure, which was best removed using only bias subtraction (and was often degraded if the dark was also subtracted), and so we settled on simply removing the bias and making no dark current corrections to the images. However, we did continue to acquire dark images in later runs, in order to monitor possible changes in the dark current.

4.1.1. R_C -Band Images

The R_C -band images were processed simply by overscan subtraction, debiasing, and flat-fielding using twilight flats, all in the standard manner. As a final step for data from each night, all available R_C -band images were combined using rejection algorithms to produce a superflat. This was smoothed to eliminate small-scale noise, and all relevant images were re-flattened using this superflat. The resulting R_C -band images typically have variations in the sky of less than 0.3% over a single chip.

4.1.2. z' -Band Images

The z' -band images were overscan corrected, debiased, and flat-fielded using twilight flats similarly to the R_C -band images. However, the z' images suffer from significant fringing effects, so extensive further processing was required. For the CCDs used in the CFH12K, the fringe amplitude can exceed 10% of the total sky signal on the worst CCDs.

One additional complication with defringing these data is that the fringe pattern is not completely stable either in time or across the sky, since natural spatial and temporal variations in the night sky lines cause variations in the corresponding fringe patterns. Apart from variations in the fringes, this can be seen in large variations in the z' sky brightness. Even in the absence of moonlight, the z' sky brightness was observed to vary by factors of 2–3 over a single night. Often this means that the data from an entire night cannot be combined to produce a fringe frame, unlike the case when producing a superflat. After much experimentation, we settled on a procedure for producing fringe

frames in which the fringe frame for a given z' image was constructed from a weighted sum of the all z' frames from that night. The weighting is done according to time, location in the sky, and the overall sky brightness. Frames that are closest in time are given the most weight, typically using a Gaussian weighting function with a σ of ~ 3 hr. Images from the same patch, which are hence nearby, are also given twice the weight of other frames. Finally, input images were also weighted by the difference in the sky levels; for example, an image of half or twice the sky brightness of the target image is assigned half the weight of an image of the same sky brightness.

The standard image combining algorithms in IRAF were found to be insufficient for constructing the weighted fringe frames, and so further code was written to implement a two-step image combine. In this process, all the images to be used in a fringe frame are first approximately flattened using an unweighted fringe frame estimated from the entire night. All pixels brighter than 3 times the standard deviation in the sky pixel values were then masked in each frame, with the masking significantly padded to exclude the low-level extended halos of bright objects. Masked versions of the original z' images were then combined using appropriate weights to construct the fringe frame for each observation.

Each resulting fringe frame was then smoothed with a 3×3 boxcar, and then the appropriate scaling with which to subtract the fringe frame was determined by an iterative analysis of the sky residuals for different scalings. The masked regions established above were also used in this step to ensure that only sky pixels were used in this process.

The resulting defringed z' images are generally very flat, with residual fringes typically having an amplitude of less than 0.5% of the sky. On occasion the fringe residuals are higher—on order of 1%. Further experimentation using different weighting schemes and fringe removal strategies did not result in significant improvement in these frames.

4.1.3. Corrections for Saturation Effects

One final unusual step in the preprocessing of the CFH12K data is a correction implemented for saturation effects. Proper recognition of saturated pixels is important in the object-finding and photometry process, as these pixels must be excluded.

The CFH12K has a number of CCDs that saturate rather strangely. On these CCDs the count value on a saturated pixel actually drops as more charge is gathered, i.e., so that the most saturated portion of a saturated object is in fact measured at a lower count value than less saturated regions. Furthermore, once an object saturates to the point of bleeding, the bleeding columns produced are not at the saturation level of the CCD but at a much lesser level, which in some cases is below the sky level. This makes it nontrivial to establish what pixels are affected by saturation using typical analysis programs.

To circumvent this problem, a separate masking algorithm was established as part of the IRAF preprocessing pipeline. This algorithm is designed to detect and isolate saturated objects by keying on those pixels that are just saturated and hence recognizable because they fall above some predetermined threshold below the actual saturation level. Using these starting pixels, each saturated object was then traced out to a much lower threshold that was empirically determined to be lower than the typical bleeding level for the chip in question. All pixels above this lower threshold are deemed to be saturated, and each object was then reconstructed so that the most central saturated pixels for each object had the highest value, and a value well above the saturation point for the chip. This produces images in which saturated objects appear similar to those on typical CCDs, with

³ IRAF is distributed by the National Optical Astronomy Observatories, which are operated by the Association of Universities for Research in Astronomy, Inc., under cooperative agreement with the National Science Foundation.

the precise manner in which the objects are reconstructed tailored to ensure that photometry pipeline works smoothly. Neither the photometric nor astrometric information for these “reconstructed” objects is correct in detail, however, and we are careful to exclude them from any further analysis. The reconstruction process serves simply to streamline a number of later elements of the reduction pipeline.

4.2. Pipeline II: Object-Finding and Photometry

Object-finding and photometry were performed using the package PPP (Yee 1991) modified to operate in a pipeline mode. Yee (1991) provides detailed descriptions of the algorithms used along with analysis of simulated data demonstrating the characteristics of the algorithms. Further improvements to PPP, motivated by the need for photometric reduction of large imaging database, are described in Yee et al. (1996), as well as Yee et al. (2000). We refer the reader to these papers for more details and present here only a very brief overview of the methods used.

4.2.1. Object Finding

Object finding was performed on weighted sums of the R_C and z' images with the weights based on the signal-to-noise ratio of the input pixels. The R_C and z' images were registered prior to summation by using bright but unsaturated objects in each image. Because of the data acquisition strategy, shifts were typically only a few pixels, for which a simple offset is sufficient. This stacked image was then masked to exclude known hot columns and cosmetic defects, and the bleeding columns from saturated stars. Diffraction spikes are also mapped and excluded based on the positions of bright saturated stars. The image is then smoothed using a 3×3 tapered smoothing box, and all peaks with a net flux averaged over a 3×3 box greater than 2.6σ of the smoothed local sky are selected. This limit corresponds roughly to a 1σ threshold in the unsmoothed image. Each detection is then subject to a number of tests, including a “sharpness” test on the unsmoothed image to reject cosmic rays with full width at half-maximum smaller than 2 pixels, and a size test to reject objects resulting from noise spikes smaller than a point source. The resulting object list, typically 4000–6000 objects per chip, was then eye-checked to ensure that the various masking procedures for diffraction spikes, bleeding columns, and other cosmetic defects have performed properly.

4.2.2. Photometry

The photometry pipeline produces a total magnitude estimate for each detected object in the deeper of the two filters (usually the R_C filter, except for very red objects) by analyzing its photometric curve of growth, which is constructed from a predefined set of circular apertures, with masking of nearby objects as required. In all cases the total magnitude is measured at an “optimal aperture,” deduced by analyzing the shape of the curve of growth (see Yee 1991). This magnitude within the optimal aperture is then corrected to a standard aperture of $8''.5$ diameter (functionally indistinguishable from an infinite aperture for a point source) for objects with the optimal aperture smaller than the standard aperture, using corrections derived from the shape of the growth curves of bright point-source objects. For bright galaxies of larger size, a growth curve up to a maximum diameter of $25''$ is used to determine the optimal aperture to make sure that the bulk of the light is included. We note that very bright galaxies ($R_C < \sim 15$ mag) will in general have underestimated magnitudes because of their larger sizes.

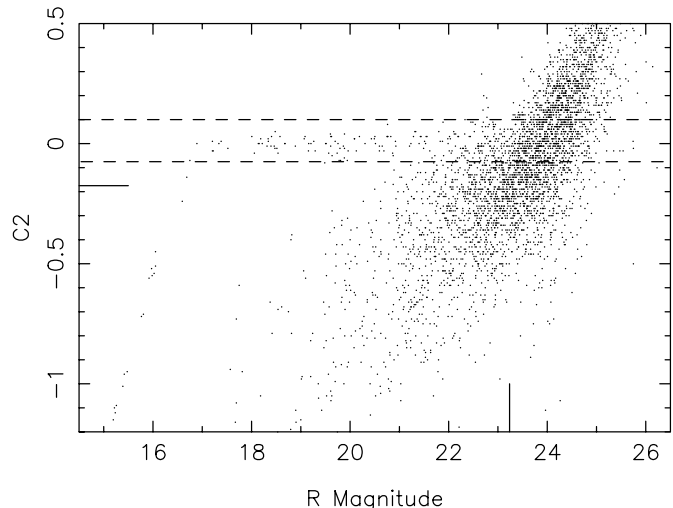


FIG. 3.—Star-galaxy separation example. The R_C band star-galaxy separation plot for chip 10 of the 1326A5 pointing, illustrating the basic elements of star-galaxy separation. The vertical axis is a measure of the compactness (see Yee 1991 for details), which is plotted against R_C magnitude. The short vertical solid line at the bottom of the figure denotes the nominal 100% completeness magnitude for galaxies. The two horizontal dashed lines show the nominal limits in compactness for stars. Bright nonsaturated stars have been used as reference objects. The large collection of less compact objects (below the second dashed line) are galaxies. The bright objects at the extreme left, arranged in a near-vertical line, are saturated stars. Objects above the top horizontal dashed line are more compact than their local PSF and are considered as spurious. At faint magnitudes (largely below the 100% completeness limit), where stars, galaxies, and objects classified as spurious become indistinguishable because of low signal-to-noise ratio, a variable classifier scheme is used in which only a statistically correct percentage of objects on the “compact” edge of the distribution are assigned as stars (see Yee 1991).

The color of each object is estimated separately from the total magnitude, in an aperture (called the color aperture) of either $3''$, or the optimal aperture, whichever is smaller. The total magnitude for the second filter is then computed from the color and the total magnitude of the first filter (see Yee 1991). This assumes that the color gradient within each galaxy produces a negligible effect in the relative total magnitude.

The final photometric catalog for each chip of each pointing has errors on the magnitudes derived from the photon noise in the optimal aperture for each object, summed in quadrature with an “aperture error” of 0.03 mag. This extra error accounts for the uncertainty in estimating the optimal aperture (Yee et al. 1996). Because the galaxies of interest are sky-noise-limited, the photometric uncertainty is computed based on the sky noise within the aperture. The color error is the sum in quadrature of the photon noise for each filter in the color aperture. Using a relatively small color aperture minimizes the error in the color.

4.2.3. Star-Galaxy Separation

Star-galaxy separation is performed by comparing each object to a local set of bright but unsaturated reference stars (Yee 1991; Yee et al. 1996). The star-galaxy separation for a typical field, showing the object compactness versus magnitude, is shown in Figure 3. In all cases the star-galaxy separation is robust for all but the faintest objects (those below the $\sim 100\%$ completeness limit), once the process is checked by eye to eliminate occasional problems with the automatic reference star selection. Star-galaxy separation is performed in both filters separately. The R_C filter is used for the primary classification, since it is generally deeper, but objects that have significantly higher S/N in the z' image are classified using the z' image instead. Note that any cosmic rays

that have passed through the initial object-finding are eliminated by the star-galaxy separation at this stage as they are typically smaller than the measured point spread function. In the final photometric catalog, objects are classified into four categories: galaxies, stars, saturated stars, and spurious “nonobjects” (e.g., cosmic ray detections, cosmetic defects, etc.).

4.3. Pipeline III: Master Catalog Assembly and Calibration

The final step in the RCS data processing is to assemble the chip-by-chip catalogs (in instrumental magnitudes and pixel positions) into an astrometrically and photometrically calibrated master catalog for each patch. This process has a number of steps, detailed below.

4.3.1. Photometric Calibration

The photometric calibration of the RCS data is complicated by the mosaic cameras and variations in those cameras from run to run, and hence a matter for significant discussion. Uniform photometric calibration is particularly important for the RCS, since the accuracy of photometric redshifts is limited by the systematic uncertainty in object colors. Absolute calibration to a particular system is of less concern; uniformity in the photometric calibration ensures accurate photometric redshifts so long as clusters of known redshift are observed within the survey area. Given the scope of the project we have not attempted to measure higher order calibration terms (such as color-dependent air mass terms), since the required effort in gathering standard data would overwhelm the actual gathering of science data in such a case.

With observations in two filters (call these filters i and j), and at the level of precision achievable using the standard data available within the RCS, the goal is to solve the following equation for each object:

$$m_i = m_{ji} + A_{0i} + A_{1i} \times (\text{air mass}) + A_{2ji} \times (m_j - m_i), \quad (1)$$

where m_i , m_j are the magnitudes of the object in the standard system in the filters i and j , m_{ji} is the instrumental magnitude of the object in filter i , A_{0i} is the zero point in filter i , A_{1i} is the extinction coefficient in filter i , and A_{2ji} is the color term transformation coefficient in filter i , referenced to the $j - i$ color. A similar equation governs filter j .

The calibration of CCD mosaic data has the complication that the chips of the mosaic are essentially independent cameras for the purposes of calibration, and so the three basic coefficients needed, per filter, become 36 coefficients for the whole CFH12K mosaic, per filter. Since standard fields are not arranged with mosaics in mind, it is then nontrivial to acquire enough standard data to measure all these coefficients. Fortunately, we expect some of the coefficients to be very similar. First, the air mass terms should be essentially the same for all chips. Second, provided that the individual CCDs have similarly shaped quantum efficiency (QE) curves, the color terms should all be similar. For the CFH12K mosaic, which has two types of CCDs with markedly different QE curves, we can thus reduce the problem to establishing a single air mass term, two color terms, and 12 zero points—per filter.

Observations with the z' filter suffer from a further complication, namely that the filter has until recently been little used, and so the standards available in the literature are rather limited. Since the beginning of RCS observations in 1999 this situation has improved significantly, thanks wholly to the efforts of the SDSS in establishing a new network of primary and secondary

standard fields (Smith et al. 2002) that include the z' filter (Fukugita et al. 1996). The strategy at the telescope for acquiring standards hence evolved from run to run, and moreover, the CFH12K was reconfigured with some new chips between Runs 1 and 2. We note the individual details for each run below.

4.3.2. Photometric Calibration: Run 1

At the time of the first run in 1999 May the SDSS standard star fields were not known to us, and so we relied upon older standards from the literature. The R_C filter was calibrated by observations of Landolt (1992) fields. Fields SA101 and SA110 were repeatedly observed during the run. The z' standards BD +17°4708, Feige 34, Ross 484, and Ross 711 (D. Schneider 1999, private communication) were also observed over the course of the run. In this case the star BD+17°4708 was tiled across the entire mosaic by repeated observations offset to each chip, and other standards were observed when possible. The standard fields were preprocessed using the same pipeline as the science frames, save that the superflat used was the one deduced from the science observations rather than from the images of the standard fields. Standard stars were located and their brightness in a large aperture measured by hand using tools within IRAF, with aperture corrections deduced from bright isolated objects applied to the magnitudes of fainter or somewhat crowded objects for which large measurement apertures were inadvisable.

Despite the allocation of significant observing time at the telescope, particularly to tile the mosaic with z' standards, the total number of standard star measurements was found to be insufficient to measure all the required coefficients with good accuracy. In most cases zero points could be measured individually, but the data for each chip were insufficient to measure either a color or air mass term. We thus adopted a compromise strategy in which we rescaled each chip to the same sky value (using the mean offset in sky values between the chips established from all of the science frames), allowing us to look at the observed standards in ensemble. Notably, this rescaling by the sky value gives chip-to-chip offsets that are within a few percent of the offsets implied by the zero points, hence validating the implicit assumption that the sky has a color similar to the standard stars. Formally, the residual standard deviation in the zero points between chips (after rescaling by the sky) is 0.04 mag in z' and 0.02 in R_C . Notably, the two chips for which multiple z' standards were observed showed internal standard deviations of 0.04 and 0.03 mag between standards, from which we conclude that the residuals in the standard measurements after rescaling are a good estimate of the uncertainty in the calibrations. The final zero points for both filters are thus taken as rescaled versions of the global zero point deduced from all chips. Also, note that the z' data have been calibrated to the SDSS system, since the z' standards observed are also part of the SDSS primary standard set.

Further analysis of this ensemble distribution of standard star measurements demonstrated that the air mass range explored was insufficient to measure the air mass term with good accuracy. The air mass terms used thus come from prior knowledge of the Mauna Kea site, and in R_C the air mass term is the same as that used for the CNOC2 survey data (Yee et al. 2000). To estimate the z' term, we used the scaling between r' and z' from Fukugita et al. (1996), applied to the R_C term. Further accuracy is not required, since the highest air masses in the science observations are approximately 1.5.

The available standard measurements were also used to estimate color terms for the two chip types. Over a range of several magnitudes in $R_C - I_C$ color for the Landolt standards, there was no measurable color term in R_C for either chip type. The z'

standards used span a range of only ~ 1 mag in $i' - z'$, and we similarly could find no color term from these data. Much more extensive data from Run 2 refine these conclusions: the color term in R_C is maximally about 0.001 and consistent with zero, and there are small color terms in z' that differ between the chip types. As we expect the color terms to be stable from run to run, we have retroactively applied the color terms in z' from Run 2 to the data from the appropriate chips in Run 1.

4.3.3. Photometric Calibration: Run 2 and Run 4

The photometric calibration data acquired during these two runs are more extensive than the data in Run 1, both because the run was nearly 4 times as long, and also because the preliminary SDSS calibration lists were available to us by that point. For these runs, only Landolt fields that included SDSS primary standards were observed. Typically, each field was observed more than once during each run, and several fields were observed at several camera positions in an attempt to ensure that some of the relatively sparse SDSS primary standards fell onto each chip.

These data were preprocessed in a manner similar to the data in Run 1. However, noting that the volume of standard data was growing rapidly, we implemented a new procedure for measuring the standards. Essentially, all the standard fields were run through the same object-finding, photometry, and astrometric calibration procedure (described below) as the science data. This ensures that these data are measured uniformly, and also allows us to use automatic algorithms to match the measured objects to the standard lists.

The resulting R_C calibration data for Run 2 (Run 4 is similar) are shown in Figure 4. The vertical axis shows the offset between the computed magnitude (after calibration) and standard magnitudes, versus the $R_C - I_C$ color from the Landolt catalog. The ensemble for “normal” and “red-sensitive” chips are shown, demonstrating the lack of significant color terms in both cases. The error bars shown are the sum in quadrature of the errors in the Landolt catalog and the measurement errors in the RCS data, and hence there may be additional scatter owing to errors in the calibrations on each chip. However, for most chips there are a number of observations of standards, allowing a good estimate of the mean offset. The uncertainty in the mean calibration for each chip is typically in the range 0.015–0.030 mag. These values indicate the fundamental accuracy on a chip-by-chip basis.

Despite a greater number of primary z' standards, and the large number of standard field observations, we found that the z' data from Runs 2 and 4 were, like Run 1, also insufficient to fully characterize the z' photometric solution for the CFH12K.

As in Run 1, we use somewhat nonstandard methods to get around these difficulties. Essentially, we rely on the SDSS data to provide the z' calibration, using data not from the primary standards list, but rather from early release SDSS photometry (Stoughton et al. 2002) of the entire Landolt fields. Despite the fact that these data are not of standard stars per se (in that they have not been measured repeatedly under well-controlled circumstances), the overall excellent quality of the extensive SDSS photometric calibration program ensures that the data are perfectly usable in this manner provided that enough objects are included to guard against secular variations and the like. For example, by a direct comparison of all stellar objects in overlapping calibration fields in Run 2, we derive the calibrations shown in Figure 5. Clearly, the calibration is very good. The zero point for each chip can be established with excellent precision. An examination of the zero point derived from individual observations of standard fields indicates that the ensemble zero points are accurate to better than 0.01 mag. However, the

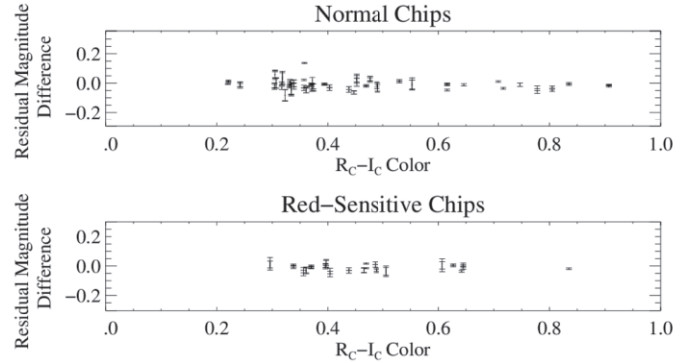


FIG. 4.— R_C calibration for CFHT Run 2. The ensemble residuals between the measured and standard magnitudes for the observed R_C Landolt standards is shown vs. the known $R_C - I_C$ color. No significant color terms are detected for either chip type.

rms uncertainty from observation to observation is typically 0.02 mag. This latter value is indicative of the calibration uncertainty in z' for any given science field observed even under photometric conditions, due likely to variations in atmospheric transmission on relatively short timescales. Note also that there is a small color term in z' that can be measured individually for each chip. Since we expect the primary difference in color terms between chips to be between the two chip types, we have in practice measured two color terms (one for the nine normal chips and one for the three red-sensitive chips).

As a final check of the R_C calibrations we have completed the same comparison to the SDSS early release data in the SDSS r' filter. As expected, there is a significant color term, since the r' filter is bluer than R_C . There are also uncertainties in the matching of the zero points at the level of a few hundredths of a magnitude. This is well within the expected uncertainty of the initial calibration to the Landolt fields. We have thus adjusted the R_C zero-point calibrations (but not color terms) to minimize the scatter with respect to the average zero-point offset between r' and R_C , since the zero point in r' is better determined. Finally, note that the measured color terms when calibrating to r' are essentially the same for both chip types (unlike the z' filter), implying that, as expected, the differences between the chip types are insignificant at these wavelengths.

Finally, we note that the SDSS data used to calibrate these runs are not the final SDSS photometric data (D. Tucker 2000, private communication). Formally, these data are on the $u^*g^*r^*i^*z^*$ system. This system differs from the planned final SDSS system in that color terms have not been applied to the data (owing to unresolved issues in transforming the SDSS monitor telescope and primary telescope cameras to the same photometric system). Systematic differences between the two systems are expected at the level of 0.05 mag. Recalibration of these data will thus be required at some future date, once the SDSS system is fully defined. By then, we expect several other calibration possibilities to exist—either calibration to the SDSS system by direct comparison of the science frames, or by comparison of the standard fields observed by the RCS to the matching SDSS Secondary Calibration Fields. We leave these possibilities to a future paper, coincident with the planned release of the RCS photometry and processed imaging.

The final calibration uncertainties in the photometric calibration for Runs 2 and 4 are about 0.02 mag for the zero points in each filter and 0.001 in the color terms. The color of any given object may thus have systematic uncertainties of about 0.03 mag in $R_C - z'$ color. Run 1 has a somewhat higher uncertainty in the

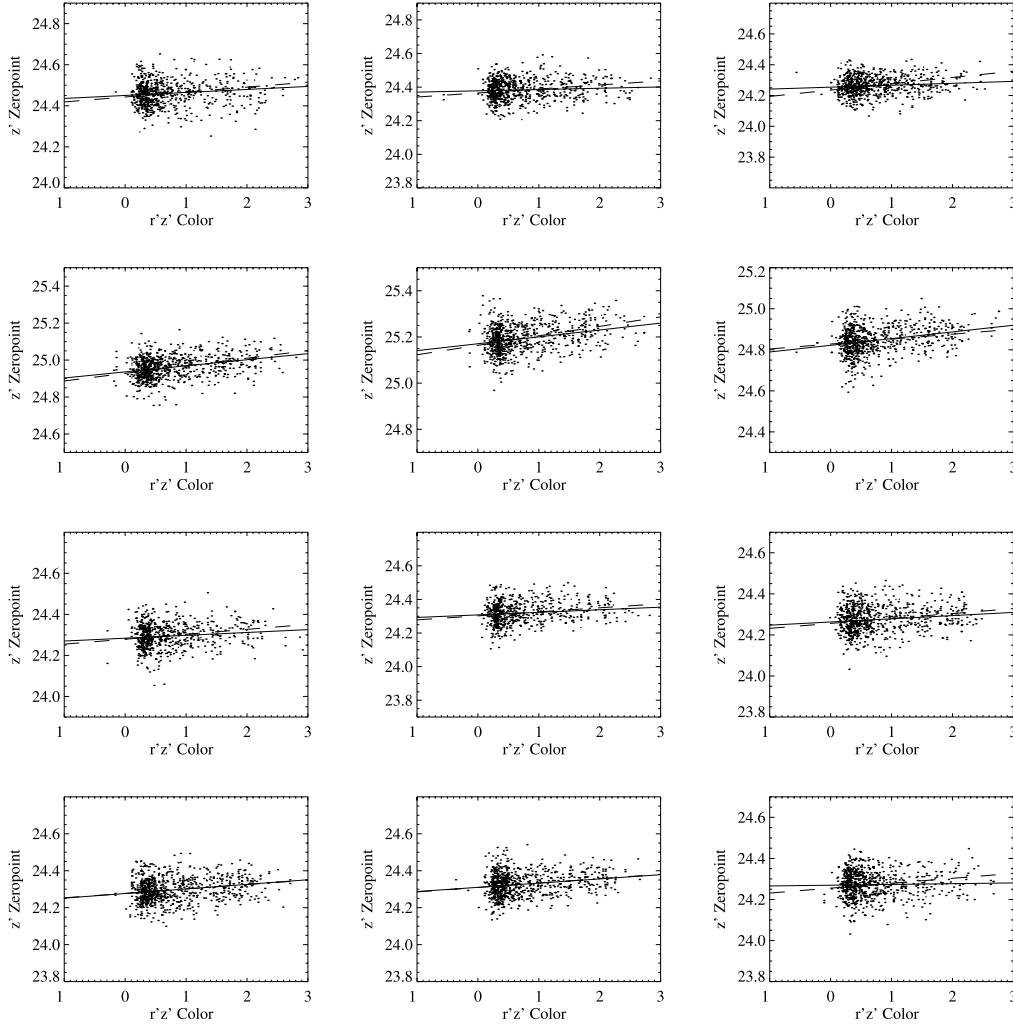


FIG. 5.— z' calibration for CFHT Run 2. The zero point (per ADU per second) vs. $r' - z'$ color for each chip of the CFH12K mosaic, for Run 2, by comparison to SDSS early release data of Landolt (1992) fields. The actual zero points, per electron, are significantly closer to each other than these data would imply since no correction has been made for gain variations between the chips. Chip 1 is in the top right corner, with chip number increasing horizontally and then vertically. The three chips on the second row (chips 4, 5, and 6) are the red-sensitive chips, and clearly have a color term that is different from the other chips. Solid lines indicate the fitted color term on each chip, and dashed lines the adopted color term.

z' calibration of 0.04, and correspondingly higher uncertainty in the color. The mapping of color onto redshift shown in Figure 1 shows that in either case this corresponds to a systematic redshift uncertainty of about 0.01–0.015 for moderate redshifts, and up to 0.05–0.08 at higher redshifts where smaller color changes correspond to larger redshift differences. For purposes of finding clusters, this systematic uncertainty is in all cases comparable to the random uncertainty due to noise in the photometry and uncertainty in the cluster red-sequence modeling (M. D. Gladders & H. K. C. Yee 2005, in preparation).

4.3.4. Astrometric Calibration and Catalog Assembly

The RCS data are astrometrically calibrated using a two-step process. First, images of M67 taken during the run are used to establish the placement of the chips relative to one another within the camera. This is done by running these images through the pipelines described above and then matching the resulting catalogs to astrometry from the USNO-A2.0 catalog (Monet et al. 1998). Each chip is mapped into the camera reference frame separately using a second-order surface polynomial with cross-terms. Typically, 100–200 stars are used on each chip to establish this mapping. This first step stitches all 12 chips of the camera

into a common reference frame and naturally incorporates such effects as camera distortions and rotation. Since the camera has random rotation offsets of about a degree from run to run, this last point is particularly relevant. We also use this distortion map to establish the variation in pixel size across the camera.

The variation in pixel size across the mosaic causes a position-dependent bias in the photometry that must be fixed at this stage. This effect comes about because of flat-fielding, a process that presumes that all pixels are the same size on the sky. If, for example, a given pixel is smaller on the sky than average, then dividing by a flat-field artificially boosts the flux of that pixel. In large mosaic cameras, which occupy a significant fraction of the telescope field and hence have significant distortions, this variation in pixel size must be corrected by normalizing to the pixel area. This is done at the catalog stage for the RCS—unlike in dithered data in which these corrections must be applied to the image directly prior to stacking the images.

The second step of the astrometric calibration maps the camera coordinates onto the sky, again using a match to the USNO-A2.0 catalog. This is done by establishing the nominal center position of the field by visual inspection, followed by an automatic, iterative algorithm that repeatedly matches objects

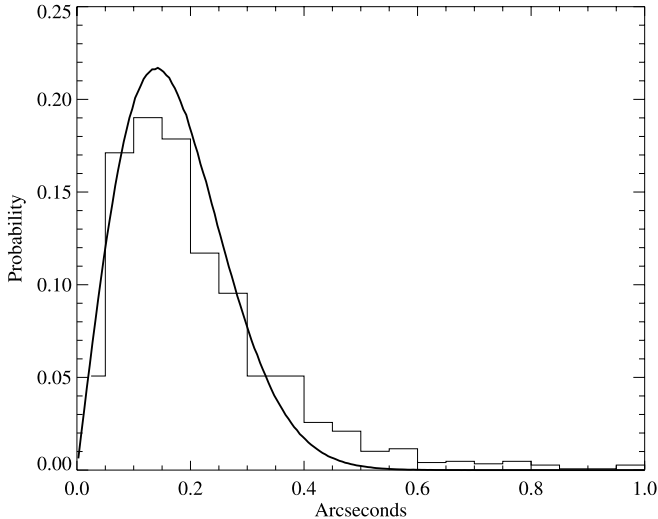


FIG. 6.—Astrometric residuals in comparison to the SDSS. The histogram shows the distribution of residuals between RCS and SDSS positions for moderately bright point sources in the overlapping Landolt calibration fields. This comparison independently shows that the RCS is astrometrically calibrated to subarcsecond precision.

in position and magnitude simultaneously until a satisfactory mapping is achieved across the whole image. Typically, 300–500 stars per pointing are used to establish this final astrometric solution. The final accuracy of the astrometric solution is indicated by the residuals between the positions of objects in the RCS and the USNO-A2.0. Typically, these residuals are one-third of an arcsecond per coordinate, consistent with being dominated by uncertainties in the USNO-A2.0 catalogs. An excellent secondary check of the accuracy of the astrometric solutions is the comparison of positions in the RCS photometric calibration fields to the equivalent SDSS early release data. The comparison between RCS and SDSS positions on three separate Landolt fields is shown in Figure 6. After subtraction of a systematic offset of a few tenths of an arcsecond, the agreement is very good. As shown in Figure 6, this comparison is consistent with an uncertainty between the SDSS and RCS positions of about 140 milliarcsec (mas) per coordinate. The total estimated astrometric uncertainty in the SDSS data is on order of 50–100 mas per coordinate (Stoughton et al. 2002); Figure 6 suggests that the RCS positions for bright but unsaturated objects are uncertain at a similar level.

Once the astrometric solution has been established for each camera pointing, the data must be stitched together to form a master patch catalog. This is done simply by locating the edge of each pointing and then taking the midpoint between the edges of it and the adjacent pointings as the boundary of each pointing. Data outside this boundary are clipped. The boundary also has a $2''$ width, to ensure that objects near the edge of a given pointing do not reoccur across the boundary in data from the adjacent pointing. This results in a negligible loss of area and is insignificant in comparison to the interchip gaps in the camera. Currently, the basic data contained in the master catalogs for each object are position, z' magnitude, $R_C - z'$ color, magnitude and color errors, the original chip coordinates and pointing and chip designations. We expect to add morphological information once this analysis is fully integrated into the data pipeline.

During this final stage, we also create a number of ancillary data products to enable various subsequent analyses. The primary product is a set of random photometric catalogs, useful at later stages for such things as generating random catalogs for

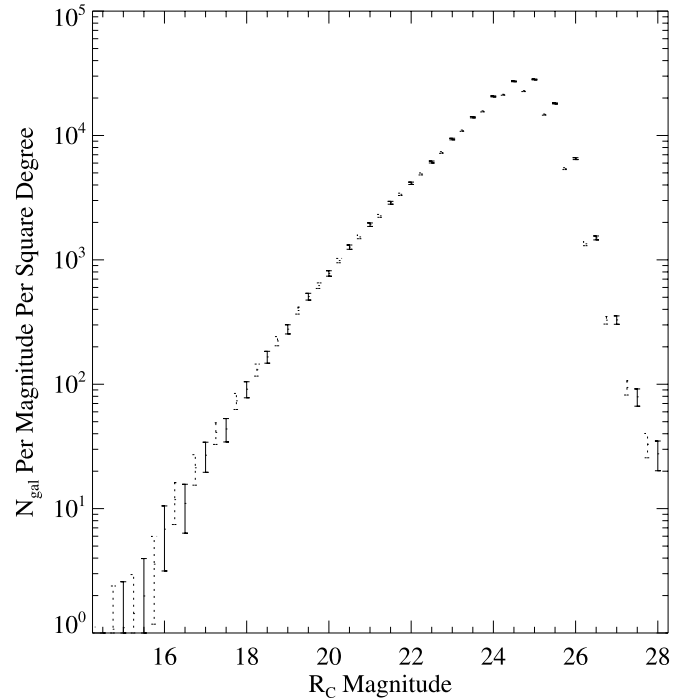


FIG. 7.— R_C galaxy counts. Galaxy counts for the patch RCS 0926+37 (dotted lines) and patch RCS 1327+29 (solid lines) are shown in offset 0.5 mag bins. Error bars as shown are $3\sqrt{N}$. The two patches agree extremely well, apart from differences at the faint end due to slightly different sampling depths.

correlation analyses. These catalogs, which include photometric information, are made by taking photometric data from other pointings with similar depths and assigning random positions to the objects, in the raw chip coordinates. These data are then assembled analogously to the real master patch catalog, using the same interpointing boundaries. We also produce a much larger random catalog of positions only, where each chip is populated by $\sim 3.5 \times 10^5$ objects at semirandom positions, with a modification to the density of points over the chip to account for the varying pixel size in the mosaic camera. This catalog is useful for estimating the contribution of individual chips and pointings to global statistics, in cases where the area rather than the number of objects (and hence image depth) is of concern. In detail this catalog is made by placing points on a nominal grid in which each grid cell has an area of 1 arcsec^2 . A single point is placed at a random position within each grid cell, producing a catalog that has a white spatial power spectrum at fine scales (and so reasonably samples chip edges and other area cutouts) but does not have significant power on large scales (and hence is less noisy than a true random catalog when used to compute area on these larger scales). For example, this semirandom position catalog is used in § 6.2. (deriving cluster richness) to compute the effective area of the survey in arbitrary regions by Monte Carlo methods, with proper accounting for chip gaps and survey edges.

5. DATA FOR PATCHES RCS 0926+37 AND RCS 1327+29

The first two RCS patches for which complete data are available are RCS 0926+37 and RCS 1327+29. Both were imaged during Run 1-a, Run 2, and Run 4. The data sets used for these patches, as previously noted, are tabulated in Tables 3 and 4. The data used here were processed using the pipeline described above. The final assembled patches cover areas of 5.59 and 4.54 deg^2 , respectively.

Figure 7 shows the R_C galaxy counts from the two patches. As expected, the galaxy counts are very similar, with deviations

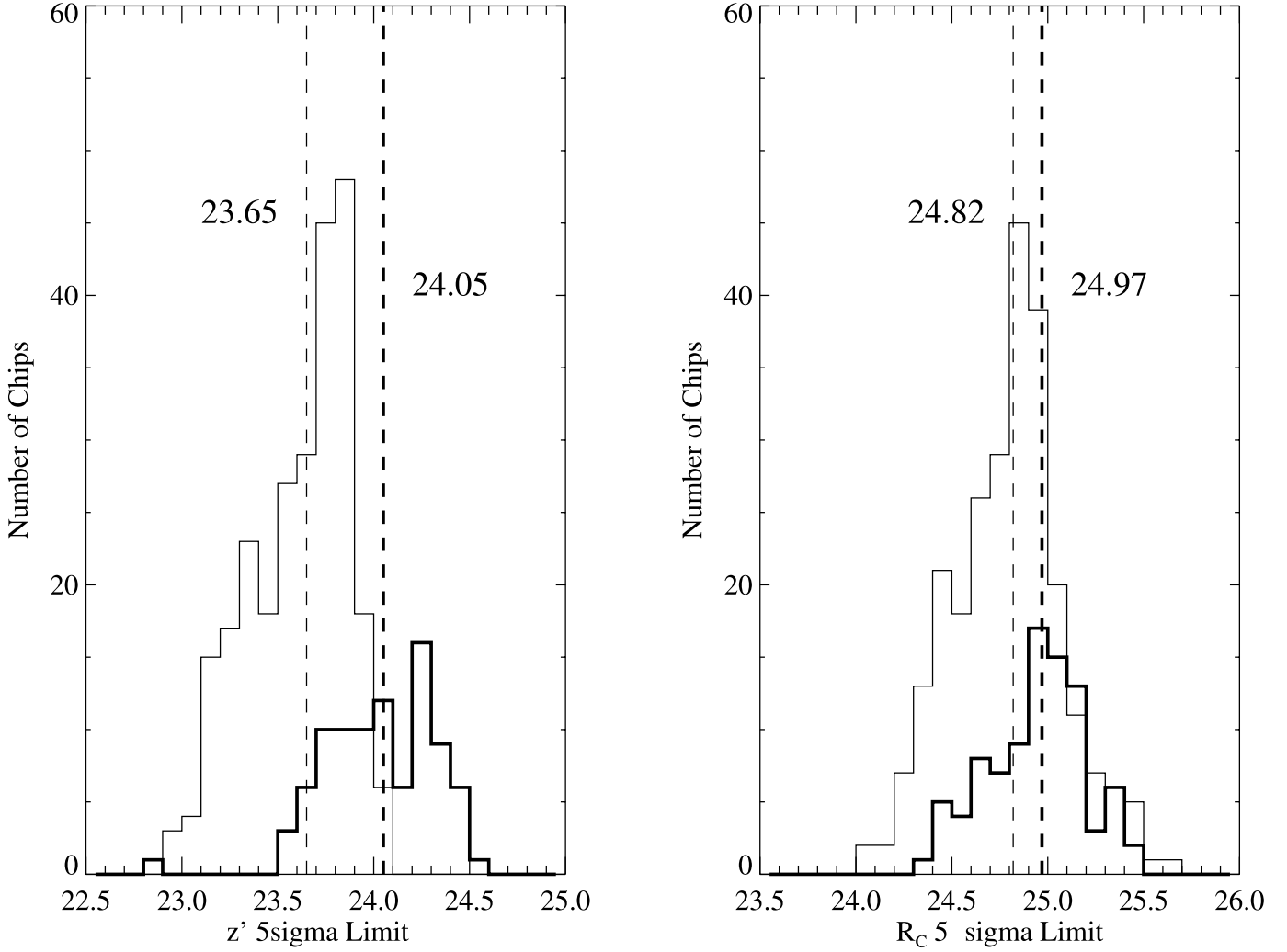


FIG. 8.—Limiting magnitudes in z' and R_C . The distribution of 5σ point source magnitudes from each individual chip for the z' filter (left panel) and the R_C filter (right panel) are shown for both normal (thin lines) and red-sensitive chips (thick line). The median value is shown for each subset.

at the faint end due to differences in image depths between the two patches. From this, it is evident that the typical 100% completeness depth for galaxies is about $R_C \sim 24.0$. Based on extensive past experience, this corresponds to about a 10σ limit for point sources. The target depth for these data was $R_C = 24.6$ at a 5σ limit for point sources; the measured value is $R_C \sim 24.7$, consistent with expectations. The variation in depths on a chip-to-chip basis for both filters is shown in Figure 8, where the 5σ point source limit has been estimated empirically for each chip. Results are shown for both normal and red-sensitive chips. Extensive tests using similar data (Yee 1991) demonstrate that the 100% completeness limit for galaxies is typically 0.7–0.8 mag brighter than the 5σ point source limit, completely consistent with Figures 7 and 8.

Figure 9 shows two color-magnitude diagrams for patch RCS 0926+37—one for a random set of 20,000 stars and the other for a random set of 20,000 galaxies. The markedly different distributions show that the star-galaxy separation works very well.

6. CLUSTER FINDING WITH THE RCS DATA

The basis of the cluster-finding algorithm used to find clusters in the RCS data is given in Gladders & Yee (2000). In brief, this algorithm works by searching for density enhancements in the four-dimensional space of position, color, and magnitude. In

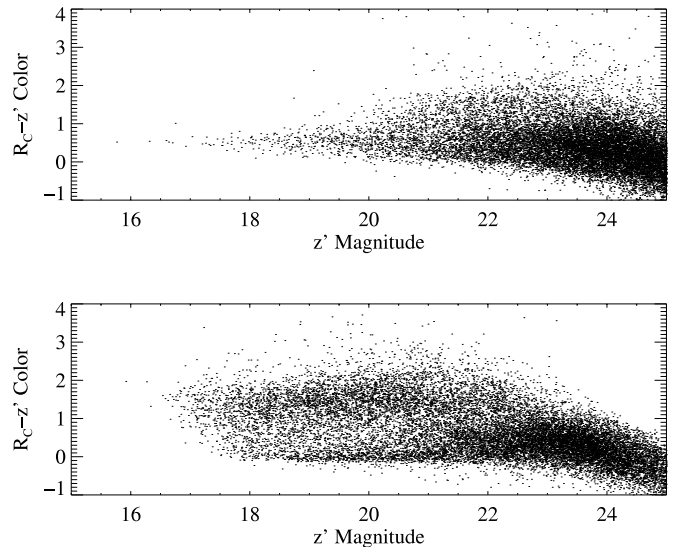


FIG. 9.—Galaxy and star color-magnitude diagrams. $R_C - z'$ vs. z' color-magnitude diagrams are shown for objects classified as galaxies (top) and stars (bottom). The data are a random sample of 20,000 objects from the RCS 0926+37 patch; the number of points is limited in order to show the distribution effectively.

practice, the algorithm works by cutting up the color-magnitude plane for galaxies into a number of overlapping color slices, corresponding to expected cluster red sequences over a range of redshifts. For each slice, the magnitude-weighted density of galaxies is computed using an appropriate smoothing kernel. The density values are translated into Gaussian sigmas by comparison to the distribution of background values in bootstrap maps. The individual slices are assembled into a datacube, which is then searched for significant peaks.

6.1. Algorithm Modifications

We have applied a modified version of the Gladders & Yee (2000) algorithm to the RCS data for patches RCS 0926+37 and RCS 1327+29. The smoothing kernel used is as described in Gladders & Yee (2000), with a core radius of $300 h^{-1}$ kpc, and the algorithm is in most details identical. The two significant changes are an enhancement to the algorithm designed to account for pointing-to-pointing and chip-to-chip variations in RCS images, and a new algorithm for selecting peaks in the final datacube. Each modification is described in detail below.

6.1.1. Algorithm Enhancements to Account for Variations in Survey Data

The complications due to image variations are subtle and must be carefully accounted for. The basic problem is that the sampling depth on any one image from a single chip varies in both filters from all other single chip images in the survey. The depth is a function of the QE of the chip in each filter (this is rather varied in the z' filter, particularly because of the two chip types in the camera) combined with the sky brightness and seeing for each pointing. Moreover, the depths achieved are a function of source type—for example, poor seeing will affect the depths achieved for point sources more than for large galaxies, whereas a brighter sky will have less of an impact on point sources compared to larger galaxies. Also, the QE variations are chip-to-chip (in that the same relative sensitivity is preserved between different chips in the mosaic regardless of sky brightness and seeing variations), and the seeing and sky brightness variations affect the depths on a pointing-to-pointing basis.

A trivial way to correct for these depth variations (which was used in Gladders & Yee 2000, in application to the CNOC2 data) is to simply cut the entire photometric catalog to the depth of the shallowest image in the survey. Clearly, for a large-scale survey this is a nonoptimal approach. Also, unless the cuts are made at rather bright limits this approach does not even work well, because the variations in the photometric uncertainty at the faint end of the distribution still produce statistical differences between different regions of the survey, even when all portions of the survey have the same nominal completeness.

We have extensively explored the idea of using the photometric catalogs with random positions (described in § 4.3.4) to normalize the density maps. The matching random-position photometric catalogs for each chip are generated by drawing photometry from chips of similar depth coupled with random positions and provide data that are in principle statistically similar to the actual data. Nominally, one could then use these data to renormalize in some way the actual data to account for depth variations. In practice we find that this approach is insufficient, in that residual chip-to-chip variations are still evident in the density maps produced by the cluster-finding algorithm.

In order to fully correct these chip-to-chip and pointing-to-pointing variations, we instead use a strategy based on sampling of the actual data. Consider first that each full patch typically consists of a total of 180 (i.e., 15 pointings times 12 chips)

individual pairs of R_C and z' images, each of which has a slightly different sampling depth. If each single chip image were totally isolated on the sky, one could in principle trivially use bootstrap resamplings of only that one image (technically, bootstrap resamplings of the corresponding catalog) to compute the significance of peaks found in the various density maps arising from the different color slices of that catalog. However, apart from the fact that the individual images are not isolated on the sky, this approach is not feasible, since a single large cluster can dominate the signal on a given chip, at least in the color slices corresponding to the cluster's redshift. In practice then, one must isolate regions larger than a single chip that have similar statistics from which one can estimate the significance of any given peak. Thus, for each pixel in a density map, the goal is to locate a subset of all pixels in the map that sample regions with similar statistical properties; the same pixels from a large set of bootstrap resampled maps then provide the necessary background distribution used to compute the significance of the measured value.

Following Gladders & Yee (2000), recall that the kernel-smoothed density map of a given color slice is an array of $n \times m$ pixels, encoding the kernel-smoothed density value, δ_{ij} , at the corresponding location. In practice, because the camera is a tightly packed mosaic, and because the pointings overlap, the smoothing kernel centered at a given location often spans multiple chips or pointings, and so the measured δ_{ij} at that point is typically influenced by several data sets each with slightly different depth. The value of δ_{ij} at any given location is then a reflection of the local density of galaxies of a given color at that position, and the sampling depth of the data sets that contribute to that measured density. To establish which other pixels in the maps to use as backgrounds, we want to somehow average over the region of the data set corresponding to each particular observation, and then use only pixels of similar sampling depths (indicated by having a similar average value of δ_{ij}) when computing the significance of the measured δ_{ij} -values. There are likely two partitions of the data in a given patch that are significant—one corresponding to the individual pointings (nominally 15 regions per patch) and one corresponding to the individual chips (nominally 12 regions per patch). In principle we are thus interested in deducing a total of 180 “average values” from the input map of δ_{ij} -values, where each average value corresponds to a given chip and pointing combination and can be estimated from a region of the input map. In practice this number is often larger since data from each run is considered separately because of significant changes in the instrument from run to run.

To find the appropriate portion of the input map from which to estimate a given average value, we turn to the random position-only catalog described in § 4.3.4. In this catalog each chip on each pointing is represented by a semirandom distribution (in the original chip pixel coordinates) of $\sim 3.5 \times 10^5$ points with no associated photometry. These positions are run through the same master catalog assembly process and produce a position-only master catalog that precisely reproduces the overlap cuts that are used when stitching the pointings together. The contribution of any one chip to the map can be estimated from this catalog simply by applying the same density estimator used in creating the real-data density map to the random points that come from only that chip. We use this random catalog, in conjunction with the actual input catalog, to estimate the “average value” of each pixel in the input map (call the input density map $M1$). This is done in a two discreet stages.

First, we want to produce a map, called $M2$, which represents the average value of each pointing in $M1$. To do this, we consider

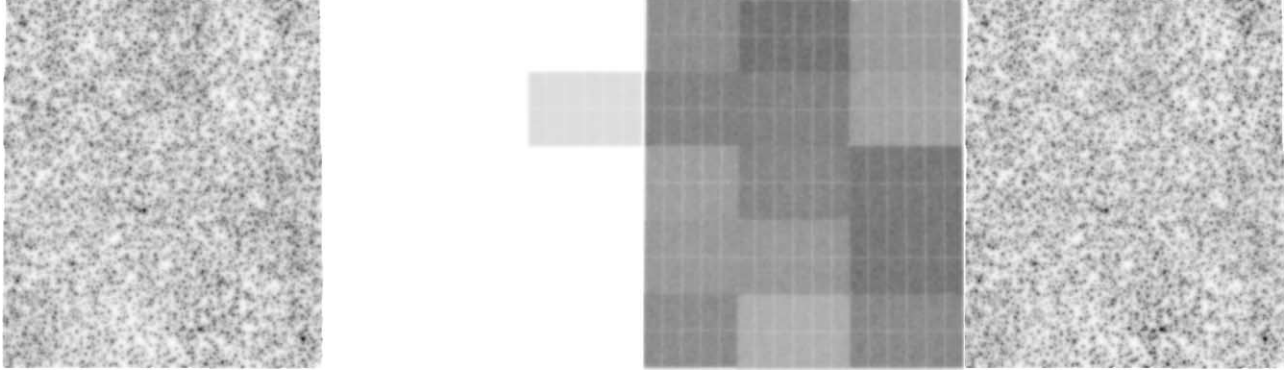


FIG. 10.—Correcting for pointing-scale survey variations. The four gray-scale panels, described in detail in the text, show the input map $M1$ (left), an example map of W_{ij}^P (center left), the map $M2$ (center right), and the resulting map $M1'$ (right).

each pixel in $M1$ as a measure of the sum of a contribution from each pointing. Algorithmically, we construct a highly overdetermined set of $i \times j$ linear equations (one for each pixel) in which we presume that each measured δ_{ij} is given by

$$\delta_{ij} = \sum_{P=1}^{15} W_{ij}^P A^P, \quad (2)$$

where W_{ij}^P is the weight (calculated from the position-only catalog) of the P th pointing at pixel i, j , and A^P is the average value of the P th pointing. The A^P -values (15 of them for a typical full patch) are unknowns. We solve this using singular-value decomposition and hence recover optimal estimates for the A^P -values. These A^P -values are then used to create a density map, via equation (2), of δ'_{ij} -values, which is a map of the pointing-averaged value at each pixel. This is the desired map $M2$. $M1$ is then divided by $M2$ to produce a map (call it $M1'$) that is devoid, on average, of variations on a pointing-to-pointing basis.

Figure 10 illustrates the generation of the map $M2$ and $M1'$ in more detail. The left panel shows the input map $M1$, in this case corresponding to a color slice for the z range 0.555–0.575 in patch RCS 1327+29. The center left panel shows an example map of W_{ij}^P , in this case for the A2 pointing. Nominally 15 such maps are generated from the position-only random catalogs, in order to set up equation (2). The center right panel shows the resulting map $M2$, and the right panel shows the map $M1'$.

We next apply a similar procedure to $M1'$ in order to produce the average value of each chip in $M1'$ (we will call this map

$M3$). In this case, “chip” refers to all occurrences of a given chip of the mosaic within the entire patch. In practice, this means solving for a number of further unknowns akin to the A^P -values in equation (2). These unknowns correspond to chips from each run contributing to the patch; each run is treated independently because the camera used underwent continual refits during the course of the survey. We again solve for these average values using singular-value decomposition of a highly overdetermined set of $m \times n$ linear equations, and from this deduce the map $M3$.

The product of maps $M2$ and $M3$ yields a map, call it $M4$, which gives the average value of the δ_{ij} -values across each chip on each pointing in $M1$, where each average has been estimated over an area significantly larger than a single chip (solving the problem of a large cluster dominating in a small region) and each averaged pixel properly accounts for the relative contributions of all chips and pointings. From this, each value of δ_{ij} in $M1$ can be transformed into a probability by using only those portions of the bootstrap background maps that have similar average values in $M4$. This ensures that the significance of any given peak is assessed only in comparison to data of similar depths.

Similarly to Figure 10, Figure 11 illustrates the generation of the maps $M3$ and $M4$. The input map, $M1'$, is the rightmost panel of Figure 10. The left panel of Figure 11 shows an example map of W_{ij}^P , in this case for chip 2 in the data corresponding to Run 2 (for a total of 10 occurrences of this chip in this particular patch—see Table 4). There are total of 22 such maps for this patch, since there are data from both Run 1-a (10 chips) and Run 2 (12 chips). The resulting map of average values across chips, $M3$, is shown

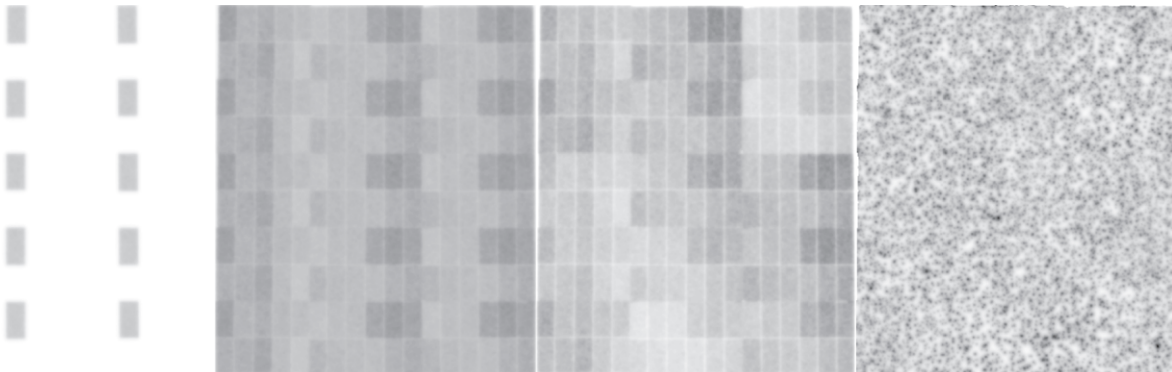


FIG. 11.—Correcting for chip-scale survey variations. The four gray-scale panels, described in detail in the text, show an example map of W_{ij}^P (left), the map $M3$ (center left), the map $M4$ (center right), and the normalized map $M1/M4$ (right).

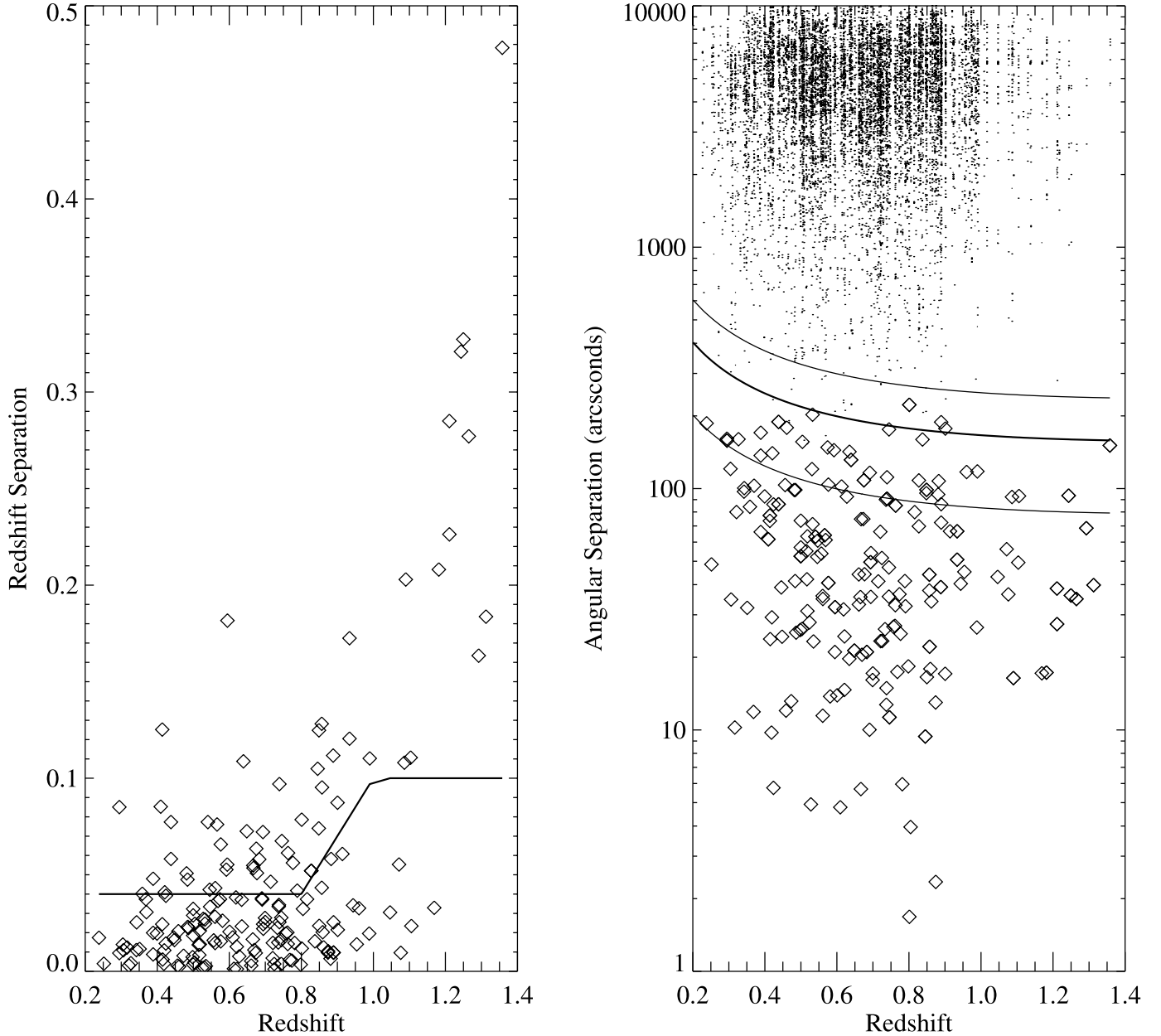


FIG. 12.—Redshift and angular separation of subpeaks. The left panel shows the redshift separation of all pairs of subpeaks within a single primary peak, for the patch RCS 1327+29. The solid line shows the typical expected redshift uncertainty, based on the simulations in M. D. Gladders & H. K. C. Yee (2005, in preparation), and taking into account systematic photometric errors. The right panel similarly shows the angular separation. Angular separations for all possible pairs of primary peaks are also shown, as dots. The solid lines show the apparent angular size of 0.5 , 1.0 , and $1.5 h^{-1}$ physical Mpc. These plots demonstrate that the connected subpeaks represent a population that is consistent with being subclumps of a single cluster, since their redshifts are statistically identical and their projected separations typically smaller than the virial radius of a cluster.

in the center left panel. The map $M4$ (the product of maps $M2$ and $M3$) is shown in the center right panel. The right panel shows the map $M1$ (see Fig. 10, *left panel*) divided by $M4$. Note that any apparent structure on both chip scales and pointing scales is now negligible.

6.1.2. Identifying Cluster Candidates

The other major change from the algorithm developed in Gladders & Yee (2000) is the method used to find peaks in the datacube of σ_{ij} -values. In Gladders & Yee (2000) we used the readily available three-dimensional peak finding algorithm of Williams et al. (1994) to select significant peaks in the datacube and to separate nearby peaks. Further experimentation has shown, however, that the separation of nearby peaks is better accom-

plished using a more physically motivated model, and so a special purpose method was developed.

The final peak-finding algorithm is relatively simple. Peaks are identified by finding the highest-valued voxel in the datacube, and then iteratively connecting all adjacent voxels down to a chosen threshold. This process is iterated, ignoring all previously flagged voxels, until all “significant” peaks are flagged. The significance cut is an arbitrarily chosen value that attempts to balance completeness and contamination in the catalog. In this paper we use a cut of 3.29σ (corresponding to a nominal 1 in 1000 chance of random occurrence). Each peak above this level is traced down to a lower threshold of 2.5σ .

This simple-minded approach can and does connect subpeaks that appear somewhat separated in the datacube. To investigate

the physical significance of these peaks, we have developed a modified algorithm capable of breaking up a single region connected at a relatively low threshold into its constituent subpeaks. Figure 12 plots the angular and redshift separations of all possible pairs of peaks identified by this modified analysis, applied to the patch RCS 0926+37. Two sets of values are plotted: those which correspond to pairs of subpeaks that are within a single primary peak, and those which correspond to pairs of separate primary peaks. Both in angular coordinates and redshift, this provides a natural separation in scale. Notably, for the angular separations the dividing region between the two scales is close to the expected virial radius for clusters. Furthermore, in redshift space the division appears to correspond to the expected redshift uncertainty for individual clusters at all but the highest redshifts. At the highest redshifts individual peaks are at a generally lower signal-to-noise ratio, and redshifts may be more systematically uncertain than simple models indicate (see § 6.2.2), and the excess difference between subpeaks at these extreme redshift is likely not significant. Thus, in almost all cases, connected subpeaks are in fact closer in projected separation than the size of a single cluster, and generally indistinguishable in redshift. Moreover, separate primary peaks are almost never so close. We thus choose, on reasonable physical grounds, to call all such connected subpeaks a single cluster.

6.1.3. Uncertainties in the Significance of Cluster Candidates

The significance of a given cluster has some associated uncertainty, which derives in part from computational limits. This computational uncertainty is separate from uncertainty in the significance (and other derived quantities such as redshift) that derives from, for example, photometric uncertainty in the input data. The latter is difficult to quantify in the absence of repeated imaging of the same area of sky but is likely to be small for most cluster candidates since the cluster signal is an aggregate from many objects. The computational uncertainty can be readily quantified, however, and is primarily due to the limited number of bootstrap realizations that can be reasonably computed. Consider, for example, that a $\sim 5\sigma$ peak is roughly a one in one million event. Thus, to make a measurement of a 5σ peak at a signal-to-noise ratio (SN) of 10 requires about 100 million bootstrap samples. If one uses only a tenth of each bootstrap map to compute the significance of any given pixel in the input map (i.e., as described in detail in § 6.1.1) then about 10^9 bootstrap map pixels are needed to describe each possible 5σ peak at a SN of 10. These computational limits motivated Gladders & Yee (2000) to use a fitted version of the distribution of δ_{ij} -values in the bootstrap maps, in attempt to suppress noise in the final significance maps. We use a similar procedure here, but apply a fitting function to only the high-valued end of the distribution, where the bootstrap maps are insufficiently well sampled. Below approximately 4σ , the actual distribution of bootstrap values is used to compute significance, and above about 4.5σ the fitted distribution is used, with a transition region in between these values where a weighted mean of both is used.

Figure 13 shows an estimate of the uncertainty in the significance of voxel values in the datacube for patch RCS 0926+37. This has been computed by comparing the voxel values across different runs of the cluster-finding algorithm. Note the general increase in uncertainty toward higher values of σ ; the use of a fitting function to the bootstrap distributions suppresses pixel-to-pixel noise in a given slice in a particular datacube but does not suppress the noise across different runs of the bootstrap analysis. It is important to note in this analysis that the computational uncertainty in σ at any given value of σ is always much less than

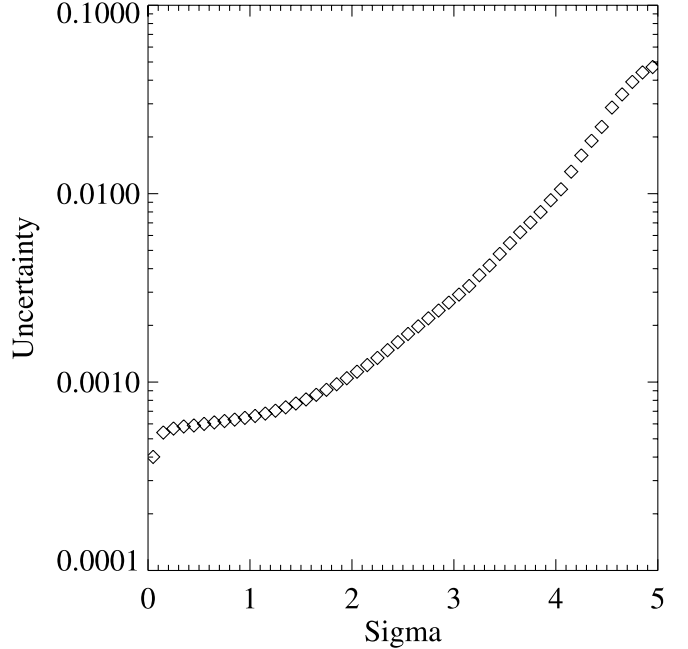


FIG. 13.—Computational uncertainty in significance maps. The uncertainty in the significance of voxel values in the patch RCS 0926+37, computed from the standard deviation about the mean value across a set of runs of the cluster finding in that patch. The primary source of the uncertainty is the limited number of bootstrap realisations.

the difference between the values of σ and the $\sim 3\sigma$ threshold used to define the catalogs, and that at this threshold the uncertainty in σ is extremely small. Thus, in the catalogs described below, the uncertainty in σ has no significant effect on the inclusion of objects in the catalog.

6.2. Two Catalogs of RCS Clusters

6.2.1. The Catalogs

Tables 5 and 6 give the cluster catalogs for patches RCS 0926+37 and RCS 1327+29, respectively, ordered by redshift, to a significance cut of 3.29σ . The peak significance of each cluster is given. Each cluster is identified with a name of the format RCS JHHMMSS+DDMM.m, with coordinate values truncated, as suggested by IAU nomenclature conventions. Clusters are listed only at redshifts greater than 0.20. The redshift accuracy at lower redshifts is compromised by the RCS filters. We are in the process of integrating complementary *B*- and *V*-band data in to the RCS databases; once available these data will be used to define a lower redshift complement to the catalogs presented here. Precise positions for each candidate are provided in J2000.0 coordinates. The final positions are found using an iterative centroiding algorithm using a three-dimensional Gaussian kernel applied to the datacube. The centering kernel has a spatial full width at half-maximum of $250 h^{-1}$ Mpc and has a σ width in redshift of 1.5 voxels. The voxel with the maximum value within the identified peak is used as the starting point for centering.

We also provide in Tables 5 and 6 the offset in arcseconds between this final position and the position of the brightest cluster galaxy. This galaxy is selected by considering all galaxies that are interior to the projected 2.5σ boundary in the datacube that defines the cluster candidate, and that have colors within $(0.2^2 + \Delta C^2)^{1/2}$ magnitudes of the expected red sequence color at the cluster redshift, where ΔC is the color error of each galaxy. The minimal cutoff of 0.2 mag in color is the same as that

TABLE 5
CLUSTERS IN THE PATCH RCS 0926+37

| Cluster | R.A. (J2000) | Decl. (J2000) | z | Δz | Δ BCG (arcsec) | Size (arcsec) | ϵ | σ_{peak} | $B_{\text{gc}T}$ (Mpc ^{1.8}) | $B_{\text{gc}R}$ (Mpc ^{1.8}) |
|--------------------------|--------------|---------------|-------|------------|--------------------------|------------------|------------|------------------------|---|---|
| RCS J092445+3628.1 | 09 24 45.70 | +36 28 11.6 | 0.202 | 0.037 | 20.6 | 44.0 | 0.368 | 3.58 | 495 ± 187 | 393 ± 164 |
| RCS J092414+3710.2 | 09 24 14.00 | +37 10 15.3 | 0.220 | 0.037 | 348.9 | 194.0 | 0.643 | 4.92 | 758 ± 217 | 706 ± 200 |
| RCS J092540+3626.8 | 09 25 40.70 | +36 26 49.8 | 0.233 | 0.037 | 25.6 | 138.2 | 0.225 | 6.00 | 798 ± 223 | 797 ± 209 |
| RCS J092343+3804.1 | 09 23 43.00 | +38 04 09.6 | 0.251 | 0.037 | 9.9 | 33.1 | 0.027 | 3.77 | 199 ± 164 | 178 ± 139 |
| RCS J093004+3828.5 | 09 30 04.80 | +38 28 30.2 | 0.262 | 0.037 | 141.2 | 124.6 | 0.261 | 4.40 | 910 ± 237 | 899 ± 220 |
| RCS J093115+3638.4 | 09 31 15.70 | +36 38 24.7 | 0.270 | 0.037 | 11.8 | 27.9 | 0.026 | 3.71 | 421 ± 193 | 340 ± 161 |
| RCS J092536+3800.3 | 09 25 36.50 | +38 00 21.6 | 0.275 | 0.037 | 14.6 | 56.1 | 0.449 | 3.55 | 501 ± 201 | 369 ± 164 |
| RCS J092523+3708.7 | 09 25 23.70 | +37 08 43.1 | 0.275 | 0.037 | 18.4 | 63.7 | 0.436 | 3.68 | 538 ± 205 | 500 ± 179 |
| RCS J092836+3747.9 | 09 28 36.30 | +37 47 56.7 | 0.299 | 0.037 | 202.2 | 147.6 | 0.156 | 6.19 | 3443 ± 400 | 2263 ± 321 |
| RCS J092245+3631.1 | 09 22 45.70 | +36 31 11.1 | 0.301 | 0.037 | 61.9 | 84.9 | 0.343 | 5.04 | 1209 ± 266 | 845 ± 215 |
| RCS J092644+3643.2 | 09 26 44.30 | +36 43 16.0 | 0.303 | 0.038 | 31.1 | 98.6 | 0.613 | 3.73 | 601 ± 216 | 618 ± 192 |
| RCS J092405+3653.1 | 09 24 05.00 | +36 53 08.9 | 0.303 | 0.038 | 7.0 | 24.4 | 0.121 | 3.34 | 67 ± 159 | 17 ± 114 |
| RCS J092401+3744.3 | 09 24 01.30 | +37 44 21.3 | 0.310 | 0.038 | 12.2 | 32.0 | 0.162 | 4.11 | 297 ± 187 | 243 ± 148 |
| RCS J092517+3703.9 | 09 25 17.30 | +37 03 54.7 | 0.310 | 0.038 | 18.1 | 75.2 | 0.493 | 3.86 | 220 ± 178 | 299 ± 156 |
| RCS J092513+3731.2 | 09 25 13.50 | +37 31 13.2 | 0.311 | 0.038 | 50.4 | 143.2 | 0.575 | 5.77 | 700 ± 226 | 659 ± 197 |
| RCS J092121+3844.8 | 09 21 21.70 | +38 44 51.0 | 0.312 | 0.038 | 42.2 | 47.1 | 0.508 | 3.33 | 378 ± 196 | 378 ± 166 |
| RCS J092907+3757.2 | 09 29 07.40 | +37 57 13.4 | 0.314 | 0.038 | 10.9 | 109.7 | 0.548 | 4.02 | 601 ± 217 | 589 ± 189 |
| RCS J092918+3747.8 | 09 29 18.00 | +37 47 50.9 | 0.328 | 0.038 | 59.7 | 113.5 | 0.226 | 3.86 | 561 ± 216 | 256 ± 151 |
| RCS J092232+3833.9 | 09 22 32.30 | +38 33 59.6 | 0.338 | 0.038 | 38.4 | 73.3 | 0.565 | 3.74 | 592 ± 221 | 576 ± 188 |
| RCS J092705+3720.3 | 09 27 05.20 | +37 20 22.3 | 0.342 | 0.035 | 66.1 | 38.4 | 0.237 | 4.28 | 507 ± 213 | 379 ± 166 |
| RCS J093026+3614.9 | 09 30 26.10 | +36 14 56.4 | 0.343 | 0.035 | 7.4 | 36.4 | 0.225 | 3.55 | 396 ± 203 | 417 ± 170 |
| RCS J092310+3808.5 | 09 23 10.80 | +38 08 31.6 | 0.344 | 0.038 | 23.4 | 100.1 | 0.570 | 4.17 | 466 ± 210 | 298 ± 156 |
| RCS J092735+3829.1 | 09 27 35.00 | +38 29 06.9 | 0.349 | 0.035 | 10.7 | 33.0 | 0.097 | 3.80 | 138 ± 177 | 98 ± 127 |
| RCS J092401+3647.3 | 09 24 01.50 | +36 47 21.2 | 0.353 | 0.035 | 12.0 | 66.6 | 0.516 | 4.01 | 777 ± 239 | 618 ± 193 |
| RCS J092110+3815.9 | 09 21 10.90 | +38 15 55.9 | 0.356 | 0.035 | 26.2 | 34.3 | 0.163 | 3.99 | 414 ± 207 | 417 ± 171 |
| RCS J092123+3836.2 | 09 21 23.30 | +38 36 16.9 | 0.359 | 0.032 | 25.8 | 28.8 | 0.118 | 3.30 | 89 ± 173 | 218 ± 145 |
| RCS J092821+3646.5 | 09 28 21.80 | +36 46 31.8 | 0.361 | 0.038 | 9.0 | 74.5 | 0.250 | 6.19 | 1451 ± 291 | 1260 ± 250 |
| RCS J092335+3826.8 | 09 23 35.60 | +38 26 51.8 | 0.367 | 0.035 | 13.5 | 79.3 | 0.581 | 3.54 | 200 ± 187 | 339 ± 161 |
| RCS J092621+3704.8 | 09 26 21.20 | +37 04 49.4 | 0.371 | 0.032 | 6.4 | 31.3 | 0.354 | 3.37 | 157 ± 183 | 96 ± 127 |
| RCS J092847+3821.6 | 09 28 47.60 | +38 21 37.0 | 0.373 | 0.035 | 6.3 | 85.5 | 0.659 | 3.82 | 356 ± 204 | 376 ± 166 |
| RCS J092121+3825.3 | 09 21 21.50 | +38 25 19.9 | 0.375 | 0.035 | 30.6 | 39.9 | 0.295 | 3.64 | 552 ± 223 | 257 ± 150 |
| RCS J093025+3713.6 | 09 30 25.10 | +37 13 36.6 | 0.376 | 0.032 | 36.6 | 55.2 | 0.492 | 3.56 | 111 ± 179 | 217 ± 145 |
| RCS J093027+3645.5 | 09 30 27.90 | +36 45 34.1 | 0.379 | 0.032 | 25.9 | 28.7 | 0.260 | 3.41 | 309 ± 200 | 216 ± 145 |
| RCS J092315+3609.6 | 09 23 15.90 | +36 09 40.1 | 0.392 | 0.032 | 7.5 | 33.4 | 0.242 | 3.95 | 353 ± 207 | 339 ± 161 |
| RCS J092225+3756.9 | 09 22 25.50 | +37 56 58.0 | 0.394 | 0.038 | 11.8 | 47.6 | 0.275 | 3.78 | 614 ± 231 | 658 ± 197 |
| RCS J092344+3720.2 | 09 23 44.60 | +37 20 17.0 | 0.395 | 0.038 | 14.8 | 56.1 | 0.521 | 3.44 | 572 ± 228 | 497 ± 180 |
| RCS J093019+3748.2 | 09 30 19.30 | +37 48 12.6 | 0.401 | 0.032 | 16.7 | 58.2 | 0.446 | 3.37 | 639 ± 235 | 355 ± 163 |
| RCS J092242+3619.7 | 09 22 42.70 | +36 19 44.8 | 0.401 | 0.031 | 3.8 | 24.3 | 0.208 | 3.32 | −45 ± 172 | 166 ± 138 |
| RCS J092834+3718.8 | 09 28 34.30 | +37 18 51.1 | 0.402 | 0.032 | 13.3 | 56.8 | 0.213 | 4.81 | 989 ± 263 | 854 ± 216 |
| RCS J093113+3622.2 | 09 31 13.10 | +36 22 15.9 | 0.411 | 0.031 | 14.9 | 48.3 | 0.151 | 4.64 | 433 ± 218 | 582 ± 188 |
| RCS J093051+3739.4 | 09 30 51.50 | +37 39 29.0 | 0.416 | 0.031 | 4.5 | 75.0 | 0.649 | 3.37 | 910 ± 259 | 615 ± 191 |
| RCS J092600+3816.4 | 09 26 00.10 | +38 16 26.7 | 0.419 | 0.031 | 2.0 | 95.5 | 0.703 | 4.26 | 424 ± 219 | 261 ± 150 |
| RCS J093038+3700.8 | 09 30 38.60 | +37 00 48.6 | 0.421 | 0.028 | 24.3 | 23.1 | 0.219 | 3.32 | 102 ± 187 | 60 ± 121 |
| RCS J092243+3612.6 | 09 22 43.80 | +36 12 41.5 | 0.422 | 0.031 | 29.9 | 46.4 | 0.345 | 3.58 | 180 ± 196 | 209 ± 142 |
| RCS J092249+3731.1 | 09 22 49.10 | +37 31 08.0 | 0.423 | 0.032 | 65.3 | 52.2 | 0.426 | 3.82 | 672 ± 241 | 478 ± 176 |
| RCS J092222+3841.3 | 09 22 22.30 | +38 41 21.8 | 0.423 | 0.031 | 22.2 | 54.5 | 0.422 | 3.59 | 338 ± 212 | 263 ± 150 |
| RCS J092900+3818.4 | 09 29 00.50 | +38 18 29.3 | 0.423 | 0.032 | 4.3 | 59.1 | 0.152 | 5.67 | 940 ± 262 | 905 ± 219 |
| RCS J093043+3622.6 | 09 30 43.90 | +36 22 40.9 | 0.426 | 0.028 | 10.9 | 57.7 | 0.452 | 3.72 | 376 ± 216 | 302 ± 155 |
| RCS J092118+3829.1 | 09 21 18.00 | +38 29 08.7 | 0.426 | 0.028 | 11.7 | 29.6 | 0.343 | 3.40 | 215 ± 200 | 222 ± 145 |
| RCS J093044+3800.8 | 09 30 44.40 | +38 00 49.9 | 0.433 | 0.028 | 7.3 | 38.5 | 0.278 | 4.08 | 243 ± 205 | 386 ± 165 |
| RCS J092229+3759.2 | 09 22 29.00 | +37 59 13.5 | 0.433 | 0.028 | 9.4 | 20.3 | 0.115 | 3.37 | 323 ± 213 | 185 ± 139 |
| RCS J092212+3739.4 | 09 22 12.00 | +37 39 26.4 | 0.438 | 0.025 | 31.2 | 35.5 | 0.375 | 3.30 | 332 ± 214 | 294 ± 154 |
| RCS J092322+3653.2 | 09 23 22.20 | +36 53 15.6 | 0.446 | 0.025 | 7.6 | 19.7 | 0.105 | 3.30 | 84 ± 192 | 137 ± 131 |
| RCS J092432+3726.3 | 09 24 32.70 | +37 26 21.3 | 0.447 | 0.025 | 125.1 | 84.8 | 0.671 | 3.52 | 467 ± 228 | 186 ± 138 |
| RCS J092809+3754.8 | 09 28 09.50 | +37 54 50.5 | 0.450 | 0.031 | 3.6 | 67.4 | 0.148 | 5.22 | 936 ± 228 | 885 ± 195 |
| RCS J093128+3841.8 | 09 31 28.60 | +38 41 53.5 | 0.450 | 0.025 | 16.1 | 39.4 | 0.404 | 3.47 | 241 ± 173 | 189 ± 127 |
| RCS J092949+3743.5 | 09 29 49.20 | +37 43 30.8 | 0.451 | 0.025 | 31.2 | 21.9 | 0.056 | 3.67 | 617 ± 205 | 191 ± 126 |
| RCS J092154+3638.2 | 09 21 54.00 | +36 38 15.5 | 0.454 | 0.028 | 34.3 | 64.1 | 0.422 | 4.02 | 773 ± 217 | 474 ± 158 |
| RCS J092223+3637.0 | 09 22 23.70 | +36 37 00.1 | 0.458 | 0.025 | 6.5 | 22.8 | 0.154 | 3.35 | 294 ± 180 | 191 ± 126 |
| RCS J093020+3843.5 | 09 30 20.00 | +38 43 35.7 | 0.469 | 0.025 | 21.5 | 42.3 | 0.442 | 3.79 | 230 ± 176 | 274 ± 137 |
| RCS J092223+3750.4 | 09 22 23.60 | +37 50 28.4 | 0.470 | 0.025 | 28.3 | 46.3 | 0.211 | 4.19 | 723 ± 216 | 538 ± 164 |
| RCS J092741+3729.2 | 09 27 41.90 | +37 29 17.8 | 0.474 | 0.023 | 11.4 | 20.2 | 0.067 | 3.50 | 148 ± 169 | 127 ± 118 |
| RCS J092508+3825.4 | 09 25 08.50 | +38 25 25.3 | 0.486 | 0.023 | 11.6 | 26.6 | 0.175 | 3.41 | 196 ± 176 | 220 ± 131 |
| RCS J093026+3835.7 | 09 30 26.10 | +38 35 43.7 | 0.486 | 0.023 | 10.2 | 29.4 | 0.122 | 3.33 | 354 ± 190 | 125 ± 119 |

TABLE 5—Continued

| Cluster | R.A. (J2000) | Decl. (J2000) | z | Δz | ΔBCG (arcsec) | Size (arcsec) | ϵ | σ_{peak} | B_{gcT} (Mpc ^{1.8}) | B_{gcR} (Mpc ^{1.8}) |
|-------------------------|--------------|---------------|-------|------------|--------------------------------|------------------|------------|------------------------|---|---|
| RCS J092658+3612.1..... | 09 26 58.50 | +36 12 09.7 | 0.489 | 0.022 | 7.5 | 28.3 | 0.175 | 3.41 | 606 ± 210 | 629 ± 173 |
| RCS J093010+3841.1..... | 09 30 10.40 | +38 41 09.1 | 0.491 | 0.028 | 19.7 | 50.1 | 0.526 | 3.37 | 507 ± 203 | 378 ± 148 |
| RCS J092235+3642.5..... | 09 22 35.00 | +36 42 34.8 | 0.498 | 0.023 | 61.4 | 75.0 | 0.284 | 3.81 | 498 ± 203 | 503 ± 161 |
| RCS J092813+3611.2..... | 09 28 13.10 | +36 11 13.2 | 0.498 | 0.025 | 11.1 | 52.9 | 0.194 | 5.02 | 1067 ± 244 | 882 ± 195 |
| RCS J092645+3817.7..... | 09 26 45.50 | +38 17 46.6 | 0.499 | 0.022 | 17.5 | 59.0 | 0.380 | 4.24 | 655 ± 215 | 471 ± 158 |
| RCS J092910+3633.4..... | 09 29 10.10 | +36 33 26.1 | 0.500 | 0.025 | 23.2 | 51.6 | 0.185 | 4.14 | 954 ± 243 | 776 ± 192 |
| RCS J093127+3745.9..... | 09 31 27.30 | +37 45 55.6 | 0.509 | 0.020 | 10.8 | 23.1 | 0.047 | 3.87 | 311 ± 190 | 234 ± 132 |
| RCS J092211+3722.1..... | 09 22 11.70 | +37 22 10.0 | 0.509 | 0.020 | 65.2 | 30.0 | 0.073 | 3.66 | 159 ± 177 | 329 ± 143 |
| RCS J092833+3745.0..... | 09 28 33.70 | +37 45 00.0 | 0.509 | 0.023 | 57.6 | 43.3 | 0.211 | 4.00 | 696 ± 220 | 390 ± 149 |
| RCS J092649+3648.5..... | 09 26 49.40 | +36 48 35.4 | 0.509 | 0.022 | 50.5 | 60.2 | 0.508 | 3.80 | 389 ± 197 | 484 ± 159 |
| RCS J093042+3728.4..... | 09 30 42.00 | +37 28 27.5 | 0.514 | 0.022 | 34.1 | 100.2 | 0.667 | 3.58 | 445 ± 202 | 411 ± 152 |
| RCS J092741+3839.5..... | 09 27 41.30 | +38 39 35.3 | 0.515 | 0.020 | 46.5 | 29.3 | 0.129 | 3.56 | 696 ± 221 | 315 ± 142 |
| RCS J092144+3729.5..... | 09 21 44.20 | +37 29 31.7 | 0.520 | 0.020 | 12.7 | 23.5 | 0.214 | 3.42 | 213 ± 185 | 161 ± 122 |
| RCS J092753+3838.8..... | 09 27 53.90 | +38 38 52.3 | 0.521 | 0.020 | 18.5 | 22.5 | 0.087 | 3.53 | 590 ± 215 | 443 ± 155 |
| RCS J092658+3637.6..... | 09 26 58.60 | +36 37 41.3 | 0.521 | 0.020 | 55.7 | 43.2 | 0.507 | 3.33 | 400 ± 200 | 380 ± 148 |
| RCS J093049+3725.9..... | 09 30 49.10 | +37 25 59.8 | 0.531 | 0.018 | 21.0 | 35.8 | 0.295 | 3.70 | 384 ± 201 | 193 ± 126 |
| RCS J092713+3842.7..... | 09 27 13.90 | +38 42 46.2 | 0.535 | 0.020 | 81.6 | 75.2 | 0.656 | 3.76 | 158 ± 183 | 290 ± 137 |
| RCS J092832+3620.5..... | 09 28 32.80 | +36 20 33.9 | 0.539 | 0.022 | 3.5 | 61.9 | 0.450 | 4.10 | 834 ± 235 | 712 ± 179 |
| RCS J093121+3736.8..... | 09 31 21.80 | +37 36 50.0 | 0.540 | 0.016 | 15.6 | 28.1 | 0.229 | 3.31 | 215 ± 189 | 195 ± 126 |
| RCS J092610+3601.9..... | 09 26 10.70 | +36 01 58.4 | 0.540 | 0.016 | 45.0 | 22.4 | 0.230 | 3.51 | 377 ± 202 | 318 ± 141 |
| RCS J092231+3612.4..... | 09 22 31.20 | +36 12 28.6 | 0.542 | 0.018 | 5.0 | 35.9 | 0.145 | 4.23 | 564 ± 219 | 535 ± 165 |
| RCS J092921+3755.9..... | 09 29 21.40 | +37 55 59.0 | 0.543 | 0.023 | 46.8 | 75.1 | 0.569 | 3.33 | 779 ± 232 | 386 ± 148 |
| RCS J092712+3741.7..... | 09 27 12.60 | +37 41 46.0 | 0.548 | 0.016 | 14.7 | 21.8 | 0.179 | 3.38 | 424 ± 207 | 418 ± 151 |
| RCS J092750+3616.2..... | 09 27 50.40 | +36 16 13.4 | 0.551 | 0.016 | 34.7 | 21.3 | 0.183 | 3.53 | 194 ± 190 | 197 ± 126 |
| RCS J092739+3627.1..... | 09 27 39.10 | +36 27 10.9 | 0.553 | 0.014 | 9.4 | 20.6 | 0.129 | 3.67 | 762 ± 233 | 262 ± 133 |
| RCS J092308+3813.5..... | 09 23 08.20 | +38 13 33.7 | 0.555 | 0.018 | 6.5 | 31.3 | 0.380 | 3.35 | 412 ± 208 | 293 ± 137 |
| RCS J092606+3758.7..... | 09 26 06.70 | +37 58 46.9 | 0.555 | 0.022 | 39.0 | 74.5 | 0.500 | 3.93 | 697 ± 228 | 578 ± 167 |
| RCS J092641+3630.2..... | 09 26 41.40 | +36 30 16.6 | 0.556 | 0.014 | 49.8 | 20.9 | 0.110 | 3.30 | 1076 ± 253 | 356 ± 144 |
| RCS J092604+3627.4..... | 09 26 04.90 | +36 27 24.4 | 0.559 | 0.014 | 39.0 | 41.8 | 0.287 | 3.63 | 440 ± 210 | 262 ± 133 |
| RCS J093057+3721.6..... | 09 30 57.00 | +37 21 37.0 | 0.561 | 0.014 | 6.5 | 31.8 | 0.131 | 4.06 | 248 ± 196 | 234 ± 130 |
| RCS J092905+3739.6..... | 09 29 05.50 | +37 39 36.1 | 0.564 | 0.014 | 10.0 | 72.2 | 0.607 | 3.60 | 131 ± 187 | 181 ± 123 |
| RCS J092606+3622.0..... | 09 26 06.40 | +36 22 05.9 | 0.565 | 0.014 | 29.1 | 25.8 | 0.215 | 3.60 | 399 ± 209 | 297 ± 137 |
| RCS J092445+3711.5..... | 09 24 45.10 | +37 11 34.8 | 0.565 | 0.014 | 4.7 | 38.1 | 0.424 | 3.49 | 367 ± 206 | 329 ± 140 |
| RCS J092334+3823.3..... | 09 23 34.60 | +38 23 23.5 | 0.566 | 0.014 | 32.0 | 27.9 | 0.198 | 3.62 | 206 ± 194 | 265 ± 133 |
| RCS J092451+3821.7..... | 09 24 51.30 | +38 21 44.9 | 0.572 | 0.014 | 14.5 | 36.1 | 0.302 | 4.13 | 568 ± 237 | 569 ± 176 |
| RCS J092136+3623.3..... | 09 21 36.80 | +36 23 18.7 | 0.573 | 0.014 | 35.5 | 31.1 | 0.272 | 3.49 | 242 ± 202 | 260 ± 135 |
| RCS J092434+3751.1..... | 09 24 34.00 | +37 51 09.4 | 0.575 | 0.016 | 14.6 | 67.9 | 0.333 | 4.90 | 1077 ± 257 | 648 ± 172 |
| RCS J092547+3717.8..... | 09 25 47.30 | +37 17 48.2 | 0.578 | 0.022 | 10.8 | 50.7 | 0.271 | 4.10 | 1073 ± 257 | 773 ± 184 |
| RCS J092940+3637.9..... | 09 29 40.00 | +36 37 56.4 | 0.583 | 0.015 | 24.3 | 23.6 | 0.107 | 3.37 | 232 ± 229 | 177 ± 138 |
| RCS J092136+3625.6..... | 09 21 36.60 | +36 25 41.7 | 0.588 | 0.015 | 11.1 | 27.3 | 0.106 | 3.94 | 619 ± 238 | 406 ± 154 |
| RCS J092902+3620.0..... | 09 29 02.20 | +36 20 03.8 | 0.590 | 0.014 | 3.8 | 48.2 | 0.283 | 3.89 | 599 ± 240 | 497 ± 166 |
| RCS J092459+3747.1..... | 09 24 59.60 | +37 47 10.8 | 0.600 | 0.015 | 25.0 | 32.6 | 0.161 | 3.36 | 503 ± 223 | 314 ± 137 |
| RCS J092457+3846.4..... | 09 24 57.80 | +38 46 29.1 | 0.602 | 0.015 | 16.7 | 30.1 | 0.438 | 3.32 | 235 ± 217 | 200 ± 131 |
| RCS J092945+3656.1..... | 09 29 45.50 | +36 56 11.6 | 0.613 | 0.014 | 49.0 | 43.4 | 0.157 | 4.18 | 984 ± 266 | 542 ± 167 |
| RCS J092938+3714.4..... | 09 29 38.40 | +37 14 27.3 | 0.617 | 0.016 | 12.3 | 33.6 | 0.342 | 3.59 | 6 ± 211 | 257 ± 146 |
| RCS J092224+3629.0..... | 09 22 24.50 | +36 29 01.8 | 0.618 | 0.016 | 7.0 | 32.9 | 0.321 | 3.43 | 258 ± 224 | 293 ± 144 |
| RCS J092359+3742.4..... | 09 23 59.60 | +37 42 29.6 | 0.618 | 0.016 | 4.8 | 37.2 | 0.429 | 3.32 | 343 ± 215 | 149 ± 116 |
| RCS J092645+3604.4..... | 09 26 45.20 | +36 04 25.4 | 0.618 | 0.014 | 2.7 | 37.1 | 0.162 | 4.42 | 803 ± 255 | 736 ± 185 |
| RCS J092358+3841.5..... | 09 23 58.70 | +38 41 34.8 | 0.620 | 0.015 | 12.4 | 30.9 | 0.117 | 4.32 | 635 ± 236 | 558 ± 162 |
| RCS J093001+3758.0..... | 09 30 01.10 | +37 58 00.7 | 0.621 | 0.016 | 5.2 | 20.2 | 0.119 | 3.50 | 509 ± 235 | 250 ± 133 |
| RCS J092402+3754.5..... | 09 24 02.10 | +37 54 34.6 | 0.621 | 0.016 | 64.1 | 29.6 | 0.134 | 3.36 | 648 ± 267 | 343 ± 158 |
| RCS J092622+3621.8..... | 09 26 22.90 | +36 21 49.6 | 0.624 | 0.014 | 25.5 | 43.1 | 0.167 | 4.42 | 1002 ± 260 | 911 ± 193 |
| RCS J092924+3827.3..... | 09 29 24.30 | +38 27 22.9 | 0.628 | 0.016 | 6.0 | 20.9 | 0.138 | 3.38 | −1 ± 223 | 126 ± 131 |
| RCS J093045+3838.8..... | 09 30 45.90 | +38 38 52.9 | 0.628 | 0.014 | 41.5 | 78.0 | 0.652 | 3.50 | 424 ± 232 | 229 ± 131 |
| RCS J092139+3620.8..... | 09 21 39.50 | +36 20 53.3 | 0.636 | 0.016 | 23.1 | 23.5 | 0.076 | 3.37 | 96 ± 219 | 87 ± 117 |
| RCS J093032+3846.0..... | 09 30 32.00 | +38 46 00.9 | 0.638 | 0.016 | 5.6 | 41.5 | 0.182 | 3.69 | 651 ± 253 | 550 ± 170 |
| RCS J092408+3836.9..... | 09 24 08.40 | +38 36 55.3 | 0.638 | 0.018 | 11.9 | 22.6 | 0.132 | 3.70 | 3 ± 192 | 190 ± 120 |
| RCS J093050+3845.1..... | 09 30 50.20 | +38 45 08.7 | 0.638 | 0.018 | 10.3 | 26.5 | 0.241 | 3.67 | 261 ± 223 | 278 ± 138 |
| RCS J092654+3606.6..... | 09 26 54.30 | +36 06 36.8 | 0.642 | 0.016 | 8.0 | 26.7 | 0.153 | 3.66 | 316 ± 217 | 189 ± 120 |
| RCS J092515+3606.3..... | 09 25 15.00 | +36 06 22.0 | 0.655 | 0.018 | 24.0 | 37.0 | 0.328 | 3.53 | 505 ± 244 | 380 ± 150 |
| RCS J092649+3638.5..... | 09 26 49.90 | +36 38 30.6 | 0.657 | 0.021 | 14.0 | 27.3 | 0.178 | 3.45 | 208 ± 211 | 58 ± 100 |
| RCS J092843+3734.7..... | 09 28 43.10 | +37 34 42.4 | 0.659 | 0.021 | 17.0 | 26.1 | 0.051 | 3.51 | −26 ± 209 | 36 ± 103 |
| RCS J092333+3706.4..... | 09 23 33.30 | +37 06 26.2 | 0.660 | 0.018 | 10.2 | 21.8 | 0.150 | 3.43 | 261 ± 219 | 76 ± 104 |
| RCS J092733+3609.0..... | 09 27 33.40 | +36 09 00.2 | 0.660 | 0.021 | 2.0 | 22.3 | 0.140 | 3.49 | 498 ± 254 | 200 ± 131 |
| RCS J092135+3720.0..... | 09 21 35.10 | +37 20 02.5 | 0.661 | 0.018 | 15.6 | 44.5 | 0.180 | 3.56 | 468 ± 252 | 562 ± 177 |

TABLE 5—*Continued*

| Cluster | R.A. (J2000) | Decl. (J2000) | z | Δz | Δ BCG (arcsec) | Size (arcsec) | ϵ | σ_{peak} | B_{gcT} (Mpc ^{1.8}) | B_{gcR} (Mpc ^{1.8}) |
|--------------------------|--------------|---------------|-------|------------|--------------------------|------------------|------------|------------------------|---|---|
| RCS J092342+3843.5 | 09 23 42.20 | +38 43 33.0 | 0.661 | 0.021 | 15.1 | 20.1 | 0.122 | 3.35 | 792 ± 252 | 225 ± 123 |
| RCS J092710+3755.4 | 09 27 10.00 | +37 55 28.7 | 0.663 | 0.021 | 10.5 | 22.0 | 0.160 | 3.33 | 392 ± 227 | 230 ± 125 |
| RCS J093029+3830.0 | 09 30 29.40 | +38 30 03.8 | 0.663 | 0.018 | 25.3 | 32.3 | 0.033 | 4.07 | 697 ± 289 | 663 ± 201 |
| RCS J092546+3621.8 | 09 25 46.70 | +36 21 48.1 | 0.664 | 0.016 | 55.2 | 51.9 | 0.497 | 3.89 | 866 ± 269 | 445 ± 156 |
| RCS J092425+3702.4 | 09 24 25.90 | +37 02 24.1 | 0.668 | 0.021 | 4.7 | 21.2 | 0.141 | 3.40 | 161 ± 211 | 167 ± 116 |
| RCS J092849+3805.8 | 09 28 49.80 | +38 05 53.9 | 0.679 | 0.021 | 6.1 | 22.6 | 0.231 | 3.32 | 283 ± 237 | 259 ± 137 |
| RCS J092452+3656.2 | 09 24 52.80 | +36 56 16.7 | 0.682 | 0.021 | 25.8 | 20.8 | 0.100 | 3.34 | 265 ± 231 | 71 ± 105 |
| RCS J092304+3804.9 | 09 23 04.10 | +38 04 54.3 | 0.688 | 0.021 | 11.6 | 22.5 | 0.040 | 3.66 | 692 ± 296 | 412 ± 171 |
| RCS J092912+3639.2 | 09 29 12.30 | +36 39 13.7 | 0.692 | 0.021 | 15.8 | 39.5 | 0.283 | 3.78 | 1082 ± 377 | 595 ± 223 |
| RCS J092554+3652.9 | 09 25 54.10 | +36 52 58.1 | 0.694 | 0.021 | 23.9 | 37.0 | 0.280 | 4.16 | 736 ± 266 | 497 ± 161 |
| RCS J092813+3846.6 | 09 28 13.00 | +38 46 40.6 | 0.696 | 0.021 | 12.7 | 17.1 | 0.017 | 3.36 | 344 ± 296 | 252 ± 162 |
| RCS J092501+3637.5 | 09 25 01.90 | +36 37 31.2 | 0.701 | 0.021 | 6.5 | 37.3 | 0.501 | 3.30 | 436 ± 260 | 182 ± 128 |
| RCS J092754+3654.9 | 09 27 54.90 | +36 54 54.5 | 0.702 | 0.018 | 48.1 | 46.4 | 0.302 | 4.27 | 1205 ± 283 | 806 ± 182 |
| RCS J092935+3633.2 | 09 29 35.60 | +36 33 15.6 | 0.703 | 0.018 | 47.4 | 34.0 | 0.291 | 3.54 | 936 ± 374 | 496 ± 212 |
| RCS J092136+3630.6 | 09 21 36.30 | +36 30 39.7 | 0.705 | 0.021 | 7.2 | 29.5 | 0.216 | 3.88 | 553 ± 310 | 177 ± 145 |
| RCS J092716+3725.6 | 09 27 16.00 | +37 25 36.1 | 0.707 | 0.021 | 64.2 | 63.8 | 0.336 | 3.70 | 1020 ± 291 | 558 ± 169 |
| RCS J092928+3627.6 | 09 29 28.70 | +36 27 39.0 | 0.707 | 0.021 | 11.6 | 23.5 | 0.061 | 3.83 | 314 ± 284 | 275 ± 159 |
| RCS J092343+3656.4 | 09 23 43.60 | +36 56 26.7 | 0.712 | 0.021 | 22.7 | 27.9 | 0.126 | 3.82 | 107 ± 252 | 280 ± 151 |
| RCS J092528+3716.5 | 09 25 28.90 | +37 16 34.0 | 0.714 | 0.021 | 5.0 | 30.1 | 0.242 | 3.67 | 372 ± 247 | 405 ± 151 |
| RCS J092356+3726.3 | 09 23 56.40 | +37 26 18.6 | 0.717 | 0.021 | 8.7 | 45.8 | 0.360 | 3.60 | 37 ± 216 | 190 ± 119 |
| RCS J093101+3740.3 | 09 31 01.60 | +37 40 22.5 | 0.718 | 0.020 | 12.6 | 20.2 | 0.038 | 3.61 | 381 ± 239 | 191 ± 118 |
| RCS J092214+3815.6 | 09 22 14.10 | +38 15 38.3 | 0.719 | 0.020 | 9.6 | 24.7 | 0.300 | 3.39 | −35 ± 263 | 133 ± 137 |
| RCS J092324+3717.6 | 09 23 24.30 | +37 17 39.6 | 0.723 | 0.021 | 72.0 | 58.3 | 0.610 | 3.58 | 583 ± 289 | 310 ± 152 |
| RCS J093009+3633.7 | 09 30 09.90 | +36 33 42.9 | 0.724 | 0.020 | 8.4 | 28.8 | 0.299 | 3.38 | −199 ± 302 | 7 ± 122 |
| RCS J093016+3835.0 | 09 30 16.00 | +38 35 03.0 | 0.728 | 0.020 | 9.1 | 52.2 | 0.496 | 3.49 | 398 ± 286 | 156 ± 132 |
| RCS J092743+3821.9 | 09 27 43.00 | +38 21 59.6 | 0.735 | 0.018 | 1.8 | 19.0 | 0.086 | 3.30 | 218 ± 309 | 236 ± 164 |
| RCS J092737+3637.8 | 09 27 37.50 | +36 37 51.5 | 0.735 | 0.021 | 23.7 | 23.6 | 0.111 | 3.50 | 435 ± 271 | 449 ± 165 |
| RCS J092107+3618.5 | 09 21 07.30 | +36 18 31.7 | 0.735 | 0.020 | 5.1 | 26.5 | 0.182 | 3.55 | 607 ± 325 | 254 ± 158 |
| RCS J092910+3741.4 | 09 29 10.30 | +37 41 24.3 | 0.739 | 0.018 | 27.3 | 37.5 | 0.342 | 3.36 | 316 ± 274 | 368 ± 161 |
| RCS J092742+3654.3 | 09 27 42.80 | +36 54 22.2 | 0.741 | 0.020 | 52.8 | 44.5 | 0.402 | 3.49 | 320 ± 235 | 281 ± 125 |
| RCS J092753+3755.6 | 09 27 53.20 | +37 55 36.0 | 0.742 | 0.018 | 9.6 | 29.8 | 0.265 | 3.57 | 615 ± 297 | 544 ± 183 |
| RCS J092958+3844.1 | 09 29 58.40 | +38 44 06.0 | 0.743 | 0.021 | 22.6 | 126.5 | 0.699 | 4.26 | 909 ± 334 | 663 ± 206 |
| RCS J092722+3804.3 | 09 27 22.40 | +38 04 21.6 | 0.744 | 0.018 | 16.0 | 54.7 | 0.586 | 3.41 | 210 ± 246 | 180 ± 122 |
| RCS J092217+3750.1 | 09 22 17.50 | +37 50 08.3 | 0.747 | 0.021 | 118.1 | 55.7 | 0.515 | 3.36 | 678 ± 304 | 646 ± 196 |
| RCS J093124+3723.2 | 09 31 24.10 | +37 23 12.8 | 0.754 | 0.017 | 33.9 | 43.4 | 0.418 | 3.30 | 397 ± 290 | 302 ± 154 |
| RCS J092349+3709.9 | 09 23 49.00 | +37 09 58.1 | 0.756 | 0.017 | 7.0 | 20.9 | 0.169 | 3.31 | −315 ± 239 | 9 ± 93 |
| RCS J092425+3714.3 | 09 24 25.30 | +37 14 20.0 | 0.767 | 0.021 | 19.4 | 30.5 | 0.245 | 3.44 | 500 ± 289 | 447 ± 167 |
| RCS J092138+3617.2 | 09 21 38.40 | +36 17 17.1 | 0.773 | 0.017 | 9.4 | 23.8 | 0.254 | 3.42 | −5 ± 288 | 55 ± 119 |
| RCS J092909+3823.6 | 09 29 09.40 | +38 23 36.7 | 0.774 | 0.017 | 24.3 | 28.2 | 0.365 | 3.31 | 643 ± 391 | 343 ± 196 |
| RCS J092639+3609.4 | 09 26 39.10 | +36 09 28.4 | 0.776 | 0.017 | 9.1 | 18.4 | 0.048 | 3.41 | −251 ± 270 | 87 ± 119 |
| RCS J092455+3635.3 | 09 24 55.30 | +36 35 23.4 | 0.780 | 0.017 | 27.9 | 21.4 | 0.078 | 3.44 | 430 ± 302 | 174 ± 132 |
| RCS J092247+3613.9 | 09 22 47.90 | +36 13 55.6 | 0.781 | 0.017 | 26.7 | 45.9 | 0.444 | 3.75 | 869 ± 377 | 306 ± 174 |
| RCS J093127+3742.7 | 09 31 27.10 | +37 42 43.1 | 0.782 | 0.017 | 13.9 | 24.1 | 0.172 | 3.80 | 404 ± 266 | 94 ± 103 |
| RCS J092144+3608.1 | 09 21 44.10 | +36 08 11.3 | 0.784 | 0.020 | 8.9 | 53.6 | 0.028 | 4.27 | 883 ± 374 | 828 ± 245 |
| RCS J092247+3744.7 | 09 22 47.50 | +37 44 42.2 | 0.787 | 0.017 | 10.2 | 21.5 | 0.179 | 3.36 | 291 ± 298 | 222 ± 143 |
| RCS J093032+3758.6 | 09 30 32.60 | +37 58 37.2 | 0.790 | 0.018 | 12.2 | 23.1 | 0.154 | 3.48 | 174 ± 283 | 225 ± 141 |
| RCS J092641+3612.7 | 09 26 41.00 | +36 12 46.3 | 0.791 | 0.017 | 20.5 | 45.8 | 0.425 | 3.66 | 1056 ± 366 | 413 ± 177 |
| RCS J092947+3818.7 | 09 29 47.50 | +38 18 45.5 | 0.791 | 0.017 | 4.5 | 22.0 | 0.011 | 3.84 | 136 ± 250 | 384 ± 147 |
| RCS J092138+3716.7 | 09 21 38.20 | +37 16 44.1 | 0.796 | 0.018 | 16.0 | 20.6 | 0.140 | 3.33 | −133 ± 287 | 107 ± 126 |
| RCS J092343+3820.1 | 09 23 43.30 | +38 20 07.9 | 0.800 | 0.018 | 17.4 | 29.5 | 0.202 | 3.52 | 274 ± 295 | 282 ± 150 |
| RCS J092824+3817.3 | 09 28 24.40 | +38 17 23.9 | 0.804 | 0.017 | 5.0 | 25.8 | 0.234 | 3.48 | 847 ± 356 | 583 ± 202 |
| RCS J092151+3624.5 | 09 21 51.70 | +36 24 30.9 | 0.813 | 0.018 | 5.7 | 25.6 | 0.176 | 3.77 | 653 ± 379 | 465 ± 204 |
| RCS J093103+3726.7 | 09 31 03.10 | +37 26 43.6 | 0.815 | 0.019 | 5.9 | 18.4 | 0.049 | 3.37 | 235 ± 315 | 224 ± 150 |
| RCS J093107+3816.2 | 09 31 07.60 | +38 16 13.2 | 0.817 | 0.018 | 13.2 | 21.1 | 0.096 | 3.55 | 296 ± 272 | 289 ± 136 |
| RCS J092958+3610.5 | 09 29 58.50 | +36 10 33.2 | 0.821 | 0.019 | 14.6 | 20.9 | 0.204 | 3.34 | 97 ± 353 | 318 ± 190 |
| RCS J092340+3807.1 | 09 23 40.40 | +38 07 10.2 | 0.826 | 0.019 | 3.7 | 26.2 | 0.140 | 3.90 | 950 ± 334 | 553 ± 179 |
| RCS J092220+3627.7 | 09 22 20.90 | +36 27 47.6 | 0.833 | 0.018 | 6.6 | 32.3 | 0.245 | 3.49 | 344 ± 363 | 287 ± 176 |
| RCS J093118+3612.0 | 09 31 18.80 | +36 12 00.7 | 0.834 | 0.019 | 46.1 | 36.0 | 0.227 | 4.05 | 502 ± 424 | 610 ± 254 |
| RCS J092537+3612.1 | 09 25 37.60 | +36 12 11.0 | 0.841 | 0.024 | 13.8 | 25.4 | 0.200 | 3.34 | 492 ± 372 | 262 ± 168 |
| RCS J093025+3717.9 | 09 30 25.90 | +37 17 58.2 | 0.843 | 0.019 | 9.1 | 43.9 | 0.278 | 3.55 | 577 ± 343 | 269 ± 153 |
| RCS J093030+3727.5 | 09 30 30.40 | +37 27 32.9 | 0.844 | 0.018 | 41.8 | 26.1 | 0.284 | 3.38 | 625 ± 347 | 375 ± 171 |
| RCS J093037+3816.6 | 09 30 37.40 | +38 16 40.4 | 0.844 | 0.019 | 24.8 | 29.7 | 0.174 | 3.73 | 259 ± 275 | 376 ± 147 |
| RCS J092220+3749.9 | 09 22 20.40 | +37 49 58.5 | 0.845 | 0.024 | 13.6 | 21.1 | 0.114 | 3.46 | 1324 ± 413 | 355 ± 175 |
| RCS J092740+3623.7 | 09 27 40.80 | +36 23 46.8 | 0.847 | 0.024 | 8.9 | 20.3 | 0.092 | 3.61 | 409 ± 293 | 191 ± 123 |
| RCS J092530+3832.2 | 09 25 30.70 | +38 32 12.1 | 0.848 | 0.024 | 11.8 | 33.9 | 0.346 | 3.38 | −407 ± 375 | 127 ± 158 |

TABLE 5—*Continued*

| Cluster | R.A. (J2000) | Decl. (J2000) | z | Δz | ΔBCG (arcsec) | Size (arcsec) | ϵ | σ_{peak} | $B_{\text{gc}T}$ (Mpc ^{1.8}) | $B_{\text{gc}R}$ (Mpc ^{1.8}) |
|-------------------------|--------------|---------------|-------|------------|--------------------------------|------------------|------------|------------------------|---|---|
| RCS J092713+3808.6..... | 09 27 13.20 | +38 08 38.0 | 0.852 | 0.017 | 1.9 | 28.7 | 0.372 | 3.30 | -25 ± 247 | 297 ± 129 |
| RCS J092135+3627.0..... | 09 21 35.40 | +36 27 04.2 | 0.856 | 0.017 | 188.9 | 246.6 | 0.759 | 4.87 | 606 ± 412 | 466 ± 216 |
| RCS J092858+3646.5..... | 09 28 58.30 | +36 46 32.2 | 0.857 | 0.019 | 13.5 | 24.5 | 0.103 | 3.43 | 413 ± 448 | 242 ± 195 |
| RCS J092251+3602.4..... | 09 22 51.60 | +36 02 27.6 | 0.864 | 0.017 | 9.7 | 45.3 | 0.385 | 3.90 | 927 ± 458 | 737 ± 266 |
| RCS J092416+3726.7..... | 09 24 16.70 | +37 26 45.0 | 0.867 | 0.017 | 32.6 | 40.0 | 0.355 | 3.45 | 1204 ± 366 | 269 ± 142 |
| RCS J092230+3837.5..... | 09 22 30.40 | +38 37 30.0 | 0.874 | 0.024 | 44.2 | 41.5 | 0.551 | 3.47 | 424 ± 385 | 433 ± 202 |
| RCS J092954+3724.6..... | 09 29 54.20 | +37 24 36.6 | 0.879 | 0.024 | 8.3 | 23.3 | 0.274 | 3.32 | 64 ± 350 | 360 ± 187 |
| RCS J093119+3723.4..... | 09 31 19.80 | +37 23 28.1 | 0.879 | 0.019 | 13.1 | 35.0 | 0.407 | 3.44 | 105 ± 349 | 607 ± 224 |
| RCS J092904+3831.3..... | 09 29 04.40 | +38 31 20.4 | 0.880 | 0.018 | 66.1 | 49.8 | 0.292 | 3.57 | 477 ± 489 | 470 ± 253 |
| RCS J092621+3621.8..... | 09 26 21.90 | +36 21 48.3 | 0.887 | 0.024 | 20.7 | 26.5 | 0.132 | 3.61 | 2088 ± 427 | 377 ± 160 |
| RCS J092440+3757.2..... | 09 24 40.50 | +37 57 12.4 | 0.888 | 0.020 | 10.2 | 53.0 | 0.228 | 4.07 | 1126 ± 409 | 591 ± 209 |
| RCS J092506+3727.0..... | 09 25 06.90 | +37 27 01.9 | 0.892 | 0.019 | 52.9 | 27.0 | 0.257 | 3.53 | 704 ± 393 | 205 ± 152 |
| RCS J092944+3626.8..... | 09 29 44.90 | +36 26 51.8 | 0.893 | 0.028 | 12.7 | 21.5 | 0.185 | 3.42 | 665 ± 385 | 320 ± 170 |
| RCS J092313+3724.8..... | 09 23 13.10 | +37 24 52.9 | 0.894 | 0.028 | 16.3 | 17.6 | 0.040 | 3.37 | -102 ± 349 | 163 ± 148 |
| RCS J093037+3636.6..... | 09 30 37.10 | +36 36 41.6 | 0.899 | 0.024 | 44.5 | 30.7 | 0.430 | 3.58 | 672 ± 545 | 527 ± 277 |
| RCS J092314+3721.3..... | 09 23 14.20 | +37 21 23.6 | 0.900 | 0.024 | 16.0 | 27.6 | 0.205 | 3.69 | 1269 ± 497 | 748 ± 268 |
| RCS J092545+3611.7..... | 09 25 45.90 | +36 11 47.1 | 0.912 | 0.031 | 13.0 | 28.2 | 0.236 | 3.31 | 327 ± 427 | 369 ± 207 |
| RCS J093122+3624.3..... | 09 31 22.70 | +36 24 19.9 | 0.913 | 0.018 | 63.8 | 50.5 | 0.295 | 4.50 | 2227 ± 516 | 1448 ± 322 |
| RCS J093020+3605.2..... | 09 30 20.30 | +36 05 16.0 | 0.914 | 0.024 | 65.3 | 51.7 | 0.614 | 3.39 | 546 ± 477 | 157 ± 172 |
| RCS J092101+3818.5..... | 09 21 01.90 | +38 18 33.5 | 0.949 | 0.031 | 22.0 | 68.0 | 0.431 | 4.50 | 82 ± 492 | 606 ± 284 |
| RCS J093036+3745.6..... | 09 30 36.80 | +37 45 38.3 | 0.951 | 0.031 | 16.0 | 22.4 | 0.138 | 3.32 | 218 ± 344 | 284 ± 153 |
| RCS J092732+3637.0..... | 09 27 32.70 | +36 37 00.6 | 0.956 | 0.024 | 19.7 | 58.8 | 0.683 | 3.51 | 638 ± 443 | 478 ± 215 |
| RCS J092611+3636.0..... | 09 26 11.80 | +36 36 05.3 | 0.959 | 0.031 | 10.5 | 18.9 | 0.121 | 3.40 | 57 ± 394 | 226 ± 168 |
| RCS J092138+3733.6..... | 09 21 38.50 | +37 33 40.3 | 0.960 | 0.039 | 5.1 | 21.2 | 0.190 | 3.37 | 96 ± 429 | 60 ± 137 |
| RCS J092435+3818.0..... | 09 24 35.10 | +38 18 00.2 | 0.977 | 0.031 | 23.2 | 19.0 | 0.080 | 3.31 | -115 ± 381 | 176 ± 151 |
| RCS J092620+3834.6..... | 09 26 20.90 | +38 34 36.8 | 0.997 | 0.028 | 12.3 | 18.7 | 0.154 | 3.31 | 222 ± 489 | 262 ± 199 |
| RCS J092831+3612.2..... | 09 28 31.70 | +36 12 12.6 | 1.000 | 0.039 | 129.8 | 60.7 | 0.634 | 3.32 | 744 ± 780 | 238 ± 268 |
| RCS J093006+3643.1..... | 09 30 06.80 | +36 43 06.7 | 1.017 | 0.031 | 16.6 | 38.0 | 0.455 | 3.39 | 547 ± 581 | 474 ± 264 |
| RCS J093047+3753.5..... | 09 30 47.90 | +37 53 34.9 | 1.034 | 0.031 | 17.7 | 19.6 | 0.067 | 3.47 | 860 ± 577 | 470 ± 250 |
| RCS J092212+3624.7..... | 09 22 12.40 | +36 24 45.4 | 1.035 | 0.039 | 3.0 | 86.4 | 0.707 | 3.63 | 1522 ± 757 | 399 ± 278 |
| RCS J092124+3801.2..... | 09 21 24.80 | +38 01 13.6 | 1.066 | 0.039 | 13.7 | 24.9 | 0.183 | 3.62 | 98 ± 827 | 786 ± 435 |
| RCS J092301+3641.2..... | 09 23 01.40 | +36 41 13.3 | 1.088 | 0.028 | 142.0 | 137.9 | 0.752 | 3.49 | 1686 ± 970 | 736 ± 413 |
| RCS J092119+3611.5..... | 09 21 19.70 | +36 11 34.7 | 1.100 | 0.039 | 8.7 | 29.0 | 0.266 | 3.49 | 330 ± 977 | 698 ± 453 |
| RCS J093015+3738.7..... | 09 30 15.30 | +37 38 45.9 | 1.105 | 0.059 | 2.5 | 27.4 | 0.403 | 3.31 | 318 ± 544 | 506 ± 251 |
| RCS J093110+3618.9..... | 09 31 10.40 | +36 18 55.6 | 1.113 | 0.031 | 13.7 | 19.5 | 0.128 | 3.35 | 886 ± 720 | 744 ± 342 |
| RCS J092102+3752.2..... | 09 21 02.70 | +37 52 13.1 | 1.113 | 0.059 | 8.8 | 17.4 | 0.069 | 3.35 | 67 ± 1026 | 378 ± 389 |
| RCS J092736+3621.9..... | 09 27 36.20 | +36 21 55.9 | 1.144 | 0.039 | 29.7 | 38.7 | 0.172 | 3.93 | 1495 ± 665 | 741 ± 294 |
| RCS J092715+3805.5..... | 09 27 15.70 | +38 05 32.9 | 1.186 | 0.031 | 9.4 | 97.2 | 0.734 | 3.78 | 1146 ± 851 | 646 ± 345 |
| RCS J092219+3800.8..... | 09 22 19.30 | +38 00 48.0 | 1.206 | 0.039 | 51.8 | 43.0 | 0.392 | 3.38 | 1823 ± 1699 | 1504 ± 788 |
| RCS J092718+3733.2..... | 09 27 18.30 | +37 33 16.3 | 1.207 | 0.059 | 28.7 | 25.0 | 0.197 | 3.89 | 2235 ± 1055 | 1344 ± 507 |
| RCS J092511+3634.5..... | 09 25 11.50 | +36 34 34.3 | 1.230 | 0.059 | 52.6 | 36.6 | 0.519 | 3.42 | 2458 ± 1159 | 941 ± 461 |
| RCS J092339+3813.1..... | 09 23 39.00 | +38 13 10.9 | 1.232 | 0.039 | 10.8 | 22.0 | 0.169 | 3.40 | 518 ± 910 | 815 ± 405 |
| RCS J092741+3649.6..... | 09 27 41.80 | +36 49 36.3 | 1.232 | 0.039 | 27.0 | 48.7 | 0.431 | 3.37 | 1058 ± 765 | 452 ± 269 |
| RCS J092412+3840.4..... | 09 24 12.60 | +38 40 29.3 | 1.245 | 0.059 | 35.1 | 33.2 | 0.190 | 3.76 | 1184 ± 1051 | 1261 ± 513 |
| RCS J092740+3734.1..... | 09 27 40.30 | +37 34 10.3 | 1.281 | 0.059 | 17.6 | 47.4 | 0.421 | 3.31 | 306 ± 1291 | 793 ± 520 |
| RCS J093029+3714.7..... | 09 30 29.30 | +37 14 42.9 | 1.283 | 0.133 | 15.3 | 23.3 | 0.217 | 3.46 | 881 ± 1500 | 644 ± 527 |
| RCS J092552+3809.4..... | 09 25 52.50 | +38 09 28.9 | 1.286 | 0.133 | 5.1 | 19.6 | 0.130 | 3.30 | 226 ± 1276 | 296 ± 383 |

NOTE.—Units of right ascension are hours, minutes, and seconds, and units of declination are degrees, arcminutes, and arcseconds. Table 5 is also available in machine-readable form in the electronic edition of the *Astrophysical Journal Supplement*.

typically used to separate blue and red cluster galaxies (e.g., Butcher & Oemler 1984). Each galaxy considered is assigned a score equal to its z' magnitude, minus the value of σ_{ij} at that line of sight at the cluster redshift. The lowest ranking object is picked as the nominal brightest cluster galaxy. The use of weighting by the σ_{ij} -values, in addition to simply considering the magnitudes, guards against unassociated bright objects on the periphery of the cluster being selected as the center. Large values of this offset between the position of this galaxy and the cluster center may indicate an incorrect central galaxy, or a cluster with a filamentary shape or ill-defined center (such as a double cluster).

In addition to positions for each cluster, Tables 5 and 6 give estimates of the apparent projected size and shape of each cluster.

These values are derived by considering all voxels corresponding to the cluster in the σ_{ij} datacube, projected along the redshift axis. A size and ellipticity is computed by considering weighted moments of this projected distribution, with each input voxel assigned a weight equal to its value in excess of 2.5σ . Tables 5 and 6 give the resulting ellipticity, and the size of the semimajor axis in arcseconds. Clusters with unusually large sizes or ellipticities are likely multiple associated structures. As a final diagnostic, Tables 5 and 6 also provide an estimate of the redshift “range” for each cluster, where the range is found from the minimum and maximum redshifts ascribed to the set of voxels that make up the cluster peak in the σ_{ij} datacube. As in the projected size and shape, egregiously large values of this range in

TABLE 6
CLUSTERS IN THE PATCH RCS 1327+29

| Cluster | R.A. (J2000) | Decl. (J2000) | z | Δz | ΔBCG (arcsec) | Size (arcsec) | ϵ | σ_{peak} | $B_{\text{gc}T}$ (Mpc ^{1.8}) | $B_{\text{gc}R}$ (Mpc ^{1.8}) |
|-------------------------|--------------|---------------|-------|------------|--------------------------------|------------------|------------|------------------------|---|---|
| RCS J132757+2900.5..... | 13 27 57.10 | +29 00 32.5 | 0.201 | 0.037 | 82.9 | 47.8 | 0.113 | 3.32 | 375 ± 174 | 313 ± 154 |
| RCS J132524+2935.9..... | 13 25 24.60 | +29 35 57.9 | 0.212 | 0.037 | 111.1 | 106.7 | 0.550 | 3.32 | 401 ± 179 | 348 ± 160 |
| RCS J132606+2926.5..... | 13 26 06.70 | +29 26 31.2 | 0.229 | 0.037 | 26.8 | 52.6 | 0.137 | 3.96 | 422 ± 185 | 303 ± 155 |
| RCS J132523+2839.0..... | 13 25 23.80 | +28 39 02.1 | 0.248 | 0.037 | 138.4 | 110.5 | 0.610 | 4.11 | 567 ± 203 | 420 ± 170 |
| RCS J132447+3052.2..... | 13 24 47.20 | +30 52 14.9 | 0.265 | 0.037 | 36.1 | 38.5 | 0.391 | 3.37 | 443 ± 194 | 407 ± 169 |
| RCS J132706+2846.8..... | 13 27 06.10 | +28 46 49.7 | 0.275 | 0.038 | 64.8 | 37.3 | 0.036 | 3.73 | 498 ± 201 | 339 ± 161 |
| RCS J132802+3046.1..... | 13 28 02.40 | +30 46 10.5 | 0.288 | 0.037 | 95.1 | 64.6 | 0.161 | 3.69 | 645 ± 217 | 579 ± 188 |
| RCS J132630+2837.8..... | 13 26 30.80 | +28 37 51.5 | 0.289 | 0.038 | 4.6 | 76.7 | 0.654 | 3.48 | 525 ± 206 | 420 ± 170 |
| RCS J132643+2852.8..... | 13 26 43.40 | +28 52 52.4 | 0.298 | 0.037 | 19.7 | 104.1 | 0.472 | 4.17 | 620 ± 217 | 549 ± 185 |
| RCS J132655+2927.3..... | 13 26 55.90 | +29 27 18.3 | 0.313 | 0.038 | 12.2 | 29.7 | 0.258 | 3.50 | 379 ± 196 | 338 ± 161 |
| RCS J132739+2855.8..... | 13 27 39.70 | +28 55 51.7 | 0.314 | 0.038 | 15.1 | 25.2 | 0.104 | 3.30 | 298 ± 187 | 298 ± 156 |
| RCS J133010+3043.4..... | 13 30 10.70 | +30 43 28.3 | 0.316 | 0.037 | 1.8 | 103.7 | 0.212 | 6.19 | 1779 ± 307 | 1379 ± 260 |
| RCS J132348+3003.4..... | 13 23 48.10 | +30 03 27.4 | 0.319 | 0.038 | 4.2 | 41.6 | 0.267 | 3.72 | 611 ± 219 | 497 ± 180 |
| RCS J132901+2907.5..... | 13 29 01.20 | +29 07 31.7 | 0.321 | 0.037 | 17.9 | 62.8 | 0.456 | 3.54 | 248 ± 184 | 376 ± 166 |
| RCS J132901+2927.3..... | 13 29 01.40 | +29 27 19.2 | 0.328 | 0.038 | 152.0 | 147.4 | 0.689 | 4.05 | 481 ± 209 | 376 ± 166 |
| RCS J133010+3001.3..... | 13 30 10.80 | +30 01 23.0 | 0.341 | 0.035 | 17.9 | 43.9 | 0.350 | 3.71 | 147 ± 176 | 179 ± 139 |
| RCS J133152+2959.3..... | 13 31 52.10 | +29 59 21.5 | 0.342 | 0.035 | 18.2 | 47.9 | 0.465 | 3.71 | 668 ± 228 | 419 ± 170 |
| RCS J132557+3007.1..... | 13 25 57.70 | +30 07 06.8 | 0.342 | 0.035 | 37.7 | 74.0 | 0.668 | 3.32 | 307 ± 194 | 299 ± 156 |
| RCS J133016+3029.9..... | 13 30 16.40 | +30 29 54.8 | 0.343 | 0.035 | 4.7 | 35.7 | 0.177 | 3.45 | 105 ± 172 | 57 ± 121 |
| RCS J132622+2847.1..... | 13 26 22.10 | +28 47 10.4 | 0.345 | 0.035 | 48.5 | 127.0 | 0.531 | 3.41 | 265 ± 190 | 378 ± 166 |
| RCS J132633+2920.7..... | 13 26 33.60 | +29 20 47.9 | 0.345 | 0.035 | 9.3 | 67.2 | 0.380 | 3.37 | 345 ± 198 | 298 ± 156 |
| RCS J132532+2938.3..... | 13 25 32.90 | +29 38 20.8 | 0.346 | 0.038 | 9.7 | 53.6 | 0.097 | 5.91 | 1025 ± 258 | 819 ± 212 |
| RCS J132652+3003.3..... | 13 26 52.10 | +30 03 21.2 | 0.347 | 0.035 | 32.4 | 40.8 | 0.389 | 3.75 | 262 ± 190 | 296 ± 156 |
| RCS J133031+3012.5..... | 13 30 31.10 | +30 12 33.3 | 0.349 | 0.035 | 102.5 | 70.0 | 0.269 | 3.56 | 740 ± 235 | 660 ± 197 |
| RCS J132655+3021.1..... | 13 26 55.50 | +30 21 11.6 | 0.362 | 0.038 | 269.4 | 133.2 | 0.664 | 6.19 | 1530 ± 296 | 1380 ± 260 |
| RCS J132626+2958.1..... | 13 26 26.50 | +29 58 10.2 | 0.362 | 0.035 | 52.7 | 59.1 | 0.226 | 3.32 | 407 ± 207 | 377 ± 166 |
| RCS J132624+2932.9..... | 13 26 24.10 | +29 32 55.7 | 0.364 | 0.037 | 28.6 | 69.3 | 0.468 | 3.31 | 566 ± 222 | 617 ± 193 |
| RCS J132726+3052.0..... | 13 27 26.20 | +30 52 01.1 | 0.368 | 0.035 | 17.8 | 26.6 | 0.282 | 3.50 | 621 ± 228 | 380 ± 166 |
| RCS J132642+2839.9..... | 13 26 42.30 | +28 39 56.4 | 0.373 | 0.032 | 32.3 | 39.8 | 0.299 | 3.39 | 906 ± 252 | 601 ± 191 |
| RCS J132956+3047.1..... | 13 29 56.10 | +30 47 08.9 | 0.375 | 0.032 | 38.5 | 46.4 | 0.207 | 4.27 | 712 ± 237 | 458 ± 175 |
| RCS J133216+3033.9..... | 13 32 16.60 | +30 33 58.8 | 0.376 | 0.032 | 5.2 | 47.7 | 0.372 | 3.48 | 512 ± 219 | 578 ± 188 |
| RCS J132834+3030.3..... | 13 28 34.80 | +30 30 23.2 | 0.376 | 0.032 | 4.6 | 32.3 | 0.295 | 3.54 | 271 ± 196 | 177 ± 139 |
| RCS J132423+3010.5..... | 13 24 23.70 | +30 10 31.2 | 0.398 | 0.031 | 1.8 | 27.7 | 0.118 | 3.43 | 286 ± 202 | 219 ± 145 |
| RCS J132739+3006.0..... | 13 27 39.70 | +30 06 04.9 | 0.400 | 0.031 | 18.6 | 32.2 | 0.224 | 3.40 | 646 ± 235 | 339 ± 161 |
| RCS J132350+2934.7..... | 13 23 50.30 | +29 34 47.6 | 0.402 | 0.031 | 19.0 | 43.8 | 0.354 | 3.44 | 284 ± 202 | 418 ± 170 |
| RCS J132555+2852.4..... | 13 25 55.00 | +28 52 27.1 | 0.407 | 0.031 | 20.6 | 40.5 | 0.366 | 4.05 | 638 ± 236 | 499 ± 179 |
| RCS J132907+2840.7..... | 13 29 07.00 | +28 40 42.4 | 0.410 | 0.031 | 32.9 | 52.9 | 0.156 | 3.84 | 354 ± 211 | 423 ± 170 |
| RCS J132523+2919.4..... | 13 25 23.60 | +29 19 26.8 | 0.411 | 0.031 | 15.9 | 54.4 | 0.340 | 4.06 | 714 ± 243 | 502 ± 179 |
| RCS J132345+2941.0..... | 13 23 45.00 | +29 41 00.6 | 0.421 | 0.028 | 6.4 | 25.3 | 0.120 | 3.71 | 463 ± 222 | 541 ± 184 |
| RCS J132807+2902.6..... | 13 28 07.50 | +29 02 39.2 | 0.423 | 0.028 | 38.4 | 26.3 | 0.179 | 3.42 | 17 ± 179 | 23 ± 113 |
| RCS J133046+3032.5..... | 13 30 46.50 | +30 32 31.3 | 0.424 | 0.031 | 18.3 | 43.6 | 0.289 | 3.63 | 538 ± 230 | 503 ± 179 |
| RCS J132339+3044.1..... | 13 23 39.50 | +30 44 09.5 | 0.426 | 0.028 | 8.1 | 40.7 | 0.289 | 4.36 | 857 ± 256 | 583 ± 188 |
| RCS J132418+2955.0..... | 13 24 18.90 | +29 55 01.4 | 0.426 | 0.028 | 24.8 | 51.3 | 0.452 | 4.46 | 576 ± 233 | 422 ± 170 |
| RCS J132912+3011.1..... | 13 29 12.20 | +30 11 08.3 | 0.427 | 0.028 | 7.1 | 23.6 | 0.198 | 3.40 | 230 ± 202 | 256 ± 149 |
| RCS J132715+2959.7..... | 13 27 15.90 | +29 59 43.6 | 0.437 | 0.028 | 4.9 | 31.3 | 0.145 | 4.29 | 370 ± 217 | 418 ± 169 |
| RCS J132525+2935.8..... | 13 25 25.80 | +29 35 49.5 | 0.444 | 0.038 | 12.1 | 66.7 | 0.533 | 4.26 | 834 ± 258 | 505 ± 179 |
| RCS J132506+3024.8..... | 13 25 06.00 | +30 24 53.5 | 0.447 | 0.028 | 1.9 | 56.6 | 0.523 | 3.52 | 1136 ± 281 | 443 ± 172 |
| RCS J132427+2900.8..... | 13 24 27.30 | +29 00 48.8 | 0.448 | 0.025 | 7.3 | 43.0 | 0.521 | 3.36 | 264 ± 210 | 305 ± 155 |
| RCS J132625+2928.3..... | 13 26 25.40 | +29 28 23.8 | 0.450 | 0.028 | 28.1 | 56.7 | 0.438 | 3.76 | 494 ± 195 | 316 ± 141 |
| RCS J132750+2933.0..... | 13 27 50.40 | +29 33 00.2 | 0.455 | 0.028 | 3.6 | 73.3 | 0.522 | 3.86 | 676 ± 210 | 695 ± 179 |
| RCS J133206+3031.9..... | 13 32 06.70 | +30 31 57.9 | 0.457 | 0.028 | 21.6 | 48.1 | 0.545 | 3.39 | 407 ± 189 | 384 ± 148 |
| RCS J132731+2928.9..... | 13 27 31.00 | +29 28 58.4 | 0.465 | 0.025 | 34.9 | 55.9 | 0.361 | 3.72 | 571 ± 204 | 411 ± 152 |
| RCS J133123+3023.6..... | 13 31 23.00 | +30 23 40.0 | 0.467 | 0.025 | 8.5 | 78.4 | 0.545 | 4.35 | 285 ± 180 | 189 ± 127 |
| RCS J132504+2919.8..... | 13 25 04.90 | +29 19 49.3 | 0.467 | 0.025 | 16.2 | 34.0 | 0.042 | 3.46 | 348 ± 186 | 410 ± 152 |
| RCS J132723+2933.8..... | 13 27 23.10 | +29 33 49.9 | 0.484 | 0.025 | 14.8 | 41.0 | 0.279 | 3.36 | 485 ± 200 | 598 ± 170 |
| RCS J132959+2942.4..... | 13 29 59.30 | +29 42 25.9 | 0.486 | 0.023 | 60.5 | 77.8 | 0.381 | 4.05 | 322 ± 187 | 251 ± 134 |
| RCS J133045+2941.8..... | 13 30 45.30 | +29 41 48.4 | 0.491 | 0.022 | 45.6 | 65.7 | 0.556 | 3.42 | 412 ± 195 | 252 ± 134 |
| RCS J132344+2934.0..... | 13 23 44.70 | +29 34 02.1 | 0.494 | 0.023 | 31.1 | 104.1 | 0.652 | 4.04 | 725 ± 220 | 407 ± 152 |
| RCS J132636+2925.1..... | 13 26 36.30 | +29 25 07.0 | 0.499 | 0.023 | 9.5 | 61.0 | 0.418 | 3.99 | 600 ± 211 | 551 ± 166 |
| RCS J132907+2926.3..... | 13 29 07.60 | +29 26 21.8 | 0.499 | 0.023 | 36.5 | 34.6 | 0.035 | 4.74 | 655 ± 215 | 629 ± 173 |
| RCS J132441+2907.5..... | 13 24 41.60 | +29 07 32.6 | 0.501 | 0.022 | 59.9 | 68.6 | 0.446 | 3.69 | 401 ± 196 | 311 ± 142 |
| RCS J132608+2851.1..... | 13 26 08.30 | +28 51 07.1 | 0.502 | 0.025 | 27.8 | 66.5 | 0.332 | 5.00 | 810 ± 227 | 599 ± 170 |
| RCS J132504+2924.6..... | 13 25 04.80 | +29 24 40.9 | 0.502 | 0.022 | 83.1 | 51.5 | 0.453 | 4.23 | 462 ± 201 | 346 ± 145 |
| RCS J132452+2927.7..... | 13 24 52.50 | +29 27 46.4 | 0.503 | 0.023 | 15.9 | 33.1 | 0.121 | 3.43 | 524 ± 206 | 409 ± 152 |

TABLE 6—*Continued*

| Cluster | R.A. (J2000) | Decl. (J2000) | z | Δz | ΔBCG (arcsec) | Size (arcsec) | ϵ | σ_{peak} | $B_{\text{gc}T}$ (Mpc ^{1.8}) | $B_{\text{gc}R}$ (Mpc ^{1.8}) |
|-------------------------|--------------|---------------|-------|------------|--------------------------------|------------------|------------|------------------------|---|---|
| RCS J132608+2858.8..... | 13 26 08.30 | +28 58 49.2 | 0.504 | 0.022 | 8.6 | 31.2 | 0.131 | 3.64 | 366 ± 194 | 313 ± 142 |
| RCS J132913+2932.9..... | 13 29 13.80 | +29 32 59.9 | 0.506 | 0.022 | 49.5 | 92.8 | 0.673 | 3.39 | 330 ± 191 | 537 ± 164 |
| RCS J132938+3025.4..... | 13 29 38.20 | +30 25 24.0 | 0.508 | 0.020 | 24.9 | 24.4 | 0.178 | 3.41 | 170 ± 178 | 156 ± 123 |
| RCS J132335+3022.6..... | 13 23 35.80 | +30 22 39.1 | 0.508 | 0.031 | 23.9 | 81.0 | 0.184 | 6.19 | 2163 ± 307 | 2053 ± 274 |
| RCS J133017+2944.0..... | 13 30 17.50 | +29 44 04.2 | 0.509 | 0.020 | 39.7 | 44.1 | 0.426 | 4.11 | 459 ± 202 | 391 ± 150 |
| RCS J132617+2933.3..... | 13 26 17.70 | +29 33 23.4 | 0.509 | 0.031 | 64.8 | 67.1 | 0.239 | 5.17 | 894 ± 234 | 885 ± 195 |
| RCS J132422+2946.7..... | 13 24 22.70 | +29 46 44.0 | 0.509 | 0.020 | 29.7 | 47.4 | 0.412 | 4.12 | 672 ± 218 | 569 ± 167 |
| RCS J132931+2913.4..... | 13 29 31.60 | +29 13 29.5 | 0.511 | 0.022 | 23.3 | 65.0 | 0.322 | 4.65 | 987 ± 240 | 948 ± 200 |
| RCS J132940+2835.3..... | 13 29 40.00 | +28 35 20.6 | 0.516 | 0.020 | 7.5 | 36.9 | 0.382 | 3.95 | 446 ± 203 | 600 ± 170 |
| RCS J132412+3024.2..... | 13 24 12.90 | +30 24 13.0 | 0.523 | 0.018 | 17.2 | 19.6 | 0.111 | 3.33 | 177 ± 182 | 284 ± 138 |
| RCS J133220+3003.1..... | 13 32 20.70 | +30 03 09.8 | 0.526 | 0.018 | 15.8 | 31.5 | 0.230 | 4.12 | 24 ± 172 | 85 ± 114 |
| RCS J132935+2857.9..... | 13 29 35.50 | +28 57 58.1 | 0.526 | 0.018 | 29.5 | 28.3 | 0.138 | 3.95 | 79 ± 174 | 128 ± 118 |
| RCS J133119+2835.5..... | 13 31 19.10 | +28 35 32.4 | 0.526 | 0.023 | 7.9 | 49.7 | 0.539 | 3.83 | 444 ± 204 | 555 ± 166 |
| RCS J133012+2927.4..... | 13 30 12.40 | +29 27 27.5 | 0.527 | 0.018 | 53.0 | 30.2 | 0.224 | 3.37 | 169 ± 183 | 193 ± 126 |
| RCS J133109+2836.9..... | 13 31 09.30 | +28 36 54.7 | 0.531 | 0.018 | 18.1 | 32.9 | 0.211 | 4.26 | 163 ± 183 | 320 ± 141 |
| RCS J132708+2954.8..... | 13 27 08.90 | +29 54 53.5 | 0.532 | 0.018 | 13.7 | 55.6 | 0.404 | 3.72 | 658 ± 221 | 392 ± 149 |
| RCS J132710+2931.5..... | 13 27 10.90 | +29 31 34.3 | 0.540 | 0.016 | 16.6 | 36.4 | 0.362 | 3.45 | 343 ± 199 | 225 ± 130 |
| RCS J132856+2839.1..... | 13 28 56.50 | +28 39 09.4 | 0.540 | 0.016 | 25.1 | 25.9 | 0.159 | 3.39 | 602 ± 232 | 479 ± 167 |
| RCS J132913+2835.8..... | 13 29 13.40 | +28 35 52.1 | 0.549 | 0.016 | 23.8 | 68.4 | 0.525 | 3.64 | 210 ± 204 | 503 ± 172 |
| RCS J132721+3000.3..... | 13 27 21.80 | +30 00 19.9 | 0.552 | 0.016 | 63.6 | 51.4 | 0.453 | 3.30 | 323 ± 200 | 198 ± 126 |
| RCS J132527+3033.4..... | 13 25 27.70 | +30 33 27.9 | 0.556 | 0.018 | 30.4 | 79.3 | 0.644 | 3.38 | 380 ± 205 | 451 ± 154 |
| RCS J132723+2924.7..... | 13 27 23.10 | +29 24 46.7 | 0.566 | 0.014 | 24.0 | 27.6 | 0.157 | 3.35 | 206 ± 194 | 138 ± 117 |
| RCS J132538+3027.9..... | 13 25 38.10 | +30 27 56.4 | 0.567 | 0.014 | 33.3 | 32.5 | 0.290 | 3.78 | 649 ± 227 | 233 ± 129 |
| RCS J132720+2955.4..... | 13 27 20.40 | +29 55 25.9 | 0.568 | 0.014 | 5.8 | 25.7 | 0.196 | 3.76 | 518 ± 218 | 330 ± 140 |
| RCS J133201+2845.9..... | 13 32 01.70 | +28 45 57.4 | 0.577 | 0.031 | 41.8 | 47.7 | 0.173 | 4.49 | 1284 ± 269 | 663 ± 174 |
| RCS J132910+2849.3..... | 13 29 10.20 | +28 49 20.1 | 0.579 | 0.014 | 51.6 | 78.3 | 0.628 | 3.52 | 468 ± 217 | 430 ± 151 |
| RCS J132732+2933.5..... | 13 27 32.10 | +29 33 34.6 | 0.581 | 0.014 | 115.6 | 68.0 | 0.465 | 4.12 | 372 ± 210 | 426 ± 151 |
| RCS J132357+2907.4..... | 13 23 57.40 | +29 07 28.5 | 0.599 | 0.015 | 15.5 | 21.1 | 0.165 | 3.44 | 219 ± 202 | 84 ± 108 |
| RCS J133229+3000.4..... | 13 32 29.70 | +30 00 29.3 | 0.599 | 0.015 | 29.5 | 23.8 | 0.171 | 3.37 | 267 ± 230 | 217 ± 141 |
| RCS J132549+3020.0..... | 13 25 49.30 | +30 20 05.0 | 0.614 | 0.015 | 7.6 | 22.0 | 0.077 | 3.55 | 354 ± 215 | 214 ± 124 |
| RCS J132810+3019.2..... | 13 28 10.20 | +30 19 16.5 | 0.619 | 0.015 | 75.3 | 42.6 | 0.407 | 4.27 | 601 ± 233 | 278 ± 132 |
| RCS J132541+3028.7..... | 13 25 41.20 | +30 28 42.7 | 0.627 | 0.016 | 28.0 | 43.4 | 0.259 | 4.20 | 818 ± 249 | 357 ± 141 |
| RCS J132455+3005.3..... | 13 24 55.30 | +30 05 19.5 | 0.628 | 0.015 | 4.3 | 27.0 | 0.263 | 3.67 | 362 ± 220 | 487 ± 156 |
| RCS J133136+3029.7..... | 13 31 36.10 | +30 29 46.7 | 0.639 | 0.016 | 18.8 | 19.7 | 0.116 | 3.33 | 149 ± 218 | 183 ± 127 |
| RCS J133125+3032.9..... | 13 31 25.20 | +30 32 59.4 | 0.640 | 0.018 | 3.9 | 57.5 | 0.695 | 3.50 | 168 ± 222 | −36 ± 98 |
| RCS J133051+2924.2..... | 13 30 51.50 | +29 24 17.5 | 0.641 | 0.018 | 6.1 | 21.8 | 0.220 | 3.31 | 31 ± 195 | 158 ± 116 |
| RCS J133135+3044.9..... | 13 31 35.70 | +30 44 54.6 | 0.645 | 0.016 | 0.8 | 56.3 | 0.246 | 3.83 | 846 ± 253 | 475 ± 153 |
| RCS J132828+2902.7..... | 13 28 28.20 | +29 02 47.6 | 0.651 | 0.018 | 18.4 | 21.4 | 0.164 | 3.30 | 278 ± 218 | 172 ± 119 |
| RCS J132644+2842.3..... | 13 26 44.40 | +28 42 21.9 | 0.666 | 0.021 | 13.7 | 21.7 | 0.169 | 3.38 | −94 ± 232 | 88 ± 123 |
| RCS J132454+3052.3..... | 13 24 54.40 | +30 52 18.5 | 0.672 | 0.018 | 19.7 | 23.0 | 0.182 | 3.36 | 311 ± 228 | 154 ± 116 |
| RCS J132503+3043.9..... | 13 25 03.40 | +30 43 54.4 | 0.677 | 0.016 | 42.6 | 83.8 | 0.673 | 3.50 | 828 ± 265 | 466 ± 155 |
| RCS J132718+3034.5..... | 13 27 18.10 | +30 34 34.3 | 0.678 | 0.021 | 8.0 | 20.1 | 0.108 | 3.62 | −195 ± 205 | 124 ± 112 |
| RCS J133154+3036.1..... | 13 31 54.10 | +30 36 11.5 | 0.686 | 0.018 | 14.4 | 51.7 | 0.525 | 3.55 | 283 ± 251 | 237 ± 141 |
| RCS J132838+3005.1..... | 13 28 38.90 | +30 05 08.8 | 0.686 | 0.021 | 6.1 | 19.5 | 0.132 | 3.38 | 240 ± 221 | 77 ± 102 |
| RCS J133120+2908.4..... | 13 31 20.70 | +29 08 25.1 | 0.690 | 0.021 | 21.5 | 31.4 | 0.349 | 3.37 | 431 ± 234 | 453 ± 149 |
| RCS J133144+3041.1..... | 13 31 44.20 | +30 41 07.4 | 0.692 | 0.021 | 79.2 | 61.4 | 0.487 | 3.54 | 508 ± 240 | 366 ± 139 |
| RCS J133216+3022.7..... | 13 32 16.00 | +30 22 47.0 | 0.697 | 0.021 | 4.1 | 38.4 | 0.227 | 3.32 | 677 ± 274 | 479 ± 165 |
| RCS J132657+3029.5..... | 13 26 57.40 | +30 29 34.1 | 0.697 | 0.021 | 27.2 | 45.0 | 0.453 | 3.92 | 729 ± 262 | 437 ± 151 |
| RCS J133155+3049.6..... | 13 31 55.90 | +30 49 41.0 | 0.700 | 0.021 | 34.8 | 56.3 | 0.081 | 3.62 | 1010 ± 275 | 474 ± 152 |
| RCS J132728+2942.1..... | 13 27 28.80 | +29 42 06.0 | 0.700 | 0.021 | 1.4 | 22.3 | 0.134 | 3.36 | 158 ± 226 | 1 ± 92 |
| RCS J133140+3051.5..... | 13 31 40.40 | +30 51 30.9 | 0.701 | 0.021 | 16.5 | 24.3 | 0.080 | 3.80 | 685 ± 255 | 214 ± 121 |
| RCS J132421+3012.6..... | 13 24 21.00 | +30 12 39.3 | 0.708 | 0.014 | 4.1 | 45.5 | 0.276 | 4.92 | 1634 ± 334 | 893 ± 206 |
| RCS J133000+2916.5..... | 13 30 00.30 | +29 16 34.8 | 0.710 | 0.021 | 17.4 | 23.9 | 0.105 | 4.00 | 80 ± 214 | 242 ± 124 |
| RCS J132402+3044.2..... | 13 24 02.10 | +30 44 12.2 | 0.714 | 0.015 | 38.4 | 78.4 | 0.547 | 3.81 | 1068 ± 304 | 786 ± 199 |
| RCS J132453+2925.3..... | 13 24 53.20 | +29 25 23.0 | 0.717 | 0.020 | 3.0 | 23.4 | 0.247 | 3.38 | 14 ± 223 | 93 ± 109 |
| RCS J132446+3047.9..... | 13 24 46.60 | +30 47 58.3 | 0.717 | 0.021 | 12.6 | 35.9 | 0.318 | 3.64 | 966 ± 291 | 499 ± 164 |
| RCS J132417+2851.2..... | 13 24 17.90 | +28 51 13.5 | 0.719 | 0.020 | 10.2 | 25.8 | 0.184 | 3.90 | 407 ± 265 | 399 ± 159 |
| RCS J133004+2911.5..... | 13 30 04.20 | +29 11 33.2 | 0.723 | 0.020 | 37.0 | 27.7 | 0.213 | 3.70 | 185 ± 228 | 376 ± 143 |
| RCS J133131+3048.2..... | 13 31 31.60 | +30 48 15.2 | 0.729 | 0.020 | 1.4 | 27.6 | 0.167 | 3.33 | 524 ± 255 | 274 ± 130 |
| RCS J132718+2919.4..... | 13 27 18.00 | +29 19 24.9 | 0.743 | 0.018 | 31.8 | 41.1 | 0.402 | 3.39 | 318 ± 261 | 441 ± 162 |
| RCS J132821+3031.3..... | 13 28 21.50 | +30 31 22.5 | 0.749 | 0.018 | 3.8 | 25.0 | 0.167 | 3.60 | 129 ± 229 | 174 ± 114 |
| RCS J133053+2932.1..... | 13 30 53.90 | +29 32 11.3 | 0.753 | 0.017 | 17.4 | 25.5 | 0.212 | 3.58 | 268 ± 256 | 192 ± 125 |
| RCS J132449+3011.6..... | 13 24 49.20 | +30 11 36.1 | 0.755 | 0.018 | 6.2 | 41.4 | 0.048 | 3.66 | 1170 ± 333 | 594 ± 185 |
| RCS J133147+3040.6..... | 13 31 47.10 | +30 40 37.8 | 0.759 | 0.017 | 7.9 | 24.1 | 0.167 | 3.46 | 217 ± 246 | 282 ± 134 |
| RCS J133201+2855.8..... | 13 32 01.30 | +28 55 48.4 | 0.767 | 0.018 | 11.8 | 17.6 | 0.020 | 3.34 | −5 ± 220 | 234 ± 118 |

TABLE 6—*Continued*

| Cluster | R.A. (J2000) | Decl. (J2000) | z | Δz | ΔBCG (arcsec) | Size (arcsec) | ϵ | σ_{peak} | $B_{\text{gc}T}$ (Mpc ^{1.8}) | $B_{\text{gc}R}$ (Mpc ^{1.8}) |
|-------------------------|--------------|---------------|-------|------------|--------------------------------|------------------|------------|------------------------|---|---|
| RCS J132935+2931.1..... | 13 29 35.90 | +29 31 10.7 | 0.771 | 0.018 | 32.0 | 26.1 | 0.184 | 3.57 | 1095 \pm 334 | 370 \pm 158 |
| RCS J132620+3033.2..... | 13 26 20.10 | +30 33 16.1 | 0.771 | 0.017 | 8.7 | 25.6 | 0.217 | 3.51 | 141 \pm 248 | 231 \pm 128 |
| RCS J132454+2948.3..... | 13 24 54.30 | +29 48 18.4 | 0.771 | 0.017 | 7.4 | 30.2 | 0.432 | 3.34 | 100 \pm 269 | 168 \pm 131 |
| RCS J133006+2932.2..... | 13 30 06.90 | +29 32 17.9 | 0.778 | 0.017 | 28.1 | 48.9 | 0.515 | 3.60 | 1075 \pm 314 | 547 \pm 169 |
| RCS J132427+2940.7..... | 13 24 27.90 | +29 40 43.8 | 0.779 | 0.017 | 25.2 | 24.2 | 0.272 | 3.30 | 361 \pm 299 | 229 \pm 144 |
| RCS J132911+2857.0..... | 13 29 11.20 | +28 57 03.6 | 0.795 | 0.018 | 15.3 | 44.9 | 0.465 | 3.77 | 1084 \pm 361 | 548 \pm 192 |
| RCS J132736+2908.7..... | 13 27 36.90 | +29 08 47.1 | 0.796 | 0.017 | 38.0 | 50.2 | 0.461 | 3.44 | 32 \pm 281 | 352 \pm 166 |
| RCS J132419+2844.7..... | 13 24 19.60 | +28 44 47.7 | 0.802 | 0.018 | 24.3 | 29.4 | 0.308 | 3.60 | 295 \pm 294 | 226 \pm 139 |
| RCS J132346+2904.0..... | 13 23 46.20 | +29 04 02.4 | 0.817 | 0.018 | 8.1 | 47.8 | 0.293 | 4.05 | 1012 \pm 362 | 860 \pm 230 |
| RCS J133136+2911.6..... | 13 31 36.70 | +29 11 41.4 | 0.830 | 0.019 | 12.6 | 24.2 | 0.110 | 3.96 | 208 \pm 274 | 227 \pm 129 |
| RCS J132829+3021.9..... | 13 28 29.50 | +30 21 57.4 | 0.837 | 0.024 | 10.8 | 27.9 | 0.271 | 3.38 | 251 \pm 252 | 259 \pm 119 |
| RCS J132556+3010.1..... | 13 25 56.10 | +30 10 10.7 | 0.842 | 0.018 | 11.8 | 37.4 | 0.422 | 3.74 | 1486 \pm 366 | 500 \pm 170 |
| RCS J132809+3020.9..... | 13 28 09.40 | +30 20 58.4 | 0.855 | 0.019 | 1.8 | 20.0 | 0.048 | 3.57 | 445 \pm 282 | 271 \pm 128 |
| RCS J132823+2853.7..... | 13 28 23.30 | +28 53 42.8 | 0.873 | 0.028 | 16.9 | 30.5 | 0.288 | 3.30 | 437 \pm 335 | 317 \pm 159 |
| RCS J133150+2956.5..... | 13 31 50.00 | +29 56 32.0 | 0.874 | 0.028 | 8.8 | 17.8 | 0.063 | 3.42 | 418 \pm 271 | 270 \pm 120 |
| RCS J133138+2940.2..... | 13 31 38.60 | +29 40 15.1 | 0.882 | 0.028 | 16.0 | 23.3 | 0.078 | 3.32 | 294 \pm 305 | 315 \pm 148 |
| RCS J132639+2838.1..... | 13 26 39.70 | +28 38 10.6 | 0.886 | 0.028 | 7.4 | 23.1 | 0.047 | 3.61 | 500 \pm 550 | 386 \pm 259 |
| RCS J132437+2844.4..... | 13 24 37.90 | +28 44 24.5 | 0.888 | 0.024 | 8.4 | 24.5 | 0.286 | 3.44 | 1226 \pm 404 | 456 \pm 184 |
| RCS J132955+3051.6..... | 13 29 55.40 | +30 51 38.1 | 0.889 | 0.028 | 40.8 | 43.3 | 0.458 | 3.44 | 650 \pm 416 | 245 \pm 170 |
| RCS J132914+3009.4..... | 13 29 14.20 | +30 09 28.3 | 0.894 | 0.019 | 75.7 | 55.3 | 0.452 | 3.41 | 952 \pm 387 | 502 \pm 190 |
| RCS J133154+2918.7..... | 13 31 54.10 | +29 18 44.2 | 0.896 | 0.028 | 33.8 | 25.1 | 0.121 | 3.43 | 539 \pm 288 | 295 \pm 126 |
| RCS J132926+3004.1..... | 13 29 26.40 | +30 04 10.4 | 0.900 | 0.028 | 2.3 | 23.3 | 0.163 | 3.77 | 505 \pm 492 | 460 \pm 248 |
| RCS J132939+2853.3..... | 13 29 39.40 | +28 53 18.2 | 0.907 | 0.028 | 10.6 | 31.8 | 0.301 | 3.56 | 1012 \pm 457 | 613 \pm 237 |
| RCS J132924+2914.8..... | 13 29 24.30 | +29 14 50.4 | 0.907 | 0.028 | 2.1 | 19.6 | 0.083 | 3.32 | 58 \pm 331 | 305 \pm 164 |
| RCS J132342+3052.4..... | 13 23 42.30 | +30 52 29.9 | 0.909 | 0.031 | 20.1 | 24.8 | 0.243 | 3.38 | 419 \pm 380 | 283 \pm 168 |
| RCS J132336+3007.9..... | 13 23 36.20 | +30 07 57.9 | 0.920 | 0.028 | 15.4 | 24.3 | 0.179 | 3.39 | 1068 \pm 478 | 495 \pm 223 |
| RCS J132900+2907.3..... | 13 29 00.00 | +29 07 21.2 | 0.925 | 0.031 | 22.9 | 30.0 | 0.244 | 3.40 | 1276 \pm 501 | 283 \pm 186 |
| RCS J132400+2925.7..... | 13 24 00.20 | +29 25 44.1 | 0.926 | 0.024 | 3.8 | 22.8 | 0.212 | 3.57 | 501 \pm 415 | 527 \pm 220 |
| RCS J132454+2857.9..... | 13 24 54.70 | +28 57 58.3 | 0.927 | 0.028 | 15.4 | 45.4 | 0.515 | 3.30 | 1479 \pm 461 | 402 \pm 187 |
| RCS J132645+2959.8..... | 13 26 45.20 | +29 59 48.3 | 0.930 | 0.024 | 70.1 | 44.3 | 0.204 | 3.87 | 1350 \pm 441 | 557 \pm 206 |
| RCS J132904+3041.7..... | 13 29 04.20 | +30 41 47.7 | 0.936 | 0.019 | 81.4 | 81.3 | 0.441 | 3.40 | 1223 \pm 368 | 426 \pm 158 |
| RCS J133215+2944.4..... | 13 32 15.70 | +29 44 24.3 | 0.950 | 0.031 | 11.0 | 37.2 | 0.395 | 3.83 | 426 \pm 315 | 200 \pm 119 |
| RCS J132629+2903.1..... | 13 26 29.70 | +29 03 06.2 | 0.952 | 0.017 | 18.4 | 46.1 | 0.337 | 5.07 | 2607 \pm 596 | 1636 \pm 369 |
| RCS J133028+2838.7..... | 13 30 28.10 | +28 38 44.6 | 0.958 | 0.031 | 7.2 | 19.9 | 0.143 | 3.42 | 326 \pm 471 | 183 \pm 177 |
| RCS J132428+2924.3..... | 13 24 28.80 | +29 24 23.4 | 0.962 | 0.031 | 47.8 | 28.7 | 0.300 | 3.47 | 96 \pm 395 | 468 \pm 212 |
| RCS J132928+3023.6..... | 13 29 28.80 | +30 23 40.1 | 0.976 | 0.039 | 23.9 | 17.4 | 0.048 | 3.39 | −415 \pm 553 | 129 \pm 196 |
| RCS J132346+2926.2..... | 13 23 46.80 | +29 26 16.4 | 0.984 | 0.031 | 49.3 | 48.0 | 0.566 | 3.38 | 1218 \pm 538 | 396 \pm 216 |
| RCS J132427+2845.2..... | 13 24 27.60 | +28 45 14.8 | 0.997 | 0.017 | 20.2 | 68.6 | 0.404 | 4.06 | 3667 \pm 697 | 1852 \pm 405 |
| RCS J132540+2925.2..... | 13 25 40.10 | +29 25 13.6 | 1.041 | 0.028 | 45.4 | 45.8 | 0.435 | 3.60 | 1375 \pm 554 | 542 \pm 238 |
| RCS J133121+2835.6..... | 13 31 21.40 | +28 35 37.0 | 1.082 | 0.039 | 43.8 | 38.5 | 0.513 | 3.40 | 1046 \pm 635 | 195 \pm 198 |
| RCS J133027+3023.0..... | 13 30 27.60 | +30 23 03.4 | 1.115 | 0.039 | 2.9 | 27.9 | 0.259 | 3.56 | −215 \pm 923 | 666 \pm 434 |
| RCS J133002+3002.9..... | 13 30 02.50 | +30 02 59.3 | 1.124 | 0.024 | 5.7 | 20.6 | 0.171 | 3.34 | 1438 \pm 1157 | 520 \pm 423 |
| RCS J132359+3023.7..... | 13 23 59.20 | +30 23 46.6 | 1.148 | 0.039 | 35.1 | 23.2 | 0.117 | 3.48 | 2678 \pm 965 | 886 \pm 398 |
| RCS J132803+3013.6..... | 13 28 03.10 | +30 13 36.6 | 1.157 | 0.059 | 11.8 | 21.9 | 0.220 | 3.37 | 1719 \pm 624 | 540 \pm 237 |
| RCS J133159+3046.5..... | 13 31 59.80 | +30 46 30.2 | 1.176 | 0.039 | 90.0 | 33.1 | 0.383 | 3.53 | 371 \pm 682 | 464 \pm 274 |
| RCS J133222+2857.5..... | 13 32 22.70 | +28 57 31.2 | 1.191 | 0.039 | 8.6 | 24.9 | 0.362 | 3.31 | 435 \pm 613 | 463 \pm 244 |
| RCS J133202+2930.6..... | 13 32 02.10 | +29 30 36.0 | 1.250 | 0.059 | 10.0 | 38.4 | 0.251 | 4.01 | 795 \pm 901 | 1074 \pm 435 |
| RCS J132423+3010.7..... | 13 24 23.10 | +30 10 42.3 | 1.276 | 0.039 | 17.4 | 26.2 | 0.345 | 3.50 | 7446 \pm 2351 | 2638 \pm 1039 |
| RCS J132915+3019.2..... | 13 29 15.80 | +30 19 16.2 | 1.278 | 0.059 | 28.3 | 35.4 | 0.208 | 4.27 | 1117 \pm 844 | 1216 \pm 418 |
| RCS J132347+3012.4..... | 13 23 47.40 | +30 12 29.5 | 1.279 | 0.059 | 30.2 | 25.9 | 0.107 | 3.80 | 352 \pm 1444 | 928 \pm 598 |
| RCS J132447+3031.9..... | 13 24 47.20 | +30 31 59.1 | 1.282 | 0.133 | 48.1 | 28.9 | 0.397 | 3.36 | 225 \pm 1257 | 529 \pm 445 |
| RCS J132811+2938.5..... | 13 28 11.30 | +29 38 35.1 | 1.286 | 0.133 | 66.0 | 37.5 | 0.498 | 3.31 | 365 \pm 1350 | 577 \pm 480 |
| RCS J132935+2900.6..... | 13 29 35.10 | +29 00 41.6 | 1.306 | 0.133 | 4.6 | 19.4 | 0.109 | 3.51 | 1113 \pm 2078 | 153 \pm 496 |
| RCS J133220+2923.7..... | 13 32 20.00 | +29 23 46.3 | 1.329 | 0.133 | 26.4 | 19.0 | 0.022 | 3.62 | −317 \pm 842 | 509 \pm 314 |
| RCS J132706+2935.6..... | 13 27 06.40 | +29 35 36.0 | 1.358 | 0.175 | 15.2 | 20.0 | 0.088 | 3.44 | 603 \pm 1671 | 347 \pm 484 |

NOTES.—Units of right ascension are hours, minutes, and seconds, and units of declination are degrees, arcminutes, and arcseconds. Table 6 is also available in machine-readable form in the electronic edition of the *Astrophysical Journal Supplement*.

comparison to other clusters of similar significance and redshift may indicate a projection of some sort. In any obvious cases of projections or double clusters we resist the temptation to modify objects individually, preferring instead to define a catalog based strictly on a single algorithm. This facilitates automated comparison to future modeling efforts.

The expected false-positive contamination rate for the combined catalog is discussed extensively elsewhere (M. D. Gladders & H. K. C. Yee 2005, in preparation). Projection effects due to the clustering and random projection of nominally field galaxies is expected to be less than 5% at all redshifts, consistent with that seen in an empirical test using a combination of photometric and

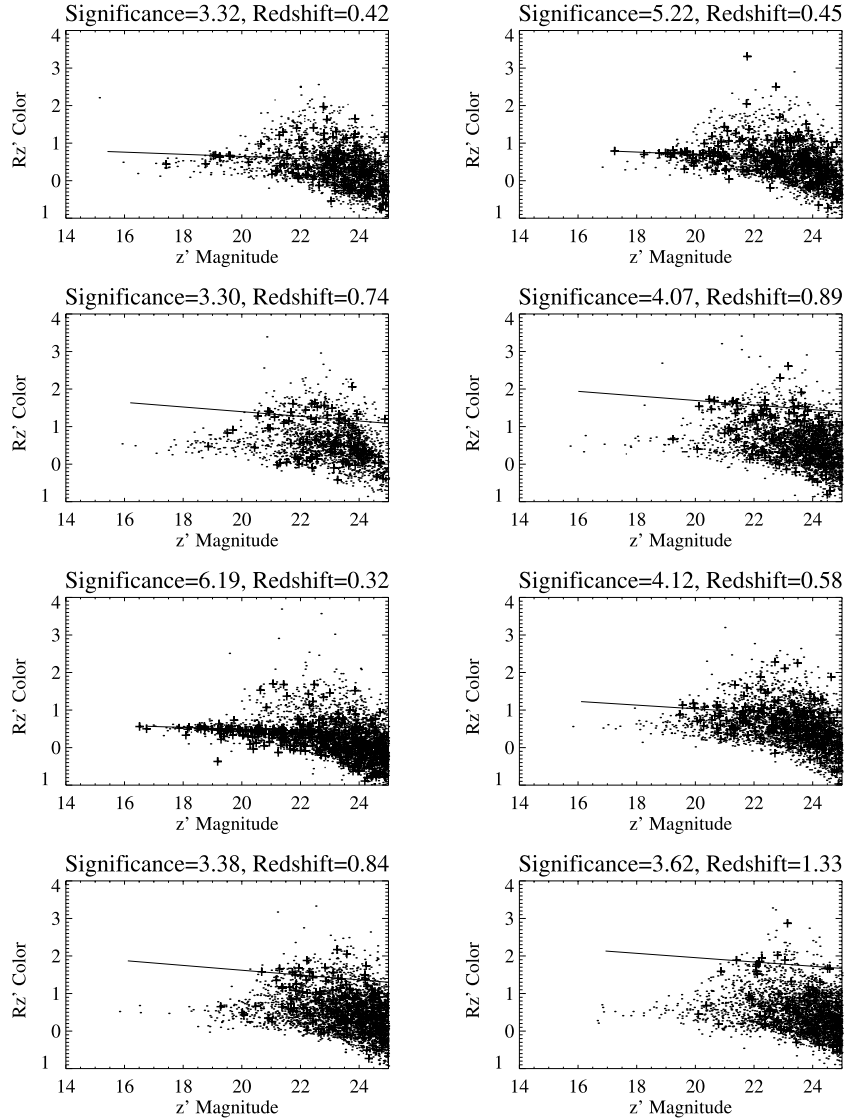


FIG. 14.—Representative color-magnitude diagrams. Four color-magnitude diagrams from each of the patches are shown, spanning a representative range of redshift and detection significance. The top four panels are from the patch RCS 0926+37, and the bottom four are from the patch RCS 1327+29. Only galaxies with color errors less than 1.0 mag are shown. Galaxies within 0.5 Mpc radius of the fiducial cluster center are plotted in heavy symbols, with all other galaxies on the same chip (and hence with essentially identical sampling) plotted as points. The location of the fiducial red sequence in each cluster, following the models discussed in § 2.1, is indicated by the solid near-horizontal line.

redshift data from the much smaller CNOC2 Survey (Gladders & Yee 2000). A larger fraction of all clusters in Tables 5 and 6 will have some amount of projected structure; these are real clusters, but their apparent properties may be modified by projection of galaxies from nearby clusters and groups in the cosmic web. Such cases of associated multiple structures are in part distinguishable by the size and shape criteria outlined above.

Figure 14 provides example color-magnitude plots for representative clusters from Tables 5 and 6. In some cases, particularly for lower significance systems, the red sequence is not overwhelmingly apparent to casual examination. For such systems it is the aggregate signal in color, magnitude, and position that results in a detection, and direct visual examination does not always yield similar confidence.

Figures 15a–15bi show color images of each clusters listed in Table 5, for the patch RCS 0926+37. Figures 16a–16au similarly show all clusters in Table 6 for the patch RCS 1327+29. (The print edition of the Supplement shows only a sample panel

of these figures; see the electronic edition for the complete sets.) Each figure provides color images of four clusters, constructed from the R_C and z' survey images. These are overlaid by a contour map of the projected σ_{ij} map, as used above to estimate the cluster size. For each cluster a larger scale version of this map is also shown, which give a visual indication of possible nearby clusters, many of which will themselves be listed in Tables 5 and 6.

6.2.2. Redshift Calibration and Uncertainties

The red-sequence model used for the cluster finding presented here is the $z_f = 2.5$ model described in § 2.1. The model has been fine-tuned by adjusting the color to match the redshifts of several known clusters in the patch RCS 1327+29. The required color adjustment is a few hundredths of a magnitude, well within the expected uncertainties between absolute calibration of the photometry and the modeling. Initial spectroscopy of a subset of RCS clusters at redshifts $0.2 < z < 1.0$ shows that the redshifts

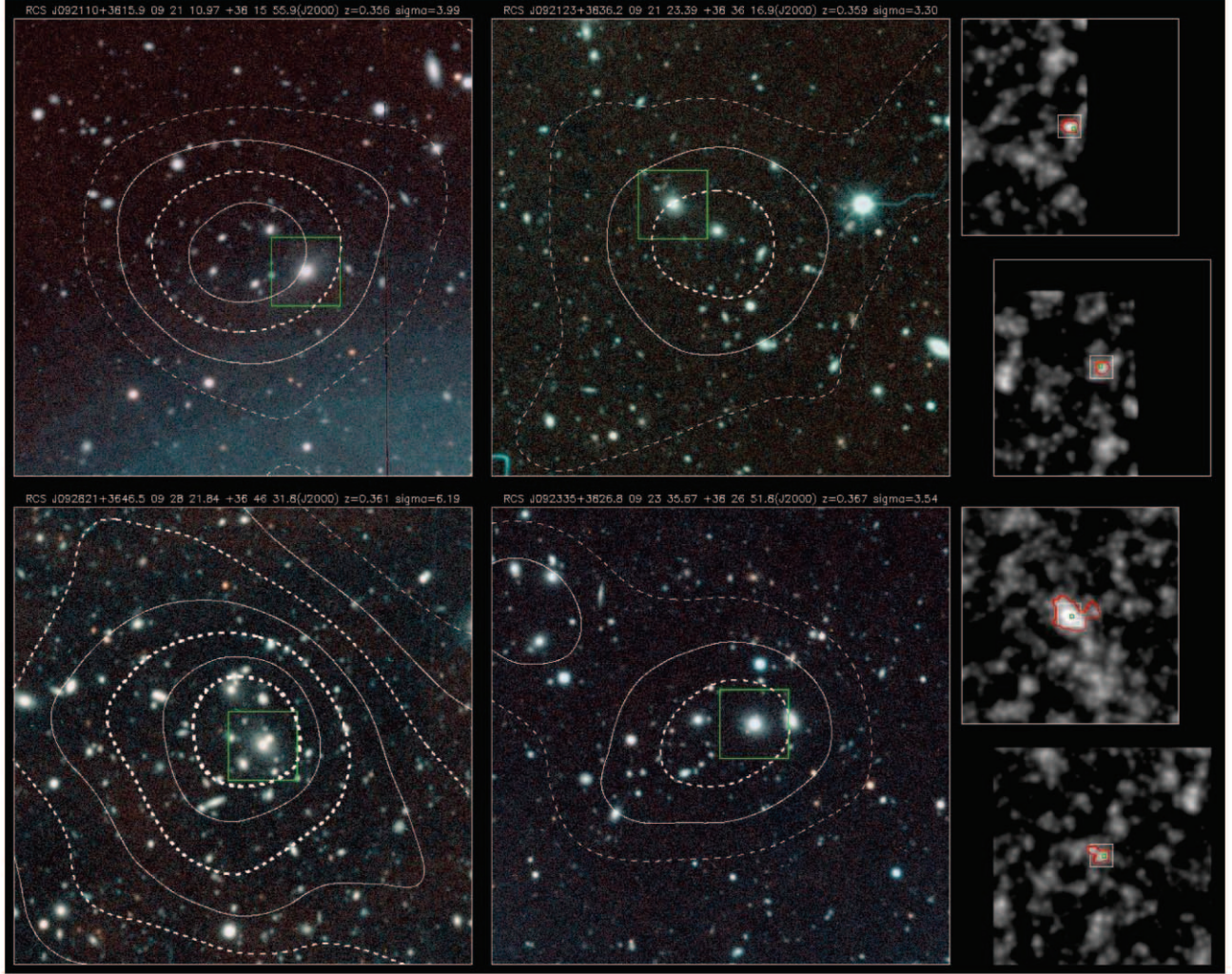


FIG. 15.—Clusters in the patch RCS 0926+37. Color images of all clusters identified in Table 5. The images are a color composite of the R_C and z' images, with a logarithmic stretch adjusted with redshift to reasonably display the wide range of cluster galaxy luminosities seen across the sample. When necessary, a simple astrometric mapping has been used to stitch together data from different chips. No effort has been made to ensure fidelity in the displayed colors across different chips; these images are illustrative only. Clusters are shown four per figure, and are sorted by redshift, lowest to highest, as in Table 5. The galaxy density for galaxies corresponding to the cluster red sequence is overlaid in each case in white contours. The lowest contour level is 2.0σ , and the highest is 5.0σ , with contours drawn with increasingly thick lines in alternating line styles at 0.5σ intervals. The green box (when present within this field of view) indicates the brightest cluster galaxy, selected as described in the main text. Clusters are shown in the order top left, top right, bottom left, and bottom right. Corresponding gray-scale images of a larger region also showing the red sequence galaxy density are placed running top to bottom along the right side of each figure. In these images the white square indicates the region corresponding to the color survey image shown in detail to the left, and the green box similarly indicates the position of the brightest cluster galaxy. The red contour indicates the outer 2.5σ boundary of each peak, projected in redshift. The large gray-scale plots are typically $30' \times 30'$ in size, except for clusters near the boundary of a patch. All clusters images and galaxy density plots are shown with north up and east to the left. [See the electronic edition of the Supplement for additional panels of this figure.]

derived from the photometry are typically accurate to better than 0.05 over this redshift range (Gladders 2003), and possibly as good as 0.03 in fields with optimal photometric calibration. Extensive modeling of the RCS data (M. D. Gladders & H. K. C. Yee 2005, in preparation) confirms this expected (Gladders & Yee 2000) result and suggests that redshift errors should increase at the lowest redshifts and at $z > 1$. At the highest redshifts, the 1σ uncertainty in the photometric redshifts is approximately 0.1, resulting from a combination of poorer sampling of the 4000 \AA break by the R_C and z' filters, and larger photometric uncertainties on the increasingly faint and red cluster galaxies. At the highest redshifts there is also a fundamental ambiguity regarding the appropriateness of the particular red-sequence model used, in that changes in the details of the model produce significant changes in the expected colors of the cluster red sequence at

$z > 1$ (Gladders 2003). Additionally, the near-degeneracy between $R_C - z'$ color and redshift at $z \sim 1$ (see Fig. 1) tends to scatter clusters at $z \sim 1$ to either slightly higher or lower redshifts, more so than at other redshifts, which results in an apparent depopulation of the cluster population at that redshift.

6.2.3. Richness Estimates

Tables 5 and 6 also provide a richness estimate for each cluster. The clusters in the catalogs are characterized by the richness parameter B_{gc} , the amplitude of the cluster-center–galaxy correlation function computed individually for each cluster assuming a distribution of excess galaxies of the form $\xi(r) \sim B_{gc} r^{-1.8}$ (see Yee & López-Cruz 1999 for a detailed discussion of the derivation and properties of the parameter). The B_{gc} parameter has been found to be a robust richness estimator (Yee & López-Cruz

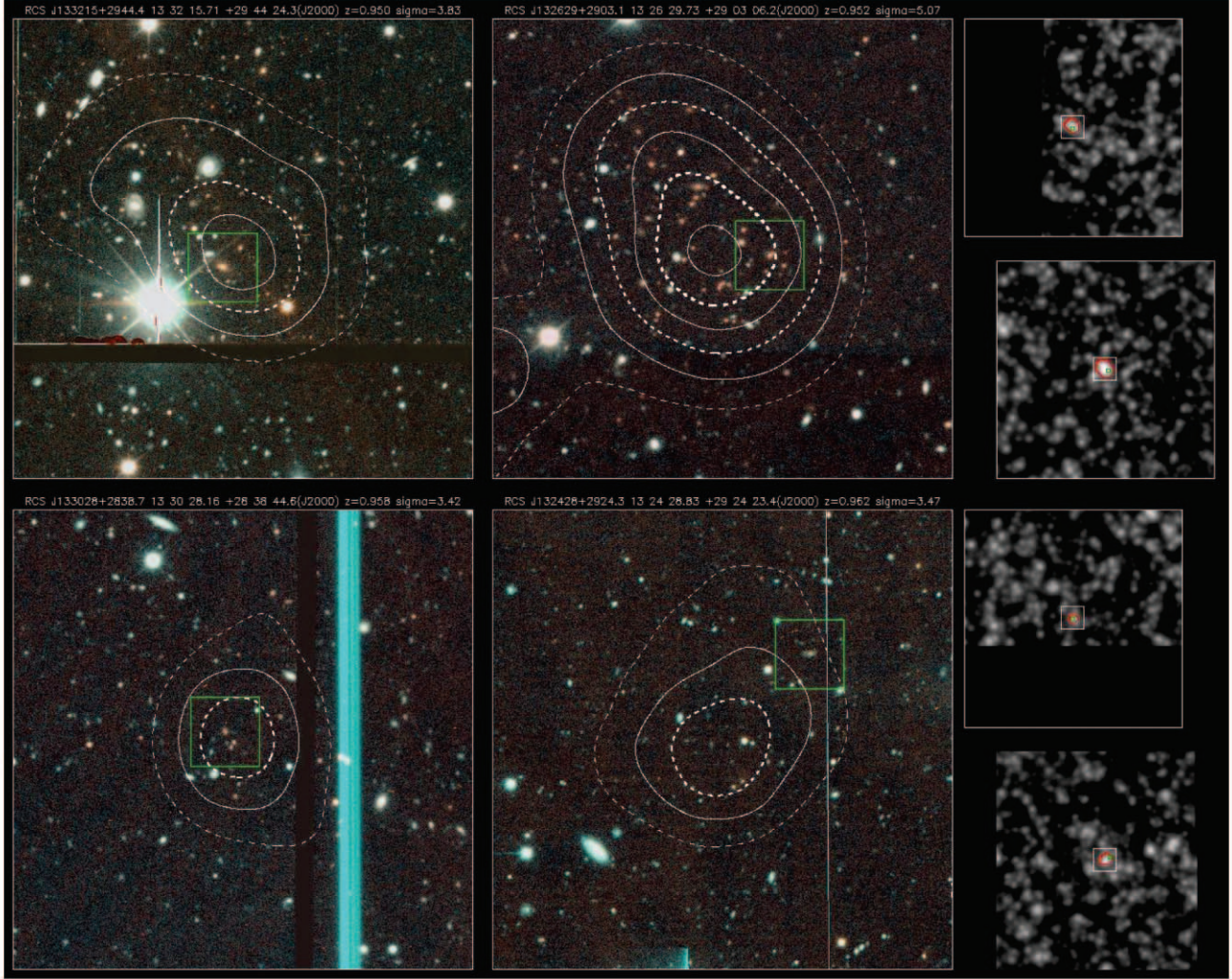


FIG. 16.—Clusters in the patch RCS 1327+29. Color images of all clusters identified in Table 6. The layout is identical to Fig. 15. [See the electronic edition of the Supplement for additional panels of this figure.]

1999 and references therein) and correlates with important cluster attributes such as velocity dispersion, mass, and X-ray temperature and luminosities for a set of X-ray luminous clusters with scatters of 15% to 40% (Yee & Ellingson 2003).

For the RCS clusters, we compute B_{gc} using a more refined method than that in Yee & López-Cruz by fully utilizing the two-band photometric data. Galaxies are counted in regions defined in the color-magnitude diagram (CMD) to minimize projection effects and counting uncertainty. This is essential for high-redshift clusters, as the effect of projected galaxies is substantially more serious than that for lower redshift clusters. A fiducial color-magnitude relation for each cluster is defined by that used to find the cluster in the first place, from which regions in the CMD for galaxy counting are established.

We compute two different B_{gc} parameters for each cluster: one using all excess galaxies (deriving what we call the total B_{gc} , or B_{gcT}), and the other using the excess red-sequence galaxies (deriving the “red-sequence” B_{gc} , or B_{gcR}). In the former we count galaxies in the CMD bounded in colors by 0.20 mag in $R_C - z'$ to the red of the red-sequence relation, and 0.25 mag in $R_C - z'$ to the blue of a blue star burst SED (colors for this limit are taken from a GISSEL Bruzual & Charlot (1993) pure starburst model of intermediate metallicity); and bounded in

magnitude by 3 mag brighter than the expected M^* , and 2 mag fainter (or the 100% completeness limit magnitude, whichever is brighter). Typically, the depth of the photometry allows the sampling (in the z' band) to 2 mag below M^* to a redshift of ~ 0.65 . At higher redshift, the B_{gc} parameter (which is normalized by the galaxy luminosity function) is derived using counts to a shallower effective depth, which increases the uncertainty, especially at $z > 1$, where on average we sample to less than 1 mag below M^* (see the detailed discussion in Yee & López-Cruz 1999). The galaxy counts are done over an aperture of radius $0.5 h_{50}^{-1}$ Mpc, centered on the nominal cluster center (see § 6.2). We retain $h = 0.5$ to keep consistency with B_{gc} measurements from Yee & López-Cruz (1999) and Yee & Ellingson (2003). Galaxy counts are modified by the sampling area as appropriate, with the sampling area estimated by examining the semirandom position-only catalogs (see § 4.3.4).

For clusters with red-sequence photometric redshifts of less than 0.45, we use the R_C catalogs for galaxy counting, while for clusters with $z > 0.45$, the z' data are used. At $z \sim 0.45$ the blue part of the R_C band begins to encroach on the 4000 Å break; hence, using the z' data diminishes uncertainties in both galaxy evolution and K -correction that are needed to apply to the photometric data for proper galaxy counts. We use the R_C -band

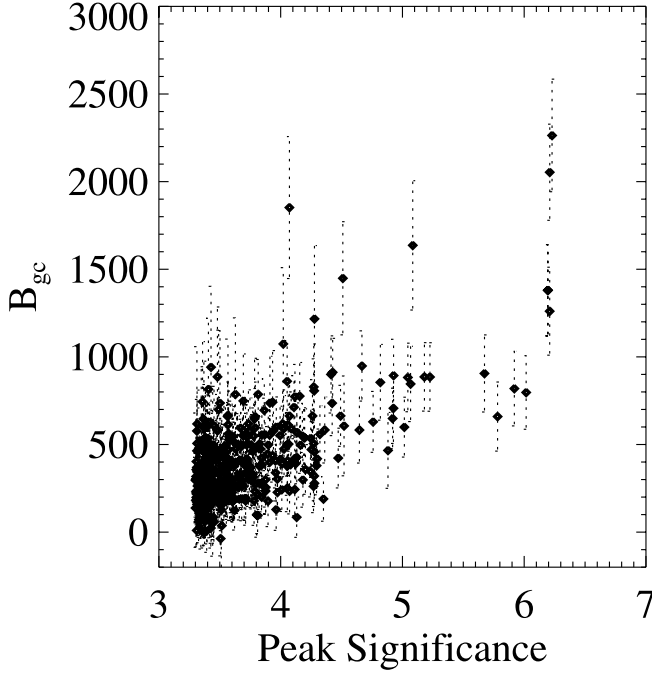


FIG. 17.—Detection significance vs. richness. The detection significance for all clusters with B_{gcR} errors less than 500 (i.e., all but the noisiest B_{gcR} measurements) is plotted against B_{gcR} . There is a broad correlation between these two parameters, though with significant scatter, as explained in the main text.

luminosity function in Yee & López-Cruz (1999) for the normalization of the galaxy counts, although we note that the simple parameterization of the evolution in M^* is almost certain not to be correct for blue galaxy dominated clusters at high redshifts. The K -corrections used are based on galaxy spectrum models from Coleman et al. (1980). We correct the LF to z' -band using $R_C - z'$ colors from the fiducial red-sequence model discussed in § 2.1. We note that we obtain very similar B_{gc} values, well within the uncertainties, for clusters at $z \sim 0.45$ when they are computed using both R_C and z' band data.

The average background galaxy counts used to perform the statistical count corrections are obtained directly from the very large amount of survey images themselves, ensuring total self-consistency. For each cluster, the average count is derived using $\sim 10 \text{ deg}^2$ of the RCS data (both patches in their entirety) with identical color and magnitude cuts as those used for the cluster. Furthermore, the large area available also allows us for the first time to derive the estimate in the stochastic variation in the background counts entirely empirically. The variance in the background count is derived for each cluster by randomly sampling the counts in several hundred areas with the same angular size and color and magnitude cuts as those used to compute the B_{gc} value. This is incorporated into the uncertainty estimate of the richness parameter.

The highly uncertain evolution of cluster galaxies at $z > 0.5$ motivates the use of a red-sequence B_{gc} . The red galaxies in clusters are much slower evolving and likely to be largely in place even at redshift one. Thus, using only the red galaxies as an estimate to the richness will provide a much more stable measurement, less affected, for example, by the varying blue fraction of clusters. (We note that in our preliminary measurements the blue fractions vary from ~ 0.2 to 0.8 for clusters at the high end of our redshift range.) This in turn should allow us to obtain more stable estimates of cluster properties such as velocity dispersion, mass, X-ray temperature, and luminosity based

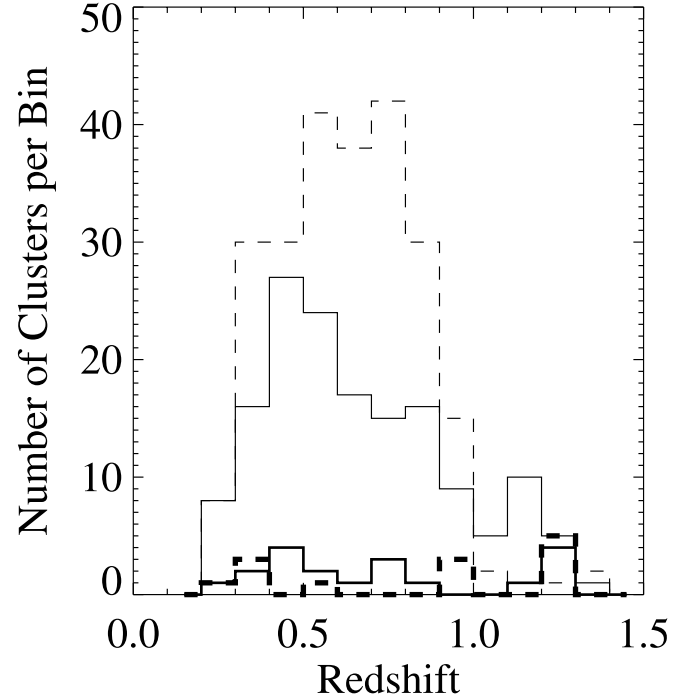


FIG. 18.—Richness-dependent redshift distributions. The four histograms show the distribution of clusters in bins 0.1 wide in redshift, for four different richness ranges. The thin dashed line is for clusters less rich than ARC 0 ($B_{gcR} < 400$), the solid thin line is for ARC 0 clusters ($400 < B_{gcR} < 800$), the solid thick line is for ARC 1 clusters ($800 < B_{gcR} < 1200$), and the dashed thick line is for ARC 2 or greater clusters ($B_{gcR} < 1200$).

on (modified) calibrations such as those from Yee & Ellingson (2003). A more detailed discussion of B_{gcR} will be given in future analysis papers on the RCS sample. We compute B_{gcR} by using a color slice with an upper (red) color bound that is 0.2 mag redder than the fiducial red sequence, and a lower (blue) color bound equivalent to the midpoint in color between an elliptical and Sbc galaxy at the relevant redshift. The background counts are obtained using the identical color cuts. The two B_{gc} parameters are listed for each cluster in our catalogs in Tables 5 and 6.

Figure 17 shows the relationship between the red-sequence richness, B_{gcR} , and the detection significance. There is a broad correlation between the two, with significant scatter. There are numerous reasons to expect significant scatter in this correlation; for example, the richness is insensitive to the cluster concentration because of the large aperture over which it is measured, whereas detection significance can be significantly boosted if a cluster is particularly compact. The depth of the data also affects the detection significance rather strongly, whereas the richness is, by design, constructed to guard against such effects.

Figure 18 summarizes the richness and redshift distribution for the two patches in aggregate. Redshift distributions are shown for four B_{gcR} richness ranges corresponding to traditional Abell Richness Classes (ARCs), as calibrated in Yee & López-Cruz (1999), without modification to account for the color cuts used here. As expected, the bulk of the clusters are of ARC 0 and poorer, and some fraction of these poorest systems are likely best termed groups. At higher redshifts the sample has proportionately more richer systems, again as expected since the poorer systems fall out of the sample owing to incompleteness.

TABLE 7
SPECTROSCOPICALLY CONFIRMED CLUSTERS IN THE PATCH RCS 1327+29

| Cluster | RCS Redshift | σ_{peak} | Other Name | Redshift |
|-------------------------|--------------|------------------------|---------------|--------------------|
| RCS J132532+2938.3..... | 0.346 | 5.91 | GHO 1323+2953 | 0.358 ^a |
| RCS J132335+3022.6..... | 0.508 | 6.19 | PDCS 062 | 0.467 ^b |
| RCS J132421+3012.6..... | 0.708 | 4.92 | GHO 1322+3028 | 0.697 ^b |
| RCS J132449+3011.6..... | 0.755 | 3.66 | GHO 1322+3027 | 0.751 ^b |

^a Gunn et al. (1986).

^b Holden (1999).

6.2.4. Known Clusters

The patch RCS 1327+29 overlaps survey fields from both the Palomar Distant Cluster Survey (Postman et al. 1996) and the older survey of Gunn et al. (1986). There are four spectroscopically confirmed clusters⁴ from these prior surveys within the boundaries of the RCS patch that we consider of sufficient reliability to warrant discussion here. All are present in Table 6, and three of these four clusters are detected at greater than 4σ . Table 7 lists each cluster, along with the RCS redshift estimate and detection significance. In all cases the estimated redshifts are consistent with the spectroscopic redshifts available from the literature.

7. SUMMARY

The RCS, now complete, is the largest moderately deep two-filter imaging survey done to date. We have developed an extensive processing pipeline to handle the data flow from this survey, which has been described extensively. Through judicious choices of observing strategies, the data are readily handled using essentially standard methods, modified slightly to accommodate the peculiarities of mosaic cameras. We have paid particular attention to the uniformity of the photometric calibration of the survey, since this affects the accuracy of cluster redshifts. The typical systematic uncertainty in the colors is expected to be less than 0.03 mag in most cases, corresponding to systematic redshift uncertainties that are no more than the expected random errors at all redshifts.

The complete data processing pipeline has been applied to data from the first two completed RCS patches. Analysis of the

basic data products such as galaxy counts illustrate that the catalogs contain no major systematic uncertainties. The targeted depths have been reached in both filters; the measured typical 5σ point source limits are 23.8 and 24.9 in z' and R_C , respectively.

Included in this paper are two catalogs of clusters at $z > 0.2$, from the patches RCS 0926+37 and RCS 1327+29. Alone these two catalogs represent a significant increase in the total population of known clusters and groups, particularly at $z > 0.5$. Processing of the RCS data is being finalized, and we expect to release further cluster catalogs soon (e.g., L. F. Barrientos et al. 2005, in preparation), with an eventual full release of all survey data (processed images, and both primary and derived catalogs).

We are grateful to the CFHT Canadian TAC for the generous allocations of CFHT time that made this project possible. We are also thankful for the efforts of the CFHT staff in providing the CFH12K camera; in particular we thank J. C. Cullandre, whose assistance has been invaluable. M. D. G. acknowledges financial support from the Canadian Natural Sciences and Engineering Research Council (NSERC) via PGSA, PGSB, and PDF Fellowships. This project is supported in part by an NSERC operating grant and a University of Toronto grant to H. K. C. Y. We also thank a number of summer students, Helen Kirk, Danica Lam, and Trevor Evans, for assistance with running the photometric pipeline and visual verification of the object-finding. Finally, we would like to thank the anonymous referee, whose detailed comments served to greatly improve the clarity of this paper.

⁴ As recorded in the NED database.

REFERENCES

- Bahcall, N. A. 1977, *ARA&A*, 15, 505
Bahcall, N. A., et al. 2003a, *ApJ*, 585, 182
———. 2003b, *ApJS*, 148, 243
Böhringer, H., et al. 2000, *ApJS*, 129, 435
Bramel, D. A., Nichol, R. C., & Pope, A. C. 2000, *ApJ*, 533, 601
Bruzual, A. G., & Charlot, S. 1993, *ApJ*, 405, 538
Burstein, D., & Heiles, C. 1978, *ApJ*, 225, 40
Butcher, H., & Oemler, A., Jr. 1984, *ApJ*, 285, 426
Coleman, G. D., Wu, C.-C., & Weedman, D. W. 1980, *ApJS*, 43, 393
Cuillandre, J., Luppino, G. A., Starr, B. M., & Isani, S. 2000, *Proc. SPIE*, 4008, 1010
Dalcanton, J. J. 1996, *ApJ*, 466, 92
Dalton, G. B., Efstathiou, G., Maddox, S. J., & Sutherland, W. J. 1992, *ApJ*, 390, L1
Ebeling, H., Edge, A. C., Bohringer, H., Allen, S. W., Crawford, C. S., Fabian, A. C., Voges, W., & Huchra, J. P. 1998, *MNRAS*, 301, 881
Ebeling, H., Edge, A. C., & Henry, J. P. 2001, *ApJ*, 553, 668
Fukugita, M., Ichikawa, T., Gunn, J. E., Doi, M., Shimasaku, K., & Schneider, D. P. 1996, *AJ*, 111, 1748
Gal, R. R., de Carvalho, R. R., Odewahn, S. C., Djorgovski, S. G., & Margoniner, V. E. 2000, *AJ*, 119, 12
Gilbank, D. G., Bower, R. G., Castander, F. J., & Ziegler, B. L. 2003, *MNRAS*, 348, 551
Gioia, I. M., Henry, J. P., Maccacaro, T., Morris, S. L., Stocke, J. T., & Wolter, A. 1990, *ApJ*, 356, L35
Gioia, I. M., & Luppino, G. A. 1994, *ApJS*, 94, 583
Gladders, M. D. 2003, in *Carnegie Observatories Astrophysics Series Vol. 3, Clusters of Galaxies: Probes of Cosmological Structure and Galaxy Evolution*, ed. J. S. Mulchaey, A. Dressler, & A. Oemler (Cambridge: Cambridge Univ. Press), 89
Gladders, M. D., & Yee, H. K. C. 2000, *AJ*, 120, 2148
———. 2005, *AJ*, in preparation
Goto, T., et al. 2002, *AJ*, 123, 1807
Gunn, J. E., Hoessel, J. G., & Oke, J. B. 1986, *ApJ*, 306, 30
Hartmann, D., & Burton, W. B. 1997, *Atlas of Galactic Neutral Hydrogen* (Cambridge: Cambridge Univ. Press)
Hoeg, E., et al. 1997, *A&A*, 323, L57
Hoekstra, H., Yee, H. K. C., Gladders, M. D., Barrientos, L. F., Hall, P. B., & Infante, L. 2002, *ApJ*, 572, 55
Holden, B. P. 1999, *AJ*, 118, 2002
Kepner, J., Fan, X., Bahcall, N., Gunn, J., Lupton, R., & Xu, G. 1999, *ApJ*, 517, 78

- Kim, R. S. J., et al. 2002, *AJ*, 123, 20
- Landolt, A. U. 1992, *AJ*, 104, 340
- Levine, E. S., Schulz, A. E., & White, M. 2002, *ApJ*, 577, 569
- Lobo, C., Iovino, A., Lazzati, D., & Chincarini, G. 2000, *A&A*, 360, 896
- Lumsden, S. L., Nichol, R. C., Collins, C. A., & Guzzo, L. 1992, *MNRAS*, 258, 1
- Margoniner, V. E., de Carvalho, R. R., Gal, R. R., & Djorgovski, S. G. 2001, *ApJ*, 548, L143
- Monet, D., Canzian, B., Harris, H., Reid, N., Rhodes, A., & Sell, S. 1998, *US Naval Obs. Flagstaff Station* 1977, 1243
- Mullis, C. R., et al. 2003, *ApJ*, 594, 154
- Olsen, L. F., et al. 1999, *A&A*, 345, 363
- Ostrander, E. J., Nichol, R. C., Ratnatunga, K. U., & Griffiths, R. E. 1998, *AJ*, 116, 2644
- Oukbir, J., & Blanchard, A. 1992, *A&A*, 262, L21
- Postman, M., Lubin, L. M., Gunn, J. E., Oke, J. B., Hoessel, J. G., Schneider, D. P., & Christensen, J. A. 1996, *AJ*, 111, 615
- Romer, A. K., et al. 2000, *ApJS*, 126, 209
- Rosati, P., della Ceca, R., Norman, C., & Giacconi, R. 1998, *ApJ*, 492, L21
- Scharf, C. A., Jones, L. R., Ebeling, H., Perlman, E., Malkan, M., & Wegner, G. 1997, *ApJ*, 477, 79
- Schlegel, D. J., Finkbeiner, D. P., & Davis, M. 1998, *ApJ*, 500, 525
- Smith, J. A., et al. 2002, *AJ*, 123, 2121
- Stoughton, C., et al. 2002, *AJ*, 123, 485
- Valtchanov, I., & Pierre, M. 2003, *Astron. Nachr.*, 324, 124
- Vikhlinin, A., McNamara, B. R., Forman, W., Jones, C., Quintana, H., & Hornstrup, A. 1998, *ApJ*, 502, 558
- Voges, W., et al. 1999, *A&A*, 349, 389
- Williams, J. P., de Geus, E. J., & Blitz, L. 1994, *ApJ*, 428, 693
- Yee, H. K. C. 1991, *PASP*, 103, 396
- Yee, H. K. C., & Ellingson, E. 2003, *ApJ*, 585, 215
- Yee, H. K. C., Ellingson, E., & Carlberg, R. G. 1996, *ApJS*, 102, 269
- Yee, H. K. C., & López-Cruz, O. 1999, *AJ*, 117, 1985
- Yee, H. K. C., et al. 2000, *ApJS*, 129, 475